A study of fluid overpressure microstructures from the creeping segment of the San Andreas Fault

Jafar Hadizadeh [a] *
[a] Department of Geographic & Environmental Sciences, University of Louisville, Louisville 40292 KY, United States.
hadizadeh@louisville.edu
Office: 502-852-2691 and mobile: 502-457-5672

Alan P. Boyle [b]
[b] Department of earth, ocean and ecological sciences, University of Liverpool, Liverpool, L69, United Kingdom.
apboyle@liverpool.ac.uk

Andrea E. Gaughan [a]
[a] Department of Geographic & Environmental Sciences, University of Louisville, Louisville 40292 KY, United States.
ae.gaughan@louisville.edu

KEYWORDS

Coseismic microstructures; Calcite veins; Calcite trace elements; Cataclasis; Aseismic creep; Calcite Cathodoluminescence.

Abstract

Evidence of episodic fluid overpressure events noted in samples from the San Andreas Fault Observatory at Depth (SAFOD) have remained largely uncorrelated in terms of their collective significance for seismic history of the fault zone. The compositional and microstructural correlations sought in this study could shed light on questions about potential for major seismic events in the creeping segment of the SAF in central California. We used quantitative energy dispersive spectroscopy (EDS), Cathodoluminescence (CL) and Scanning Electron Microscope (SEM) imaging, and electron backscatter diffraction (EBSD) analysis to acquire geochemical and microstructural data from a suite of twenty SAFOD core samples including the damage zone and the active core of the fault. The results indicate intermittent coseismic fluid overpressure events that overprint the background aseismic creep across the fault. Analysis of trace elements and deformation in the coseismic calcite vein generations and their associated hydrothermal mineral phases indicate progressive uplift and exhumation followed by an asymmetric excursion of meteoric water into the damage zone. The same analysis suggests that the actively creeping intervals act as permeability barriers. Our results are in overall agreement with recent studies of the SAF in central California that indicate large seismic events have occurred intermittent with aseismic creep in recent geological time or suggest future potential for such events.

1. Introduction

A collection of wide ranging analytical and experimental studies of core samples from the San Andreas Fault Observatory at Depth (SAFOD) shed light on microstructural, geochemical, and mechanical aspects of aseismic creep along the central section of the San Andreas Fault zone (SAF). Microstructures of fluidized gouge injection, calcite-sealed jigsaw textures, and various types of blocky calcite vein growths, mostly in samples from the SAF damage zone, have been reported in previous studies (e. g., Schleicher et al. 2009; Holdsworth et al. 2011; Gratier et al. 2011; Rybacki et al. 2011; Mittempergher et al. 2011; Hadizadeh et al. 2012; Janssen et al. 2010 and 2014; Bradbury et al. 2015, Hadizadeh et al. 2018). In most cases such observations have been attributed to local transient fluid overpressure events, possibly related to deformation by pressure solution creep or to repeating microearthquakes in the relatively inactive SAF damage zone. There are, but fewer, reports of fluid overpressure microstructures in the actively creeping core of the SAF (e.g., Moore and Rymer 2012; Luetkemeyer et al. 2016). These studies along with geophysical data and historic records of the region’s seismicity have provided grounds for raising questions about potential for major seismic events (M>6) in the creeping segment of the SAF in Central California (Noda and Lapusta 2013; French et al. 2014; Jolivet et al. 2014; Harris 2017). Maurer and Johnson (2014) noted that the 150 km long central section of the SAF has not produced a large earthquake historically. Most recently Coffey et al. (2022) used thermal maturity of a suite of biomarkers (also see Sheppard et al. 2015) and K/Ar ages in the SAFOD core samples to search for paleoseismic events in the creeping section of the SAF. The study concluded that certain intensely sheared domains in the SAFOD black gouge (foliated siltstone-shale cataclasites-Fig. 1) have experienced abundant seismicity over the past 16 million years.

While there is ample microstructural evidence of possibly-coseismic fluid overpressure in the SAFOD samples, studies to correlate these observations across the active fault core have been scarce mainly because, 1) the SAFOD samples show that there are significant compositional differences between the damage zone and the active core of the SAF (Holdsworth et al. 2011; Moore 2014; Morrow et al. 2014), and 2) the results of experimental and mechanical studies show that the serpentinite-rich gouge in the SAF core is velocity strengthening (Lockner et al 2011; Carpenter et al. 2009, 2011, 2012). Furthermore, the ongoing debate about reliability of brittle microstructures as coseismic slip indicators (e.g., Cowan 1999; Smith et al. 2008; Stunitz et al. 2010; Boutareaud et al. 2008) makes it difficult to argue that presence of blocky calcite veins, for example, indicate earthquake events in a phyllosilicate-rich aseismic creep zone. The objective of this study is to seek compositional, and microstructural correlations between fluid overpressure microstructures across the damage zone and active creep intervals of the SAF by examining a relatively large number of the SAFOD phase-3 core samples.

2. Methods

2.1 The samples and sample preparation

We present results of a geochemical and microstructural study of 20 samples from the SAFOD phase 3 drilling, spanning ~125m Measured Depth across the fault core. The sample billets were requested from the SAOD drill core collection at Gulf Coast Repository in College Station, Texas. The lithostructural units, sampling locations along the core sections 1-6, and the exact measured depth (MD) for each sample is shown in Fig. 1. The samples were selected to represent zones of moderate to intensely foliated gouge in the SAF damage zone and the actively creeping intervals: ~1.61 m-wide southwestern deforming zone (SDZ) and ~2.6m-wide central deforming zone (CDZ). The selected samples are mainly within the damage zone as defined by a zone of low P and S-waves recorded along the SAFOD main borehole (Zoback 2011-Figs. 4a-b). However, the samples were also selected to show the considerable deformation that occurs ~10m further SW the SDZ within the siltstone shale units bordering the SDZ. Here, the sample material outside the bounds of the SDZ and CDZ (Fig. 1 caption) is simply considered part of the fault damage zone, where deformation could be recognized at scales 0.1m or less on a standard petrographic thin section. In Fig. 1, the approximate position of several minor fault zones, mainly along the lithologic boundaries (e.g., reported by Holdsworth et al. 2011) are also marked, where they appear mostly concentrated within the foliated siltstone-shale lithostructural units. The drill site, scope, and geophysical well-log details of the SAFOD project (Hickman et al. 2004; Zoback et al. 2011) and protoliths of the damage zone lithostructural units are described elsewhere (Holdsworth et al. 2011; Janssen et al. 2014; Bradbury et al. 2015).

We used point-cloud imaging technique to render precise 3D images of the billets prior to physical sectioning in order to preserve a virtual copy of each billet's surface color, texture, morphology, and reference markings. The images, viewable in Microsoft 3D Viewer, were helpful in accurate sectioning of the billets as well as resectioning previously cut billets (see

Holmes et al. 2021). The sample billets were impregnated with clear epoxy resin and cut along 3 mutually perpendicular planes with the reference plane at ~90° to clearly traceable foliation at the billet scale. The billets with no visible trace of foliation were cut at 3 mutually perpendicular planes with the core orientation marker as the reference. The SEM-polish petrographic sections were surface machine-polished using 0.05 µm silicon particle colloidal suspension and each gold-sputtered for 60-75 seconds using a Cressington 108 Sputter Coater.

2.2 Imaging and analytical work

Microstructural features of interest in the samples were preliminarily studied in whole-section mosaics assembled by optical microscopy in crossed polarized light (XPL) and plane polarized light (PPL). Typical deformation microstructures of interest on the mosaics were selected for detailed electron imaging and analytical data collection. Our investigations of the SAF damage zone samples were inadvertently more focused on deformation and fluid-overpressure microstructures in gouge samples from the foliated and non-foliated siltstone-shale lithostructural units, which have been inferred to share the Great Valley Group as their protolith. However, we note that tracking evidence of deformation affecting the same/similar protoliths across the active core of the fault served to make comparisons of the features and modes of deformation more valid.

Backscatter and secondary electron images of deformed and undeformed microstructures were taken using an FEI Nova 600 FEG field emission scanning electron microscope (SEM) at 10-15 KV accelerating voltage and working distances ranging 3.5-5 mm. The electron backscatter diffraction (EBSD) analysis was conducted at the University of Liverpool using a Zeiss Gemini

450 SEM with a thermionic field emission gun, an accelerating voltage of 20kV, and a beam current of ~5 nA. We used Cathodoluminescence (CL) imaging and luminescence contrast in calcite vein networks in the samples to qualitatively differentiate the fluid source REDOX properties and relative order of the calcite vein generations. The CL results were constrained and correlated with the calcite vein EDS results as well as with the EBSD analysis of the hydrothermal phases associated with the same calcite vein networks (e.g., secondary pyrite, anhydrite, quartz). The CL images were acquired using a CITL-Mk5 cold CL stage system with exposure time between 0.5 and 10s to maximize dynamic range in the acquired images.

The atomic weight% of major and trace element composition of calcite veins in 16 samples were acquired using a Bruker Quantax Energy Dispersive Spectrometry (EDS) analyzer in an Apreo-C low vacuum field emission SEM microscope at accelerating voltage of 30kV. The measurements were made on one or more spots from each calcite vein generation, as could be determined based on CL color contrast in a vein network microstructure. Each measurement included the major and trace elements in calcium carbonate (Ca, O, C, Mg, Mn, Fe). This EDS data collection plan accounts for the sample-to-sample difference in the total number of measurement spots shown in Table 2. Additional elements S, Si, Al, K, and Na were included in each measurement to account for our preliminary observations of other phases in the sample calcite vein networks (e.g., pyrite, anhydrite, quartz, and siliciclastic inclusions). Mineral composition maps were created by interpreting elemental maps we acquired using the EDS detector analyzer. The elemental mapping targeted microstructures that showed interaction of various hydrothermal phases with blocky calcite vein networks. The EDS measurements were preferably focused on collecting data from the blocky and syntaxial calcite veins and as much as possible avoiding the antitaxial calcite vein fabric related to pressure solution cleavage in the samples. This preference was likely to provide calcite vein composition data relating to coseismic advective fluids rather than to fluids involved in aseismic diffusive mass transfer processes consistent with creep rates (Gratier et al. 2003, 2011).

3. Results

3.1 Deformation microstructures in the SAF damage zone

The typical deformation microstructures shown in Fig. 2 were selected from samples SW and NE of the SDZ (SDZ-side) and samples SW and NE of the CDZ (CDZ-side). We note that gouge zones on either side of the 95m coring gap in the SAFOD phase 3 lateral borehole G (Fig. 1) are interspersed with bands of less deformed but highly fractured protolith rocks, which are not included in Fig. 2. Deformation of the SDZ-side damage zone grades from moderately deformed, foliated block-in-matrix gouge at 3187.3m MD (Fig. 2a) to intensely foliated siltstone-shale cataclasites and ultracataclasites at 3193.7m MD ~2.8m southwest of the SDZ (Fig. 2c). The latter units are also known as 'black gouge' or 'black fault rock' in other SAFOD sample studies (e.g., Holdsworth et al. 2011; Bradbury et al. 2015; Coffey et al. 2022). The observed increases in deformation intensity may also be coincident with the presence of minor faults (thick black arrows in Fig. 1) as well as proximity to the SDZ. At core-sample scale, the foliation is mainly defined by variable intensity pressure solution cleavage and shape preferred orientation (SPO) of survivor quartzofeldspathic clasts in a matrix of siltstone-shale ultracataclasites. This general description is typical of the intervals labeled '*foliated siltstone-shale with block-in-matrix fabric* and *foliated siltstone-shale cataclasite with veins'* in Fig. 1, consistent with microstructural descriptions in previous studies (e.g., Holdsworth et al. 2011; Gratier et al. 2011; Hadizadeh et al. 2012; Bradbury et al. 2015). Microscopy reveals microstructures characteristic of deformation by cataclasis as well as pressure solution (Figs. 2a-c). The evidence of pressure solution varies from impingement dissolution of block contacts (Fig. 2a) in the block-in-matrix gouge to the development of a pervasive fabric of antitaxial calcite veins (here referred to as calcite fabric) at high angles to the solution cleavage and clast SPO in indurated quartzofeldspathic cataclasite (Fig. 2b). Microstructures of deformation by pressure solution in the same interval of the SAFOD cores are described in more detail by Gratier et al. (2011), and Richard et al. (2014). A microstructural example of alternating pressure solution and cataclastic deformation mechanisms is shown in Fig. 2c, where ultracataclasites are developed across a sheared quartzofeldspathic clast (dark streaks in small inset box). The BS-SEM image of the ultracataclasite shows that it includes reworked fragments of the calcite fabric (areas circled by dashed lines in Fig. 2c). In the same sample, a polycrystalline mass of secondary pyrite (Fig. 2d) is sheared along the foliation and appears unaffected by pressure solution. The sample directly bordering the SDZ on the NE side (G31) is mostly an undeformed fractured siltstone (not shown) while sample G32, ~1m further NE of the SDZ consists of foliated siltstone-shale cataclasites (Fig. 2e).

On the CDZ-side, typical deformation microstructures are selected from a suite of 8 samples presented in Figs. 2 f-h. A readily noted overall observation is the relative absence of intense and pervasive pressure solution cleavage and calcite fabric in this series of samples compared to those described for the SDZ-side damage zone. Evidence of deformation by pressure solution is present as local impingement dissolution in deformed vein-calcite and the quartzofeldspathic clast contacts within cataclasites and ultracataclasites (fig. 2f). The minor faults reported by Holdsworth et al. (2011) are also present in this section of the SAF damage zone close to our samples G51 and G52 (see Fig. 1). In sample G52, micro-folding of thick blocky calcite veins along foliation in ultracataclasite gouge matrix (Fig. 2g) is a remarkable example of intense deformation by cataclastic flow and development of cataclastic foliation in the CDZ-side damage zone. A close-up SEM image in Fig. 2g (large inset box) shows typical ultracataclasite matrix intrusion into tensile cracks in the folded blocky calcite veins. Microstructures in Fig. 2g demonstrate how blocks in a block-in-matrix gouge could be formed solely by deformation of calcite veins as well as by attrition of reworked quartzofeldspathic blocks. The presence of pressure solution in foliated cataclasite is shown in sample G65 at a distance of ~12m MD NE of the CDZ (Fig. 2h). In the same sample, we find a gouge injection microstructure with exceptionally large (>1) aspect ratio. The relative lack of calcite veins despite the presence of the fluidized gouge injection in this sample is notable since only a few thin strands of blocky calcite veins could be found near the tip of the injection in Fig. 2h. We also note that bending of the injection wall is accommodated through micro-scale displacements along bands of siltstone cataclasites. The growth and deformation of blocky calcite veins, unrelated to pressure solution cleavage were found to be associated with hydrothermal neo-mineralization of pyrite, anhydrite, apatite, and quartz throughout the damage zone gouge samples. In Fig. 3a-d we present interpreted elemental maps to typify these associations.

3.2 Cathodoluminescence of calcite veins in the damage zone

The CL imaging was focused on the spatial distribution of vein generations in blocky and syntaxial type calcite veins in both the damage zone and the active core of the fault. The imaged areas were selected based on a careful survey of whole-section plane-polarized (PPL) optical images. This referencing provided CL-PPL image pairs (Figs. 4,5, and 7), which allowed visual identification of microstructural boundaries of e-twinned areas and different types of e-twins on each CL image.

In general, the images from samples SW of the SDZ (Fig. 4a-c) indicate a noticeable increase in deformation intensity with proximity to minor fault zones marked in Fig. 1 and the black gouge (sample G24, 3193.7m MD-Fig. 1). The increasing deformation intensity is well represented by decreased spacing and microfaulting of calcite veins in Fig. 4b, compared to Fig. 4a. Multiple cross-cutting calcite vein generations are offset by shear displacement along microfractures in sample G24 ~2.8m MD from the SDZ (Fig. 4c). The CL images made it possible to depict, with reasonable confidence, some kinematic elements of local brittle deformation such as Riedel shear orientations (compare PPL and CL images in Figs. 4b-c). The sections from sample G31, ~0.3m MD NE of the SDZ (not shown) are almost devoid of calcite veins while sample G32 ~1.2m MD, farther NE of the SDZ (Fig. 2e) is a fine-grained foliated clast-in-matrix siltstone cataclasite. The calcite vein fabric in sample G32 is shown in the CL-PPL pair of Fig. 4d. Close inspection of the CL images in Fig. 4c (inset box) and 4d (white arrow) showed clear examples of mutually-crosscutting calcite veins with dark and light luminescence.

Across the coring gap, the SAF damage zone samples G41 and G42, SW of the CDZ, show some similarities with G31 and G32 samples NE of the SDZ in terms of general types and spatial density of calcite veins, presence of anhydrite clusters, and hydrocarbon stains in the gouge. The calcite veins in sample G41 (~1.5m SW of CDZ) are mostly blocky elongate type with anhydrite inclusions (Fig. 5a PPL image). Twin lamellae types (Fig. 5a PPL image) include densely spaced thin and lensoid types. The thick tabular type twins were mostly found in contact with anhydrite inclusion growths. We found few to no calcite veins in sample G42 (not shown). NE of the CDZ, there is a general increase in overall volume (vein thickness) and spatial density of calcite veins as multi-generation cross-cutting vein microstructures. The thick blocky calcite vein in sample G45 ~0.2m MD NE of the CDZ includes twin lamellae types indicative of twinning at elevated temperatures (Ferrill et al.2004; Lacombe et al. 2021) shown in Fig. 5b PPL image. On the CL image in Fig. 5b, a bright (margins) and dull (center) calcite luminescence zoning is noted and calcite-sealed cracks with brighter luminescence extend from the vein margins into the center of the vein. A bright/dull patchy luminescence is also noted in sample G47, at ~0.9m NE of the CDZ (Fig. 5c). However, unlike the preceding sample, the e-twin lamellae are of uniform type in areas of light and dark luminescence (Fig. 5c-PPL image). Intense ductile deformation of vein-calcite could be observed in sample G52 (Fig. 5d) ~0.2m from the minor fault zone at 3301.5m MD (see Fig. 1). The folded blocky calcites are further crosscut by relatively undeformed bright CL vein generations with open microcavities (arrows in Fig. 5d-CL image). The sample G56 shows antitaxial fibrous veins with pressure solution seams are crosscut by blocky calcite veins (Fig. 5e). Further away from the CDZ, the ductile shear of calcite in a calcite-sealed implosion jigsaw texture is shown in sample G65 at ~12.1m MD from the CDZ (Fig.5f). We note that the relative disposition of the fragments in the jigsaw texture indicate only small apparent shear strains for the area viewed in Fig. 5f.

3.3 Blocky calcite veins and injection microstructures in the SDZ and CDZ

The CL images provide clear evidence of calcite-sealed jigsaw texture (Fig. 6a-b) that may represent implosion microbreccias in the SDZ sample. The calcite e-twin types in this case tend to vary widely from sparse thin type to, thick bent, and lensoid types over mm-scale distances (inset boxes in Fig. 6a-b). While an absence of cross-cutting veins in Fig. 6a-b indicates a single event of blocky calcite growth, luminescence of the calcite is randomly non-uniform throughout the sealing mesh (white arrows in Fig. 6a-b). The CDZ sample consists of anastomosing serpentinite and quartzo-feldspathic clasts stretched along foliation. Blocky calcite growths are found within both these clasts (e.g., Fig. 6c). It is important to note that the clast blocky calcites predate the calcite veins associated with more recent alteration rind of the serpentinite block from which the sample was collected. The youngest calcite veins associated with the CDZ gouge injection microstructures, however, post-date the clast calcites since the injections crosscut the foliation in our sample. The CL image in Fig. 6c shows a thick blocky calcite vein is crosscut by a set of thin dull CL calcite veins that seal extension fractures at high-angle to foliation. The latter veins are further crosscut at a slightly different angle by a bright CL vein with medial open microcavities (white arrow in Fig. 6c). The CDZ sample also hosts a number of fluidized gouge injection microstructures (e.g., Fig. 6d), not found in our two SDZ samples. More detailed observations from clearly identifiable gouge injection microstructures, including the one shown in Fig.6d, are provided in the following.

The fluidized gouge injections in sample G44, without exception, formed at high angles to foliation. Parallel sectioning of the sample’s core billet at~5 mm intervals enabled a limited study of change in dimension of 3 different injections. The aspect ratio (width W/length L) for individual injection was determined following the procedure used by Rowe et al. (2012). Table 1 shows 7 different aspect ratios for the 3 injections since only two of the three injections were clearly traceable in the sequence of 3 parallel thin sections. The W/L ratio of the injections in sample G44 ranged from 0.24 to 0.74 with a Mean of 0.39. The data in Table 1 show only slight variations in depth and width of the injections over a ~20x40x25 mm measurement volume. The largest of the 3 injection microstructures (INJ-a in Table 1) shown in Fig. 7a, is characterized by a well-defined gouge-filled conduit with relatively straight walls. The close-up BS-SEM image across the injection (Fig. 7c) shows the blocky nature of the wall-lining calcite, globulated microstructure of the injected clay-rich gouge matrix within the injection conduit, and a symmetric compositional sequence across the injection walls. Fig. 7d exemplifies several other smaller deformed injection microstructures in the CDZ sample for which we could not obtain reliable aspect ratios. The calcite veins within quartzofeldspathic and serpentinite-rich clasts (exemplified in Fig. 6C) as well as GEN 1 veins in the injection conduit should predate the injection events as they are cross-cut by the injection microstructure. Elsewhere in our samples, only a single injection-like microstructure with an exceptionally large aspect ratio of 1.22 was found in sample G65 (Fig. 2h), ~14 m NE of the CDZ.

An interpreted EDS elemental map of the injection conduit (Fig. 8a) indicates that a calcite-sealed microbreccia wall was developed during fluidization of Mg-rich clay gouge. The map also shows that multiple gouge-filled chambers, partially separated by calcite-sealed microbreccia, are present within the injection conduit. On the CL image in Fig. 8b, we could identify 3 generations of calcite growth based on CL color contrast and cross-cutting relationship, here named GEN 1, GEN 2, and GEN3 (youngest). Mean spectral wavelength for GEN1, GEN 2, and

GEN 3 are respectively 660 ± 5 nm, 634.6 ± 1.7 nm, and 624.5 ± 4.6 nm (N=5 per generation). The CL color contrasts between these values are represented by pixel-color tiles 1, 2, and 3 on Fig. 8b. While a relative age order for GEN 1 and GEN 3 could be established by crosscutting relationship seen on the CL image, the relationship between GEN 2 calcite and the other two generations is only based on differences in spectral values given above. Close inspection of the image also shows that GEN 2 and GEN 1 mutually overprint while GEN 3 overprints, or only contacts, GEN 2 in some areas (e.g., near the injection tip). The major and trace element data from calcite generations related to the largest gouge injection microstructure were collected from 83 spots shown in the Fig. 8b CL image mosaic and summarized in Table 2b. The ternary plot of Mg, Mn, and Fe (Fig. 9a) shows considerably higher Mn/Fe ratio in GEN 3 relative to GEN1 and GEN 2 while both GEN2 and GEN3 preserve a higher Mg concentration compared to GEN 1. Mean Mn/Fe ratio for GEN 1, GEN 2, and GEN 3 calcites is respectively 0.578, 1.631, and 3.196 (see Table 2b). In terms of deformation, the EBSD grain reference orientation deviation (GROD) map (Fig. 9c) and the inverse pole figure (IPF) in Fig. 9d show GEN 1 calcite has undergone significant intracrystalline strain. In comparison, the EBSD data for a quartz vein that co-crystallized with GEN 3 calcite (Figs. 9c and 9e) shows little cumulative deformation (blue colors in Fig. 9c) and a limited range of c-axis orientation oblique to the length of the quartz vein (Fig. 9e).

3.4 The trace element and Mg/Ca ratios in calcite veins

The variation in Mn/Fe ratio in the damage zone (Fig. 10a) is clearly asymmetric. The maximum mean Mn/Fe ratio on the CDZ-side damage zone is a factor of 3 times greater than those on the SDZ-side damage zone. The trend of high Mn/Fe ratios NE of the CDZ shows a noticeable drop between ~3305.4 m and ~3301.4 m MD, which appears to coincide with the presence of two of the minor fault zones. The fluctuations in Mn/Fe ratio in samples closer to the CDZ do not seem to correlate to the other two minor fault locations marked on Fig. 10a. at ~3301 m. The variations in mean Mn/Fe ratio on the SDZ side are too small to be meaningfully attributed to the minor faults marked on Fig. 10a, SW of the SDZ interval. The Mn/Fe ratios on the SDZ-side have a low sample-to-sample variation as well as being well below the CDZ-side maximum values. This general lack of variation in Mn/Fe ratios with distance from the SDZ could indicate inactivity and/or a lack of fluid pathways on the SDZ side of the fault. The inset scattergram in Fig. 10b as well as a visual comparison of the mean Mn/Fe and Mg/Ca curves in Fig. 10 reveals that an increase in mean Mn/Fe ratio is roughly matched with a drop in mean Mg/Ca ratio. This is prominently demonstrated in the CDZ interval with the highest mean Mg/Ca ratio. Mean Mn/Fe and Mg/Ca ratios in calcite vein generations related to the fluidized gouge injections in the CDZ interval (Table 2b), are plotted as open circles on Fig. 10 for comparison with these mean values elsewhere in the CDZ sample. The mean Mn/Fe ratio in the youngest (GEN3) and the oldest (GEN1) generations respectively plot well above and below the CDZ sample average. We note that mean Mn/Fe ratio for the GEN 3 injection calcites (3.196 ± 0.41) is more comparable to the average of means for the calcite veins in the 9 samples bordering the CDZ interval (3.465 ± 0.46) than mean Mn/Fe in the CDZ sample (1.29 ± 0.21).

Fig. 10b shows that mean Mg/Ca values in the damage zone, NE of the CDZ, steadily rise, from 0.003 to 0.006, over 11.8m distance toward the CDZ interval. The individual ratio measurements in the CDZ sample fluctuate widely from 0.003 to 0.328 with mean value of 0.044, which plots as a significant peak. The Mg/Ca ratio falls sharply to 0.009 at ~1.5m SW of the CDZ border. Mean values of the Mg/Ca ratio in the injection-related youngest (GEN 3) and oldest (GEN 1) calcites fall well below the range for the calcite veins in the CDZ sample while GEN 2 injection calcites plot within the CDZ sample average. The youngest injection calcites (GEN 3) have the lowest mean Mg/Ca ratio. The damage zone average of Mg/Ca mean values for the SDZ-side and CDZ-side are respectively 0.007 and 0.005. Notably, the average Mg/Ca ratio for the two SDZ samples is 0.005, not exceeding the damage zone's average.

The ternary plots in Fig. 11 show how the normalized proportions of the trace elements Mg-Fe-Mn in the blocky calcites vary in the damage zone over distances up to 16 meters from the two active creep intervals. The plots show a general increase in the relative content of Mg within the trace element trio in the samples closer to the active creep intervals. A notable difference in the trace element composition between the CDZ and SDZ side, regardless of distance from the active creep zones, is that the overall Fe concentration of the vein calcites is 10-15% lower on the CDZ side.

4. Discussion

4.1. Deformation mechanisms

Internal structure of the foliated quartzofeldspathic gouge in the SAF damage zone varies from being dominantly defined by pressure solution cleavage (Fig. 2b) to dominantly being an SPO-defined cataclastic foliation (Fig. 2d). An explanation is that the gouge is showing progressive transition from cataclastic foliation (Chester et al. 1985) to foliation via pressure solution creep in a maturing fault zone (Bos and Spiers 2001). However, evidence of reworked pressure solution microstructures in Fig. 2c indicates possible coupled deformation mechanism.

Rutter and Mainprice (1979) and Gratier (1999) suggested that removal of soluble phases by pressure solution in highly mature fault zones may result in recurring frictional behavior. More specifically, based on a diffusion-distance limited aqueous mass transfer model, Gratier et al. (2011) argued that episodic cataclasis might be required for aseismic creep via pressure solution. Gratier et al. (2011) and Richard et al. (2014) argued that deformation by pressure solution as the dominant mechanism is a viable creep mechanism throughout the entire seismogenic zone.

The current aseismic creep in the SDZ and CDZ intervals is believed to be mainly controlled by bulk ductile flow (highly distributed grain-scale frictional sliding) of low friction ($\mu<0.3$) serpentinite alteration products found mainly as saponite smectite (e.g., Jeppson et al., 2010; Holdsworth et al., 2011; Hadizadeh et al., 2012; Bradbury et al., 2015; Moore, 2014). Several studies suggest that deformation mechanisms operating at depths below the SAFOD may involve Mg-rich phyllosilicates (e.g., chlorite) that could result from metasomatic alteration of serpentinite at greater temperatures (e.g., Carpenter et al., 2012; French et al. 2015; Carpenter et al. 2015; Moore et al. 2016). Experimental friction shows that irrespective of internal microstructures, the phyllosilicate-rich products of aseismic creep in the SAF are strongly velocity strengthening (e.g., Hadizadeh et al. 2013; Coble et al. 2014; French et al. 2014; Carpenter et al. 2015).

4.2 Microstructures of transient fluid overpressure

The microstructures of aseismic creep in the damage zone of the SAF are overprinted by calcite-sealed jigsaw textures, crosscutting generations of blocky calcite veins, and fluidized gouge injections (Figs.4 and 5). Numerous studies suggest that these microstructures indicate coseismic transient fluid overpressure events (e.g., Sibson 1986; Otsuki et al. 2005; Boulier et al. 2004, 2009; Mittempergher et al. 2011; Lin 2011; Rowe et al. 2005, 2012; Janssen et al. 2010, 2015; Smeraglia et al. 2017; Scuderi et al. 2017; Spruzeniece et al. 2021; Gu et al. 2021). The implosion microbreccias sealed by blocky calcite growths were found in the damage zone samples ~4m SW of the CDZ (e.g., Fig. 4b) and as far as ~12m NE of the CDZ (e.g., Fig. 5f). The highest densities of multi-generation blocky calcite vein networks in the damage zone (e.g., Fig. 4 b-c, Fig. 5d) were observed in samples within ~4m SW of the SDZ boundary and 2.2m NE of the CDZ boundary. The results show that the blocky calcite vein generations have been deformed by subsequent creep on the fault (Fig. 4b and Fig. 5d, 5f). The cross-cutting relationship in CL image of Fig. 5d shows new blocky calcite veins overprint earlier-generation veins deformed by folding at high-angles to foliation within the creeping gouge matrix. However, we must note that the type, spatial distribution, and deformation of calcite veins for the damage zone in the coring gap between the two SAFOD active creep intervals are unknown (Fig. 1).

The CL color spectrum in calcite is mainly the result of changes in trace concentration of Mn and Fe respectively as luminescence enhancer and luminescence quencher in $CaCO_3$ crystal structure (Grover and Read, 1983; Machel, 1985; McManus and Wallace, 1992). In geologic environments, high Mn/Fe ratios correspond to oxygen-rich meteoric pore fluids (1-3 km depths) that generates the non-biogenic bright red-orange calcite luminescence typically of spectral 588 nm; the oxygen-deprived pore fluids at the deeper levels tend to generate dull red-brown calcite luminescence typically of spectral 679 nm (Machel et al. 1999; Machel, 2000; Budd et al. 2000; Cazenave et al. 2003; Verhaert et al., 2004; Lisitsyn et al. 2012). The Mn/Fe ratio and CL colors of calcite veins, therefore, could be used as proxies for the REDOX state and relative depth of pore fluids involved in the formation of calcite veins. Based on these findings, the following luminescence observations from calcite veins in our samples pose questions regarding the provenance of fluid sources involved: 1. Mutual crosscutting of veins with different luminescence contrast (e.g., Figs. 4c-d). 2. Luminescence zoning within a single blocky vein generation (e.g., Figs. 5b-c). And 3. Non-uniform/patchy luminescence veins (e.g., Figs, 6a-b). We suggest that these luminescence interrelationships represent fluid-source mixing during fluid overpressure events. In such cases, the fluid mixing simultaneously involves hypogene as well as down-circulating supergene fluid sources in varying proportions. The involvement of hypogene fluids is also supported by the observations that the growth and deformation of the blocky calcite veins in the SAF damage zone is contemporaneous with growths of secondary pyrite, anhydrite, and quartz (Fig. 2d, Fig. 3).

The microstructural correlation of blocky calcite veins with hydrothermal mineral phases, exemplified in Fig. 3, is useful for estimating a P-T bracket for the fluid overpressure events. EBSD study of a large secondary pyrite mass in sample G24 (black gouge) showed that the pyrite has been deformed via mechanisms ranging from cataclasis to SGR (sub-grain rotation) respectively corresponding to temperatures of 120°C (SAFOD depth) to ~400°C (Hadizadeh and Boyle 2018). This P-T range together with blocky calcite trace-element ratios indicate that the fluid overpressure events had occurred episodically as the SAF gouge was uplifted and exhumed to the current SAFOD depth. The blocky, and syntaxial calcite veins also show a range of e-twin types (Fig. 5a-b and Fig. 6 a-b) that indicate deformation at a range of temperatures up to ~250°C (Ferrill et al. 2004). A study by Lacombe et al. (2021) showed that unlike calcite e-twin piezometry (Rybacki et al. 2011), which might be highly variable depending on local stress field, calcite e-twin thermometry estimates are comparatively reliable.

Fluidized gouge injection microstructures were previously reported in samples bordering the SDZ (Mittempergher et al. 2011). The gouge injections in this study (Figs. 2h, Fig. 6d, and Fig.7) provide evidence of fluid overpressure events in the CDZ sample as well as within the CDZ-side damage zone of the fault. Rowe et al. (2012) argued that the width-to-length ratio of an injection is a direct measure of the shear strain required to accommodate the injection. The CDZ injections show width to length ratio value of 0.25 for the largest injection, and mean value of 0.39 for all reliably measured injections (Table 1). Rowe et al. (2012) attributed such proportionally large aspect ratios to coseismic fluid overpressure events. The oldest (GEN 1) and the youngest (GEN 3) calcites related to the CDZ injection microstructures are in a relative-time order based on both crosscutting relationship and luminescence contrast. However, as mentioned in section 3.3, GEN 1 calcite may predate the injection event. The CL image in Fig. 8b shows that the injection of fluidized gouge and growth of GEN 3 calcites occurred after extension fracture along the GEN 1 calcite vein. Similarly, quartz-calcite veins parallel to and related to the GEN 3 injection structure crosscut GEN 1 calcite (Fig. 9b-c). Therefore, CL colors of the calcite in this case could be reliably used to relate changes in calcite Mn/Fe ratio with changes in P-T conditions.

4.3 Changes in Mn/Fe and Mg/Ca ratios in calcite veins across the fault

Assuming increased Mn/Fe ratio in calcite veins is a proxy for uplift, exhumation, and increased meteoric water activity (see 4.2), the notable southwesterly drop in Mn/Fe ratio (Fig. 10a) indicates that the creeping intervals act as cross-fault permeability barriers. This conclusion is consistent with laboratory measurements of permeability and electrical resistivity in the SAFOD samples by Morrow et al. (2014 and 2015). Morrow et al. (2014) showed that the permeability of foliated SAFOD gouge range from ~10^{-20} m^2 to 10^{-19} m^2 in the damage zone and is ~10^{-21} m^2 in the fault core intervals. Our results also suggest that the incursion of shallow meteoric water into the SAF, at least close to the SAFOD site, is asymmetric and is mostly confined to the NE side of the fault zone. A similar conclusion regarding the permeability of the active creeping intervals of the SAF was reached by clumped-isotope thermometry of the calcite veins in the SDZ and CDZ samples, carried out by Luetkemeyer et al. (2016). The latter study showed that the $\delta^{18}O$ values of paleofluids, detected in the calcite veins, approach equilibrium with modern pore waters only farther away from the CDZ and SDZ. This finding is particularly consistent with our results for the CDZ side of the fault as well as with results of a study by Schleicher et al. (2010).

A comparison of the mean Mn/Fe and Mg/Ca ratios in individual gouge-injection calcite vein generations in the CDZ (open circle symbols, Fig. 10) with those of the blocky calcites elsewhere in the samples provide some insight into the relative age and source of the fluids involved. While the GEN 2 mean values in the CDZ interval tend to agree with the overall trend represented by the dotted line curve in Fig. 10a-b, the ratios for GEN 1 and GEN 3 calcites plot below and above the trend within the CDZ sample. In particular, we interpret the progressive increase in Mn/Fe ratio of the injection calcites, from 0.578 to 3.196 (Table 2b), as intermittent seismic events over a period of uplift and exhumation with GEN 3 calcites representing the latest coseismic event. The EBSD analysis (Fig. 9b-e) shows that the oldest (GEN 1) calcite grains adjacent to the gouge injection microstructure (Fig. 8) preserve high intracrystalline distributed lattice distortions up to 25° (see GROD values in Fig. 9c) and well-developed e-twins (Figs. 9b-c) consistent with significant intracrystalline strain. Conversely, the GEN3 calcite grains in the injection microstructure have low GROD values and typically contain no e-twins, consistent with having experienced little or no strain after formation of the injection structure. The GEN3 injection structures are associated with quartz veining. One such vein cuts and displaces the GEN3 calcite vein (see dotted area in Fig. 9b-c). The larger quartz grains (pale blue in Fig. 9b) show dark blue colours in the GROD map (Fig. 9c) consistent with having experienced limited or no post vein formation strain, as with the associated GEN3 calcite in the main injection structure. The inset scatterplot in Fig. 10b shows a negative correlation between Mg/Ca and Mn/Fe ratios in the studied vein calcites. This relationship is clearly not applicable to GEN 3 injection calcites. The discrepancy could be resolved to a significant degree if the injection pore fluid had originated outside the CDZ interval. Given the compositional similarity of GEN 3 calcites with the calcites in the bordering damage zone (Fig. 10a), we suggest that the latest gouge fluidization event in the CDZ was triggered by a coseismic incursion of meteoric water from the damage zone on the NE side of the CDZ. On the other hand, the fluid source for GEN 1 and GEN2 calcites appear to be internal to the low-permeability CDZ interval. It must be noted again that for lack of available core material we cannot assess the extent of meteoric water activity in the ~95m measured depth distance that separates CDZ and SDZ.

The SDZ and most of the damage zone calcite veins in the studied samples have a Mean Mg/Ca ratio of 0.0055 (SD 0.0022), which is close to those reported by Bradbury et al. (2015). The CDZ-side damage zone Mg/Ca mean values fall further to 0.003 (SD .0008) for the samples >2m away NE of the CDZ. In notable contrast, the Mean Mg/Ca ratio in the CDZ interval, while varying widely, is about an order of magnitude greater than Mean Mg/Ca ratio of the fault zone (Fig. 10b). The magnesian composition of calcite veins in the CDZ could be attributed to this interval's higher rate of serpentinite alteration due higher creep rate, which was initially discovered as borehole casing deformation (Zoback 2011) and later studied by Moore (2014). The low Mg/Ca values elsewhere across the fault indicate lack of dissolved-Mg transfer due to permeability barrier nature of the creeping intervals. We take this to imply change in pore fluid chemistry during exhumation to SAFOD depths in a manner consistent with the model proposed by Luetkemeyer et al. (2016-Fig. 6). The latter model does not preclude preservation and activity of trapped Fe-rich pore fluid enclaves in the low-permeability barrier zones and is consistent with the notable differences in calcite-vein trace element proportions across the SAF damage zone (Fig. 11). Another possible explanation for low Mg/Ca values in the SDZ is that the studied calcite veins shown in Fig. 6a-b formed within the less altered serpentinite blocks, where the vein fluids crystallized under a restricted dissolved-Mg transfer environment. Thus, it is probable that the SDZ mean Mg/Ca could be higher than the surrounding damage zone if data from calcite veins in the altered rind of the serpentinite block (if found) were included.

4.4 Implications for the seismicity of the creeping section

The potential for seismicity as well as occasional hazardous earthquake events (M>6) along known creeping fault zones, some slipping on low friction gouge, is not rare (Harris 2017). Several models have been proposed for processes that could lead to seismic instability in an otherwise aseismic regime. Veveakis et al. (2010) and Alevizos et al. (2014) hypothesized that serpentinite dehydration reactions in mature creeping fault zones might trigger a critical bifurcating process whereby thermal fluid pressurization could result in preservation of a steady state and/or an earthquake event. Other models based on geophysical data analysis, experimental work, and historic earthquake records suggest that intermittent slip-rate acceleration could occur within sections or the entire length of a creeping fault segment due to seismic ruptures in adjacent locked sections (Noda and Lapusta 2013; Jolivet et al. 2014; French et al. 2014, 2015). The aseismic creep rates in central California, measured along strike at the surface and geophysically ascertained to depths of ~30km, range from 22-35mm/year (Titus et al. 2006; Toke et al. 2011; Maurer and Johnson 2014; Jolivet et al 2014). Considering this range of slip-rates, Maurer and Johnson (2014) estimated the degree of frictional locking and its corresponding moment accumulation rate for long-term slip rates of 27-34mm/year. Their results suggest that locked patches may develop at between 10-20km depths and potentially rupture with M_w 6.5 with return time of 150 years. However, a significant factor regarding accelerating slip rates in aseismically deforming mature fault zones is the velocity strengthening nature of phyllosilicate-rich gouges. Noda and Lapusta (2013) suggested that the rate-strengthening frictional property of the clay gouge in the SAF core could be overcome by shear heating and thermal fluid pressurization if the creeping fault is loaded by a large distant seismic event. They maintained that aseismically creeping patches surrounded by low permeability rocks are more susceptible to reduced frictional resistance, as demonstrated in Taiwan 1999 Chi-Chi earthquake (Tanikawa and Shimamoto 2009).

The described models are partially consistent with our findings as they account for the possible coseismic fluid overpressure microstructures in the SDZ and CDZ while considering these intervals as permeability barriers. Furthermore, the presence of blocky calcite growths, and fluidized gouge injections in the CDZ and SDZ indicate that the coseismic events were not limited to the SAF damage zone. If the Creeping intervals are permeability barriers as our results indicate, changes in slip rate could involve hypogene fluid influx from below as well as occasional SAFOD depth-level fluid influx due to far away rupture propagations. Experimental work of French et al. (2014) on CDZ gouge samples at sub-seismic slip-rates showed evidence of dynamic weakening by shear-heating pressurization of pore fluid in the wet gouge and possible dehydration in the dry gouge. The study concluded that rupture propagation from a microseismic patch within the CDZ is unlikely, but sustained propagation from a large earthquake may be possible. In a biomarker thermal maturity analysis, Coffey et al. (2022) found that the intensely sheared intervals of the SAFOD black gouge (3192-3196 m MD) bordering the SW side of the SDZ, yield Mean maximum coseismic temperature of 840°C and minimum K/Ar age of ~3.2 Ma. The K/Ar ages also showed that black gouge is the youngest (9.5-3.3 Ma) while the CDZ-side gouges are considerably older (43-33.8 Ma). The latter age determination is consistent with the presence of blocky calcite veins (Fig. 6c) in our CDZ sample that predate the more recent alteration of the serpentinite block from which the sample is collected. This finding widens the age span for the development of blocky calcite vein textures (mesh and jigsaw patterns) in the CDZ interval. Regardless of the absolute and/or relative age of the coseismic fluid overpressure vein-forming events in our study, their widespread presence shows that the creeping SAF has intermittently hosted seismic events. Although Coffey et al. (2022) did not identify seismic events within the SDZ, the multiple coseismic slips in black gouge associated with very localized frictional heat could indicate thermal fluid pressurization proximal to the SDZ where we find a meshwork of blocky calcite veins seal the sheared serpentinite clasts (Fig. 6a-b). Furthermore, the presence of significant secondary pyrite in our black gouge sample points to the involvement of hypogene fluids. It is important to note that, as shown here, the events involving hypogene fluid pressurization in permeability barriers are going to be episodic with irregular return times. This could in turn expose aseismically creeping fault segments to significant earthquakes with indeterminate return times. Further studies may be necessary to investigate whether the entrained serpentinite-rich bodies in the SAF creeping segment have been locked intermittently over longer geological time.

5. Conclusions

Our results indicate that the damage zone and the actively creeping intervals of the SAF at SAFOD have been subject to intermittent coseismic fluid overpressure events. The recurring events are clearly indicated by multiple generations of blocky calcite growth, implosion microbreccias, and fluidized gouge injections. The CL of the calcite veins indicate the activity of both hypogene and supergene fluid sources with older veins tending to be hypogene-sourced and the youngest supergene-related. Analysis of trace-element composition of the vein calcites and their deformation alongside associated hydrothermal mineral phases show progressive uplift and exhumation followed by an asymmetric incursion of meteoric (supergene) water into the SAF damage zone. The same analysis also suggests that the actively creeping intervals have acted, at least lately, as permeability barriers. The differing creep rates in the two actively creeping intervals, SDZ and CDZ, is reflected in different intake of Mg in the calcite veins in the intervals. Our results are in overall agreement with recent studies of the SAF in central California that indicate large seismic events have occurred intermittently with aseismic creep in recent geological time or suggest future potential for such events.

Acknowledgments

We thank Diane Moore of the US Geological Survey and an anonymous reviewer for valuable constructive reviews of the manuscript. We would like to acknowledge assistance by Elliot Holmes in generating the whole sections optical images, Forrest Stevens, and Donald J. Biddle with generating 3D point cloud sample billet images. This research was partially supported by the U.S. National Science Foundation grant NSF-EAR-1800933 to J. Hadizadeh and A. E. Gaughan.

REFERENCE

Alevizos, S., Poulet, T., Veveakis, E., 2014. Thermo-poro-mechanics of chemically active creeping faults. 1: Theory and steady state considerations. J. Geophys. Res. 119(6), 4558-4582.

Bos, B. and Spiers, C. J., 2002. Frictional-viscous flow of phyllosilicate-bearing fault rock: Microphysical model and implications for crustal strength profiles. J. Geophys. Res. 107 (B2), ECV-1.

Bos, B., and Spiers, C. J., 2001. Experimental investigation into the microstructural and mechanical evolution of phyllosilicate-bearing fault rock under conditions favoring pressure solution. J. Struct. Geol. 23, 1187-1202.

Boullier, A-M., Yeh, E-C., Boutareaud, S., Song, S-R., Tsai, C-H., 2009. Microscale anatomy of the 1999 Chi-Chi earthquake fault Zone. Geochem. Geophys. Geosystem10 (3), 1525-2027.

Boullier, A-M., Fujimotob, K., Ohtanib, T., Roman-Rossa, G., Lewinc, E., Itob, H., Pezardd, P., Ildefonse, B., 2004. Textural evidence for recent co-seismic circulation of fluids in the Nojima fault zone, Awaji island, Japan. Tectonophys. 378, 161-181.

Boutareaud, S., Calugaru, D-G., Han, R., Fabbri, O., Mizoguchi, K., Tsutsumi, A., Shimamoto, T., 2008. Clay-clast aggregates: A new textural evidence for seismic fault sliding? Geophys. Res. Lett. 35, L05302.

Bradbury, K.K., Davis, C.R., Shervais, J.W., Janecke, S.U., Evans, J.P., 2015. Composition, alteration, and texture of fault-related rocks from SAFOD core and surface outcrop analogs: evidence for deformation processes and fluid-rock interactions. PAGEOPH 172, 1053–1078.

Braithwaite, C. J, 2016. Cathodoluminescence in Quaternary carbonate deposits. Sedimentary Geology 337, 29-35.

Budd, D. A., Hames, U., Ward, B., 2000. Cathodoluminescence in calcite cements: New insights on Nb and Zn Sensitizing, Mn activation, and Fe quenching at low trace-element concentrations. J. Sedimentary Res. 70 (1), 217-226.

Carpenter, B. M., Saffer, D. M., Marone, C., 2015. Frictional properties of the active San Andreas Fault at SAFOD: Implications for fault strength and slip behavior. J. Geophys. Res. 120, 5273–5289.

Carpenter, B.M., Saffer, D. M., Marone, C., 2012. Frictional properties and sliding stability of the San Andreas fault from deep drill core. Geology 40, 759-762.

Carpenter, B.M., Marone, C., Saffer, D.M., 2011. Weakness of the San Andreas Fault revealed by samples from the active fault zone. Nature Geoscience 4(4), 251–254.

Carpenter, B.M., Marone, C., Saffer, D.M., 2009. Frictional behavior of materials in the 3D SAFOD volume. Geophys. Res. Lett. 36, L05302.

Cazenave, S., Chapoulie, R., and Villeneuve, G., 2003. Cathodoluminescence of synthetic and natural calcite: the effects of manganese and iron on orange emission. Min. Petrol. 78, 243-253.

Chester, F. M., Friedman, M., Logan, J. M., 1985. Foliated cataclasites. Tectonophys. 111, 139-146.

Coble, C. G., French, M. E., Chester, F. M., Chester, J. S., Kitajima H., 2014. In situ frictional properties of San Andreas Fault gouge at SAFOD. Geophys. International J. 199 (2), 956-967.

Coffey, G.L., Savage, H. M., Polissar, P. J., Cox, S. E., Hemming, S. R., Winckler, G., Bradbury, K. K., 2022. History of earthquakes along the creeping section of the San Andreas fault, California, USA. Geology 50, 516–521.

Cowan, D. S., 1999. Do faults preserve a record of seismic slip? A field geologist’s opinion. J. Struct. Geol. 21, 995-1001.

Ferrill, D. A., Morris, A. P., Evans, M. A., Burkhardd, M., Groshong Jr., R. H., Onasch, C. M., 2004. Calcite twin morphology: a low-temperature deformation geothermometer. J. Struct. Geol. 26, 1521-1529.

French, M. E., Chester, F. M., Chester, J. S., 2015. Micromechanisms of creep in clay-rich gouge from the central deforming zone of the San Andreas Fault. J. Geophys. Res. 120, 827–849.

French, M. E., Kitajima, H., Chester, J. S., Chester, F. M., Hirose, T., 2014. Displacement and dynamic weakening processes in smectite-rich gouge from the Central Deforming Zone of the San Andreas Fault. J. Geophys. Res. 119, 1777–1802.

Gratier, J.P., Richard, J., Renard, F., Mittempergher, S., Doan, L. M., Di Toro, G., Hadizadeh, J., Boullier, A. M., 2011. Aseismic sliding of active faults by pressure solution creep: evidence from the San Andreas Fault Observatory at Depth. Geology 39, 1131–1134.

Gratier, J.-P., Favreau, P., Renard, F., 2003. Modeling fluid transfer along Californian faults when integrating pressure solution crack sealing and compaction process: J. Geophys. Res.108 (B2).

Gratier, J-P., Renard, F., Labaume, P., 1999. How pressure solution creep and fracturing processes interact in the upper crust to make it behave in both a brittle and viscous manner. J. Struct. Geol. 21 (8-9), 1189-1197.

Grover, Jr., G. and Read, J. E., 1983. Paleoaquifer and deep burial related cements defined by regional cathodoluminescent patterns, Middle Ordovician carbonates, Virginia. AAPG Bull. 67 (8), 1275-1303.

Gu, D., Han, R., Woo, S., 2021. Geological records of coseismic shear localization along the Yangsan fault, Korea. J. Geophys. Res. 126, e2020JB021393.

Hadizadeh, J. and Boyle, A. P., 2018. A study of secondary pyrite deformation and calcite veins in SAFOD damage zone with implications for aseismic creep deformation mechanism at depths>3 km. J. Struct. Geol. 117, 14-26.

Hadizadeh, J., Tullis, T. E., White, J. C., Konkachbaev, A., 2015. Shear localization, velocity weakening behavior, and development of cataclastic foliation in experimental granite gouge. J. Struct. Geol. 71, 86-99.

Hadizadeh, J., Carpenter, B. M., Mitchell, T. M., Di Toro, G., 2013. Microstructures of reconstituted SAFOD gouge deformed in room temperature friction experiments at 14 μm/s to 6 m/s sliding velocities. AGU. Fall meeting Abstracts (vol.2013, pp T33C-2652).

Hadizadeh, J., Mittempergher, S., Gratier, J. P., Renard, F., Di Toro, G., Richard, J., Babaie, H.A., 2012. A microstructural study of fault rocks from the SAFOD: Implications for the deformation mechanisms and strength of the creeping segment of the San Andreas Fault. J. Struct. Geol. 42, 246–260.

Harris, R. A., 2017. Large earthquakes and creeping faults. Rev. Geophys. 55,169-198.

Hickman, S., Zoback, M., Ellsworth, W., 2004. Introduction to special section: Preparing for the San Andreas Fault Observatory at Depth. Geophys. Res. Lett. 31, L12S01.

Holdsworth, R.E., van Diggelen, E. W. E., de Bresser, J.H.P., Walker, R. J., Bowen, L., 2011. Fault rocks from the SAFOD core samples: implications for weakening at shallow depths along the San Andreas Fault, California. J. Struct. Geol. 33, 132–144.

Holmes, E.M., Gaughan, A.E., Biddle, D.J., Stevens, F.R., Hadizadeh, J., 2021. Geospatial Management and Analysis of Microstructural Data from San Andreas Fault Observatory at Depth (SAFOD) Core Samples. ISPRS Int. J. Geo-Inf. 10, 332.

Janssen, C., Naumann, R., Morales, L., Wirth, R., Rhede, D., Dresen, G., 2015. Co-seismic and/or a-seismic microstructures of JFAST 343 core samples from the Japan Trench. Marine Geology 362, 33-42.

Janssen, C., Wirth, R., Wenk, H.-R., Morales, L., Naumann, R., Kienast, M., Song, S.-R., Dresen, G., 2014. Faulting processes in active faults e Evidences from TCDP and SAFOD drill core samples. J. Struct. Geol. 65, 100-116.

Janssen, C., Kanitpanyacharoen, W., Wenk, H.-R., Wirth, R., Morales, L., Rybacki, E., Kienast, M., Dresen, G., 2012. Clay fabrics in SAFOD core samples. J. Struct. Geol. 43, 118-127.

Janssen, C., Wirth, R., Reinicke, A., Rybacki, E., Naumann, R., Wenk, H.-R., Dresen, G., 2011. Nanoscale porosity in SAFOD core samples (San Andreas Fault). Earth Plan. Sci. Lett. 301, 179-189.

Janssen, C., Wirth, R., Rybacki, E., Naumann, R., Kemnitz, H., Wenk, H.-R., Dresen, G., 2010.

Amorphous material in SAFOD core samples (San Andreas Fault): Evidence for crush origin psuedotachylytes? Geophys. Res. Lett. 37, L01303.

Jeppson, T. N., Bradbury, K. K., Evan, J. P., 2010. Geophysical properties within the San Andreas Fault Zone at the San Andreas Fault Observatory at Depth and their relationships to rock properties and fault zone structure. J. Geophys. Res. 115, B12423.

Jolivet, R., Simons, M., Agram, P. S., Duputel, Z., Shen, Z. K., 2015. Aseismic slip and seismogenic coupling along the central San Andreas Fault. Geophys. Res. Lett. 42, 297–306.

Lacombe, O., Parlangeau, C., Beaudoin, N. E., Amrouch, K., 2021.Calcite Twin Formation, Measurement and Use as Stress–Strain Indicators: A Review of Progress over the Last Decade. Geosciences 11, 445.

Lin, A., 2011. Seismic slip recorded by fluidized ultracataclastic veins formed in a coseismic shear zone during the 2008 Mw 7.9 Wenchuan earthquake. Geology 39 (6), 547–550.

Lisitsyn, V. M., Polisadova, E. F., Valiev, D. T., 2012. Pulsed Cathodoluminescence of Calcite Crystals of Various Origins. Inorganic Materials 48 (7), 738–744.

Lockner, D.A., Morrow, C., Moore, D., Hickman, S., 2011. Low strength of deep San Andreas Fault gouge from SAFOD core. Nature 472, 82–85.

Luetkemeyer, B., Kirschner, D. L., Huntington, K. W., Chester, J. S., Chester, F. M., Evans, J. P., 2016. Constraints on paleofluid sources using the clumped-isotope thermometry of carbonate veins from the SAFOD (San Andreas Fault Observatory at Depth) borehole. Tectonophysics 690, 174-189.

Machel, H.G., Application of Cathodoluminescence to carbonate diagenesis. In: Pagel M., Barbin V., Blanc P., Ohnenstetter D. (Eds.), Cathodoluminescence in Geosciences. Springer-Verlag, Berlin, pp. 271–301. 2000.

Machel, H.G., Mason, R. A., Mariano, A. N., Mucci, A., Causes and emission of luminescence in calcite and dolomite. In: Luminescence Microscopy: Qualitative and Quantitative Aspects. Charles E. Barker and Otto C. Kopp eds. 1999.

Machel, H.G., 1985. Cathodoluminescence in calcite and dolomite and its chemical interpretation. Geoscience Canada 12, 139–147.

McManus, A., Wallace, M.W., 1992. Age of Mississippi valley-type sulfides determined using Cathodoluminescence cement stratigraphy, Lennard shelf, canning basin, Western Australia. Econ. Geol. 87, 189–193.

Maurer, J., and Johnson, K., 2014. Fault coupling and potential for earthquakes on the creeping section of the central San Andreas Fault. J. Geophys. Res. 119, 4414–4428.

Mittempergher, S., Di Toro, G. D., Gratier, J-P., Hadizadeh, J., Smith, S., 2011. Evidence of transient increases of fluid pressure in SAFOD Phase III Cores. Geophys. Res. Lett. 38, L03301.

Moore, D. E., Lockner, D. A., Hickman, S., 2016. Hydrothermal frictional strengths of rock and mineral samples relevant to the creeping section of the San Andreas Fault. J. Struct. Geol. 89, 153-167.

Moore, D. E., 2014. Comparative mineral chemistry and textures of SAFOD fault gouge and damage-zone rocks. J. Struct. Geol. 68, 82-96.

Moore, D.E., Rymer, M.J., 2012. Correlation of clayey gouge in a surface exposure of serpentinite in the San Andreas Fault with gouge from the San Andreas Fault Observatory at Depth (SAFOD). J. Struct. Geol. 38, 51–60.

Morrow, C., Lockner, D. A., Hickman, S., 2015. Low resistivity and permeability in actively deforming shear zones on the San Andreas Fault at SAFOD. J. Geophys. Res. 120, 8240–8258.

Morrow, C. A., Lockner, D. A., Moore, D.E., Hickman, S., 2014. Deep permeability of the San Andreas Fault from San Andreas Fault Observatory at Depth (SAFOD) core samples. J. Struct. Geol. 64, 99-114.

Noda, H. and Lapusta, N., 2013. Stable creeping fault segments can become destructive as a result of dynamic weakening. Nature 493, 519-521.

Otsuki, K., Uduki, T., Monzawa, N., and Tanaka, H., 2005. Clayey injection veins and pseudotachylyte from two boreholes penetrating the Chelungpu fault, Taiwan: Their implications for the contrastive seismic slip behaviors during the 1999 Chi-Chi earthquake. Island Arc 14(1), 22–36.

Richard, J., Gratier, J-P., Doan, M-L., Boullier, A-M., Renard, F., 2014. Rock and mineral transformations in a fault zone leading to permanent creep: Interactions between brittle and viscous mechanisms in the San Andreas Fault. J. Geophys. Res. 119, 8132–8153.

Rowe, C. D., Kirkpatrick, J. D., Brodsky, E. E., 2012. Fault rock injections record paleo-earthquakes. Earth Plan. Sci. Lett. 335, 154-166.

Rowe, C.D., Moore, J.C., Meneghini, F., McKiernan, A.W., 2005. Large-scalepseudotachylytes and fluidized cataclasites from an ancient subduction thrust fault. Geology 33 (12), 937-940.

Rutter, E. H. and Mainprice, D. H., 1979. On the possibility of slow fault slip controlled by a diffusive mass transfer. Gerlands Beitr. Geophys. 88(2), 154–162.

Rybacki, E., Janssen, C., Wirth, R., Chen K., Wenk, H.-R., Stromeyer, D., Dresen, G., 2011. Low-temperature deformation in calcite veins of SAFOD core samples (San Andreas Fault)- Microstructural analysis and implications for fault rheology. Tectonophysics 509, 107-119.

Schleicher, A.M., van der Pluijm, B.A., Warr, L.N., 2010. Nanocoatings of clay and creep of the San Andreas fault at Parkfield, California. Geology 38, 667–670.

Schleicher, A. M., Tourscher, S. N., van der Pluijm, B. A., and Warr, L. N., 2009. Constraints on mineralization, fluid-rock interaction, and mass transfer during faulting at 2-3 km depth from the SAFOD drill hole. J. Geophys. Res. 114 (B4).

Scuderi, M. M., Collettini, C., Marone, C., 2017. Frictional stability and earthquake triggering during fluid pressure stimulation of an experimental fault. Earth Plan. Sci. Lett. 477, 84-96.

Sheppard, R.E., Polissar, P.J., and Savage, H.M., 2015. Organic thermal maturity as a proxy for frictional fault heating: Experimental constraints on methylphenanthrene kinetics at earthquake timescales: Geochim. et Cosmochim. Acta 151, 103–116.

Sibson, R.H., 1986. Earthquakes and rock deformation in crustal fault zones. Annual Rev. Earth Plan. Sci. 14, 149–175.

Smeraglia, L., Billi, A., Carminati, E., Cavallo, C., Doglioni, C., 2017. Field- to nano-scale evidence for weakening mechanisms along the fault of the 2016 Amatrice and Norcia earthquakes, Italy. Tectonophysics 712, 156-169.

Smith, S.A. F., Collettini, C., Holdsworth, R. E., 2008. Recognizing the seismic cycle along ancient faults: CO2-induced fluidization of breccias in the footwall of a sealing low-angle normal fault. J. Struct. Geol. 30, 1034-1046.

Spruženiece, L., Späth, M., Urai, J. L., Ukar, E., Selzer, L., Nestler, B., 2021. Wide-blocky veins explained by dependency of crystal growth rate on fracture surface type: Insights from phase-field modeling. Geology 49 (6), 641-646.

Stunitz, H., Keulen, N., Hirose, T., Heilbronner, R. E., 2010. Grain size distribution and microstructures of experimentally sheared granitoid gouge at coseismic slip rates- Criteria to distinguish seismic and aseismic faults? J. Struct. Geol. 32, 59-69.

Suchy, V., Heijlenb, W., Sykorovac, I., Muchezb, Ph., Dobesd, P., Hladikovad, J., Jackovad, I., Safandae, J., Zemana, A., 2000. Geochemical study of calcite veins in the Silurian and Devonian of the Barrandian Basin (Czech Republic): evidence for widespread post-Variscan fluid flow in the central part of the Bohemian Massif. Sed. Geol. 131, 201-219.

Tanikawa, W., and Shimamoto, T., 2009. Frictional and transport properties of the Chelungpu fault from shallow borehole data and their correlation with seismic behavior during the 1999 Chi-Chi earthquake. J. Geophys. Res. 114, B01402.

Titus, S. J., DeMets, C., and Tikoff, B., 2006. Thirty-Five-Year Creep Rates for the Creeping Segment of the San Andreas Fault and the Effects of the 2004 Parkfield Earthquake: Constraints from Alignment Arrays, Continuous Global Positioning System, and Creep meters. Bull. Seism. Soc. Amer. 96 (4B), 250-268.

Toké, N.A., Arrowsmith, J R., Rymer, M.J., Landgraf, A., Haddad, D.E., Busch, M., Coyan, J., Hannah, A., 2011. Late Holocene slip rate of the San Andreas fault and its accommodation by creep and moderate magnitude earthquakes at Parkfield, California. Geology 39 (3), 243-246.

Verhaert, G., Muchez, P., Sintubin, M., Similox-Tohon, D., Vandycke, S., Keppens, E., Hodge, E.J., Richards, D.A., 2004. Origin of palaeofluids in a normal fault setting in the Aegean region. Geofluids 4, 300–314.

Veveakis, E., Alevizos, S., Vardoulakis, I., 2010. Chemical reaction capping of thermal instabilities during shear of frictional faults. J. Mech. Phys. Solids 58, 1175-1194.

Zoback, M.D., Hickman, S.H., Ellsworth, W.E., 2011. Scientific drilling into the San Andreas Fault Zone — An Overview of SAFOD's First Five Years. Scientific Drilling 11, 14-28.

Figure Captions

Fig. 1. Location of studied samples, shown by crossed circles, as distributed along the SAFOD phase 3 lateral borehole G. Measured Depth, core Run, and core Section for each sample billet is indicated atop two lithostructural bars representing two core segments of the SAFOD phase III drilling. Southwestern Deforming Zone and Central Deforming Zone, respectively labeled SDZ (~3196.5-3198.3 m MD) and CDZ (~3296.5-3299.1 m MD), are active creep intervals detected as deformation of borehole metal casing during drilling (Zoback et al. 2010). Black arrows indicate approximate position of minor faults reported by Holdsworth et al. (2011). An approximately 95m core hiatus separates the two segments of drillhole G. Core metering and lithostructural unit boundaries modified after Holdsworth et al. (2011), Janssen et al. (2014), and Bradbury et al. (2015).

Fig. 2. Typical deformation microstructures in siltstone-shale units of the SAF damage zone. Images are optical PPL unless otherwise stated. Trace of foliation identifiable at section-scale is indicated by dashed line labeled F.

a. Close-up view showing impingement dissolution of a reworked quartzo-feldspathic block in block-in-matrix gouge. Inset box relates the magnified area to a general view of the gouge microstructure. Sample G11, 3187.3m MD.

b. Typical foliation mainly defined by a pressure solution cleavage. An antitaxial calcite vein fabric at high angles to foliation is present in quartzofeldspathic clasts. Note that calcite veins are confined to within clast boundaries. Sample G23, 3193.3m MD.

c. BS-SEM image showing close-up view of ultracataclasite located within dark-colored streaks in the smaller inset box. Dashed line areas encircle fragments of calcite vein fabric relicts from earlier deformation by pressure solution. Cal is calcite, QFc is reworked quartzofeldspathic clast. Sample G24, 3193.7m MD (black gouge ~2.8m SW of SDZ).

d. Sheared mass of secondary pyrite stretched sub-parallel to trace of foliation. Note absence of deformation by pressure solution at contacts between pyrite mass and quartzofeldspathic gouge. Inset box is location of chemical map in Fig. 3b. Sample same as in c.

e. Pressure solution cleavage foliation NE of SDZ. Anastomosing relaxation cracks have opened along foliation. Note calcite fabric in siltstone clast on far-left side. Inset box is location of Fig. 4d. Sample G32, 3198.6m MD.

f. Calcite-sealed blocks of fractured banded siltstone ~1.6m SW of CDZ. White arrow points to impingement dissolution. Sample G41, 3295m MD.

g. Intensely deformed foliated block-in-matrix gouge including multiple generations of blocky calcite veins. Convoluted calcite veins reflect flowage of shale-rich ultracataclasite matrix between quartzofeldspathic cataclasite blocks. Inset SEM-SE image shows typical injection of matrix ultracataclasites into tensile microfractures in calcite veins in this sample. Sample G52, 3301.34m MD.

h. Shallow injection of coarse-grained cataclasites into a reworked block in block-in-matrix gouge (dotted trace). Arrows show pressure solution seams along bands of siltstone cataclasite. White streaks are thin blocky calcite veins. Sample G65, 3311.1m MD.

Fig. 3. Elemental maps interpreted as mineral composition showing typical microstructural association of blocky calcite veins with hydrothermal mineralization in damage zone samples. Dashed line labeled F is trace of foliation recognizable at section-scale.

a. Secondary pyrite and blocky vein-calcite sheared along a thin cataclasite band. The band is traced with white dashed line based on SEM image of mapped area. Sample G13, 3188.6m MD.

b. Secondary pyrite overprinting blocky calcite sheared along foliation (see inset box in Fig. 2d). Note euhedral forms in pyrite (inset SEM-SE image). The area within dashed line (cCal) is a clast with calcite vein fabric related to pressure solution cleavage. Sample G24, 3193.7m MD (~3m SW of SDZ).

c. A vein fragment comprised of prismatic anhydrite crystals (anh) and strongly twinned blocky calcite (cal). Sample G41, 3295m MD (~1.5m SW of CDZ).

d. Growth of pyrite and apatite inclusions in strongly deformed blocky calcite vein. Sample G52, 3301.34m MD.

Fig. 4. Paired CL-PPL images showing microstructures of blocky and syntaxial calcite veins in SDZ-side damage zone of the SAF. Where present at section scale, trace of foliation (F) is shown with a dashed line.

a. Cross-cutting blocky and syntaxial elongate calcite vein generations (thick arrow) in highly fractured, non-foliated siltstone. A thin arrow shows blocky veins sealing a micro-jog. Sample G13, 3188.60m MD.

b. Blocky calcite vein generations deformed by local dextral shear and overprinted by syntaxial crack-seal veins along extension cracks (brighter CL). Block-in-matrix foliated siltstone-shale cataclasite. Sample G22, 3192.51m MD.

C. Blocky calcite veins offset along a set of R-shear microfractures and overprinted by syntaxial crack-seal veins of variable CL. Area within rectangular box shows dark and light CL veins mutually overprint. Thick arrows point to possible pressure solution seams in calcite veins. Intensely foliated siltstone-shale cataclasite (black gouge). Sample G24, 3193.70m MD.

d. Calcite-vein fabric with anhydrite inclusion (Anh) at high angles to foliation in a large siltstone clast (see inset box in Fig. 2e for microstructural context). Thick, bent e-twins are present in the large blocky vein. Arrow points to an example of mutual crosscutting of calcite veins with dark and light luminescence. Sample G32, 3198.6m MD.

Fig. 5. Paired CL-PPL images showing microstructures of blocky and syntaxial calcite veins in CDZ-side damage zone of the SAF. Where present at section scale, trace of foliation (F) is shown with a dashed line.

a. Sample G41 ~1.5m SW of CDZ showing blocky veins with anhydrite inclusions (Anh). Mechanical twins with different lamellae thickness and spacing are present (inset boxes marked on CL and PPL images). The image is typical of 5 sections from two G41 core billets at 3295m and 3295.13m MD in banded siltstone.

b. An open-cavity blocky growth with distinct areas of light and dark luminescence zoning. Note network of thin crack-seal veins with brighter luminescence extending from margins into interior of the vein. Clear examples of crosshatched, tapering, and gently bent e-twin types are shown in inset boxes marked on PPL and CL images. Note tight lamellar spacing of the twins throughout. Foliated siltstone-shale. Sample G45, 3299.3m MD.

c. Showing blocky elongate type veins with mostly thin, tabular e-twins. Note patchy luminescence zoning. Foliated siltstone-shale. Sample G47, 3300.0m MD.

d. Strongly deformed blocky veins (see inset box in Fig. 2g) with a variety of e-twin lamellae structures. On CL image, cross-cutting relationship indicates at least 3 vein generations with latest generation having brighter luminescence. Note open cavities (arrows) in bright-color veins. Foliated siltstone-shale. Sample G52, 3301.34m MD.

e. Blocky veins (mainly on the right side) cut across antitaxial fibrous veins with pressure solution seams (arrows). Tabular and thick twin lamellae types are present in blocky calcite. Foliated siltstone-shale. Sample G56, 3305.4m MD.

f. Showing blocky veins seal a sheared jigsaw texture. Shear along an R' plane (dashed line) and implosion-driven extension (arrows) are consistent with stress field depicted on PPL image. Foliated siltstone-shale. Sample 65, 3311.1m MD.

Fig. 6. Paired CL-PPL images showing microstructures of blocky and syntaxial calcite veins in active creep zones CDZ and SDZ. Trace of foliation recognizable at section scale is shown with a dashed line labeled F.

a-b. CL images of blocky calcite veins seal implosion jigsaw textures in two different areas on the same thin section in SDZ sample. Inset close-up views on PPL images show presence of a variety of e-twin lamellae in blocky calcites including thin, tabulated thick, and thick with tapered bent and lensoid types. Note patchy calcite luminescence (white arrows). The gouge is mostly composed of altered and deformed serpentinite phases. Sample G27, 3196.70m MD.

c. A segment along length of a thick blocky vein in CDZ crosscut by a set of calcite-sealed extension veins with dull luminescence. The latter veins do not extend into surrounding serpentine-rich gouge matrix (Serp) but merge with mesh-like veins (M) on the right. Note string of open cavities along a bright-colored vein that seals a late extension crack (arrow on CL image). Sample G44, 3298.3m MD, collected from within serpentinite block.

d. Showing one of several fluidized gouge injections across quartzo-feldspathic bands (QFc) that run parallel to foliation in CDZ sample. Injection conduit is mostly sealed by blocky calcite growths, ~50µm in average grain size, with gouge fragment inclusions. Note calcite generation with dull luminescence (arrows on CL image). Injection flow lines in clay-rich gouge (CG) could be seen at opening end and along injection walls. Sample G44, 3298.3m MD.

Fig. 7. Fluidized gouge injection microstructures in CDZ sample (G44, 3298.3m MD). Trace of foliation is shown with dashed line F.

a. Gouge injection microstructure with aspect ratio of 0.25 (INJ G44A in Table 1) shows an injection from left to right at high-angles to foliation shown. Image is an optical XPL mosaic. Plain white and yellowish areas of the image are respectively voids filled with resin (labeled arrow). Brown and black areas within the injection conduit are extremely fine-grained Mg-rich clay gouge. QFc is foliation-parallel quartzofeldspathic bands of cataclasites. Serp is serpentinite-derived phyllosilicate phases.

b. BS-SEM mosaic image partially covering the injection area (inset box in a). Clay-rich gouge fills injection conduit lined with blocky calcite growth. Intruding gouge grades from coarse at the opening to extremely fine-grained at the tip of injection microstructure. Note chambered structure of the injection conduit involving cross-conduit calcite growth.

c. BS-SEM image (inset box in b) showing close-up view of extremely fine-grained conglobate clay gouge (CG) in mid-section of the injection. Injection-wall sequence along double-headed arrow consists of calcite-sealed quartzo-feldspathic microbreccia, and old foliation-parallel quartzo-feldspathic cataclasite band (QFC) at the bottom. A chrome-spinel porphyroblast (Cs), deformed by brittle fracture, is shown by black arrow. At the top side, calcite-sealed microbreccia includes large feldspar (Fl), and quartz (Q) clasts.

d. A small reworked injection microstructure across quartzofeldspathic cataclasite band. Areas in black are void spaces. Note foliation-parallel cluster of pyrite framboids (Py) crosscut by this injection microstructure.

Fig. 8. Composition map and CL image of fluidized gouge injection microstructure (G44A, INJ. A, in Table 1) in CDZ sample.

a. Interpreted elemental map showing microstructural relationship between blocky calcite growth and injected serpentinite-rich gouge.

b. CL image revealing spatial interaction of calcite from different generations involved in fluidized gouge injection. Three generations of calcite growth, labeled GEN 1-3, could be identified via a combination of luminescence contrast and crosscutting relationship. Injection wall (white border line) is lined with latest calcite generation, GEN 3, that crosscuts earliest generation, GEN 1, calcite. Isolated pixel color tiles of the 3 calcite generations are shown on the right. White dots on the image are 83 EDS data collection spots. Inset box is location of EBSD images shown in Figs. 9b-c.

Fig. 9. The trace-element concentration and EBSD analysis of blocky calcites involved in fluidized gouge injection microstructure shown in Fig. 8.

a. Ternary plot of Mean trace-element concentrations; individual plots on the right with GEN 3 being the latest calcite vein generation.

b. EBSD-derived phase map (red = calcite, cyan = quartz) of area within Fig. 8b inset box. Two apparently separate GEN 1 twinned calcite grains are highlighted in yellow. White dashed line in b and c separates GEN1 calcite veins from GEN3 calcite that lines injection structure. Dotted white line in b and c is a GEN3-parallel quartz vein that separates the two parts of GEN 1 calcite grain highlighted in yellow. Note the well-developed e-twins in GEN1 calcite grains (parallel black lines) and their absence from GEN3 calcite grains.

c. EBSD-derived grain reference orientation deviation (GROD) map of area in b (blue = 0°, red = 25°). Note that GEN1 calcite domains have high GROD values (up to 25° in the highlighted grain) indicating a high level of lattice distortion within the grains, whereas GEN3 calcite grains, across the dashed line, have low GROD values indicating little or no lattice distortion within the grains. Quartz grains in the quartz vein (dotted line) have low GROD values indicating little or no lattice distortion. Also note the well-developed e-twins in GEN1 calcite grains (parallel white lines) and their absence from GEN3 calcite grains.

d. Lower-hemisphere pole figures for the two highlighted GEN 1 calcite "grains" in image b. Note that the two grains have the same lattice orientations, consistent with being originally part of the same calcite grain.

e. Lower-hemisphere pole figures for grains in quartz vein that separates GEN1 calcite grain in b and c. Note that the twelve quartz grains identified as part of the vein in c have a restricted range of c-axis directions oblique to the vein trace, while m <10-10> and a <11-20> axes define a broad girdle. Colors are in the IPF space.

Fig. 10. Across-the-fault variations in composition of blocky, elongate blocky, and syntaxial calcite veins with mean sampling frequency of ~1.6 m, excluding the coring gap (data from Table 2a). Active creep intervals SDZ and CDZ are indicated by shaded vertical bars. Error bars

are Standard Error of sample population. Short vertical double lines on x-axis are approximate location of minor faults transferred from Fig. 1.

a. Changes in mean value of Mn/Fe ratio. Open-circle symbols with different sizes represent mean Mn/Fe ratio for gouge-injection calcite vein generations in CDZ interval (data from Table 2b). GEN 3 is the latest generation.

b. Changes in mean value of Mg/Ca ratio. The open circle symbols in CDZ interval represent mean Mg/Ca ratio for gouge-injection calcite vein generations (data from Table 2b). Inset scattergram showing a generally negative correlation between Mn/Fe and Mg/Ca ratio (Table 2 ratio columns, excluding G44inj. data).

Fig. 11. Ternary plots showing changes in trace element composition in blocky calcite veins with distance from the active-creep intervals SDZ and CDZ (excluding data from injection-related calcite veins).

Tables

Table 1. Aspect ratio data for gouge injection microstructures a, b, and c as they appeared on parallel petrographic thin sections A, B, and C through the CDZ core sample billet, cut parallel to each other, perpendicular to foliation.

Sample	INJ.	L, mm	W, mm	W/L
G44 A	a	5.651	1.352	0.25
G44 A	b	3.616	1.446	0.40
G44 A	C	2.486	1.243	0.50
G44 B	a	3.653	0.913	0.25
G44 B	b	4.762	3.524	0.74
G44 C	a	4.491	1.078	0.24
G44 C	b	3.685	1.179	0.32

Table 2. Mean atomic wt.% Mg, Fe, Mn, and Mg/Ca and Mn/Fe values (mean of the ratios) from spots on CL images of calcite veins in all samples. Values in second row for each sample is Standard Error. **a.** Mean values for N spots in typical calcite veins in each sample. **b.** Individual and combined mean values for N spots in calcite generations (GEN 1-3) related to sample G44 gouge injection microstructures (see INJ. a, sample G44A, Table 1). GEN 3 is the latest generation.

2a

Sample	Mg	Fe	Mn	Mg/Ca	Mn/Fe	N
G65	**0.053**	**0.081**	**0.352**	**0.003**	**4.837**	**53**
	0.005	0.005	0.011	0.000	0.185	
G61	**0.039**	**0.096**	**0.344**	**0.002**	**5.220**	**27**
	0.003	0.027	0.014	0.000	0.305	
G56	**0.051**	**0.087**	**0.410**	**0.003**	**5.536**	**34**
	0.003	0.010	0.022	0.000	0.394	
G52	**0.082**	**0.049**	**0.093**	**0.004**	**2.676**	**66**
	0.006	0.003	0.003	0.000	0.240	
G51B	**0.067**	**0.030**	**0.055**	**0.005**	**2.500**	**36**
	0.006	0.003	0.002	0.000	0.267	
G47	**0.127**	**0.070**	**0.088**	**0.007**	**1.700**	**19**
	0.016	0.008	0.005	0.001	0.257	
G46	**0.118**	**0.074**	**0.105**	**0.006**	**2.364**	**27**
	0.013	0.011	0.005	0.001	0.299	
G45	**0.098**	**0.047**	**0.079**	**0.006**	**2.961**	**37**
	0.009	0.005	0.003	0.001	0.431	
G44	**0.718**	**0.152**	**0.144**	**0.044**	**1.290**	**30**
	0.168	0.013	0.010	0.012	0.208	
G41	**0.164**	**0.046**	**0.150**	**0.008**	**3.398**	**29**
	0.014	0.003	0.006	0.001	0.122	
G32	**0.138**	**0.133**	**0.130**	**0.007**	**1.176**	**20**
	0.022	0.013	0.019	0.001	0.177	
G28	**0.138**	**0.044**	**0.021**	**0.007**	**0.646**	**44**
	0.022	0.005	0.001	0.001	0.056	
G27	**0.078**	**0.039**	**0.043**	**0.004**	**1.467**	**41**
	0.022	0.006	0.004	0.001	0.136	
G24	**0.064**	**0.062**	**0.079**	**0.005**	**1.568**	**35**
	0.008	0.006	0.005	0.001	0.156	
G22	**0.152**	**0.170**	**0.141**	**0.008**	**1.095**	**22**
	0.060	0.035	0.006	0.004	0.099	
G13	**0.134**	**0.121**	**0.184**	**0.007**	**1.622**	**24**
	0.012	0.008	0.010	0.001	0.103	

2b

Vein	Mg	Fe	Mn	Mg/Ca	Mn/Fe	N
GEN 1	**0.331**	**0.185**	**0.097**	**0.018**	**0.578**	**32**
	0.048	0.009	0.007	0.003	0.081	
GEN 2	**0.827**	**0.154**	**0.161**	**0.047**	**1.631**	**28**
	0.151	0.022	0.010	0.010	0.227	
GEN 3	**0.245**	**0.060**	**0.120**	**0.013**	**3.196**	**23**
	0.052	0.011	0.007	0.003	0.407	
combined	**0.475**	**0.140**	**0.125**	**0.026**	**1.659**	**83**
	0.062	0.010	0.006	0.004	0.180	

A study of fluid overpressure microstructures from the creeping segment of the San Andreas Fault

Jafar Hadizadeh [a] *

[a] Department of Geographic & Environmental Sciences, University of Louisville, Louisville 40292 KY, United States.

hadizadeh@louisville.edu

Office: 502-852-2691 and mobile: 502-457-5672

Alan P. Boyle [b]

[b] Department of earth, ocean and ecological sciences, University of Liverpool, Liverpool, L69, United Kingdom.

apboyle@liverpool.ac.uk

Andrea E. Gaughan [a]

[a] Department of Geographic & Environmental Sciences, University of Louisville, Louisville 40292 KY, United States.

ae.gaughan@louisville.edu

KEYWORDS

Coseismic microstructures; Calcite veins; Calcite trace elements; Cataclasis; Aseismic creep; Calcite Cathodoluminescence.

Abstract

Evidence of episodic fluid overpressure events noted in samples from the San Andreas Fault Observatory at Depth (SAFOD) have remained largely uncorrelated in terms of their collective significance for seismic history of the fault zone. The compositional and microstructural correlations sought in this study could shed light on questions about potential for major seismic events in the creeping segment of the SAF in central California. We used quantitative energy dispersive spectroscopy (EDS), Cathodoluminescence (CL) and Scanning Electron Microscope (SEM) imaging, and electron backscatter diffraction (EBSD) analysis to acquire geochemical and microstructural data from a suite of twenty SAFOD core samples including the damage zone and the active core of the fault. The results indicate intermittent coseismic fluid overpressure events that overprint the background aseismic creep across the fault. Analysis of trace elements and deformation in the coseismic calcite vein generations and their associated hydrothermal mineral phases indicate progressive uplift and exhumation followed by an asymmetric excursion of meteoric water into the damage zone. The same analysis suggests that the actively creeping intervals act as permeability barriers. Our results are in overall agreement with recent studies of the SAF in central California that indicate large seismic events have occurred intermittent with aseismic creep in recent geological time or suggest future potential for such events.

1. Introduction

A collection of wide ranging analytical and experimental studies of core samples from the San Andreas Fault Observatory at Depth (SAFOD) shed light on microstructural, geochemical, and mechanical aspects of aseismic creep along the central section of the San Andreas Fault zone (SAF). Microstructures of fluidized gouge injection, calcite-sealed jigsaw textures, and various types of blocky calcite vein growths, mostly in samples from the SAF damage zone, have been reported in previous studies (e. g., Schleicher et al. 2009; Holdsworth et al. 2011; Gratier et al. 2011; Rybacki et al. 2011; Mittempergher et al. 2011; Hadizadeh et al. 2012; Janssen et al. 2010 and 2014; Bradbury et al. 2015, Hadizadeh et al. 2018). In most cases such observations have been attributed to local transient fluid overpressure events, possibly related to deformation by pressure solution creep or to repeating microearthquakes in the relatively inactive SAF damage zone. There are, but fewer, reports of fluid overpressure microstructures in the actively creeping core of the SAF (e.g., Moore and Rymer 2012; Luetkemeyer et al. 2016). These studies along with geophysical data and historic records of the region's seismicity have provided grounds for raising questions about potential for major seismic events (M>6) in the creeping segment of the SAF in Central California (Noda and Lapusta 2013; French et al. 2014; Jolivet et al. 2014; Harris 2017). Maurer and Johnson (2014) noted that the 150 km long central section of the SAF has not produced a large earthquake historically. Most recently Coffey et al. (2022) used thermal maturity of a suite of biomarkers (also see Sheppard et al. 2015) and K/Ar ages in the SAFOD core samples to search for paleoseismic events in the creeping section of the SAF. The study concluded that certain intensely sheared domains in the SAFOD black gouge (foliated siltstone-shale cataclasites-Fig. 1) have experienced abundant seismicity over the past 16 million years.

While there is ample microstructural evidence of possibly-coseismic fluid overpressure in the SAFOD samples, studies to correlate these observations across the active fault core have been scarce mainly because, 1) the SAFOD samples show that there are significant compositional differences between the damage zone and the active core of the SAF (Holdsworth et al. 2011; Moore 2014; Morrow et al. 2014), and 2) the results of experimental and mechanical studies show that the serpentinite-rich gouge in the SAF core is velocity strengthening (Lockner et al 2011; Carpenter et al. 2009, 2011, 2012). Furthermore, the ongoing debate about reliability of brittle microstructures as coseismic slip indicators (e.g., Cowan 1999; Smith et al. 2008; Stunitz et al. 2010; Boutareaud et al. 2008) makes it difficult to argue that presence of blocky calcite veins, for example, indicate earthquake events in a phyllosilicate-rich aseismic creep zone. The objective of this study is to seek compositional, and microstructural correlations between fluid overpressure microstructures across the damage zone and active creep intervals of the SAF by examining a relatively large number of the SAFOD phase-3 core samples.

2. Methods

2.1 The samples and sample preparation

We present results of a geochemical and microstructural study of 20 samples from the SAFOD phase 3 drilling, spanning ~125m Measured Depth across the fault core. The sample billets were requested from the SAOD drill core collection at Gulf Coast Repository in College Station, Texas. The lithostructural units, sampling locations along the core sections 1-6, and the exact measured depth (MD) for each sample is shown in Fig. 1. The samples were selected to represent zones of moderate to intensely foliated gouge in the SAF damage zone and the actively creeping intervals: ~1.61 m-wide southwestern deforming zone (SDZ) and ~2.6m-wide central deforming zone (CDZ). The selected samples are mainly within the damage zone as defined by a zone of low P and S-waves recorded along the SAFOD main borehole (Zoback 2011-Figs. 4a-b). However, the samples were also selected to show the considerable deformation that occurs ~10m further SW the SDZ within the siltstone shale units bordering the SDZ. Here, the sample material outside the bounds of the SDZ and CDZ (Fig. 1 caption) is simply considered part of the fault damage zone, where deformation could be recognized at scales 0.1m or less on a standard petrographic thin section. In Fig. 1, the approximate position of several minor fault zones, mainly along the lithologic boundaries (e.g., reported by Holdsworth et al. 2011) are also marked, where they appear mostly concentrated within the foliated siltstone-shale lithostructural units. The drill site, scope, and geophysical well-log details of the SAFOD project (Hickman et al. 2004; Zoback et al. 2011) and protoliths of the damage zone lithostructural units are described elsewhere (Holdsworth et al. 2011; Janssen et al. 2014; Bradbury et al. 2015).

We used point-cloud imaging technique to render precise 3D images of the billets prior to physical sectioning in order to preserve a virtual copy of each billet’s surface color, texture, morphology, and reference markings. The images, viewable in Microsoft 3D Viewer, were helpful in accurate sectioning of the billets as well as resectioning previously cut billets (see

Holmes et al. 2021). The sample billets were impregnated with clear epoxy resin and cut along 3 mutually perpendicular planes with the reference plane at ~90° to clearly traceable foliation at the billet scale. The billets with no visible trace of foliation were cut at 3 mutually perpendicular planes with the core orientation marker as the reference. The SEM-polish petrographic sections were surface machine-polished using 0.05 µm silicon particle colloidal suspension and each gold-sputtered for 60-75 seconds using a Cressington 108 Sputter Coater.

2.2 Imaging and analytical work

Microstructural features of interest in the samples were preliminarily studied in whole-section mosaics assembled by optical microscopy in crossed polarized light (XPL) and plane polarized light (PPL). Typical deformation microstructures of interest on the mosaics were selected for detailed electron imaging and analytical data collection. Our investigations of the SAF damage zone samples were inadvertently more focused on deformation and fluid-overpressure microstructures in gouge samples from the foliated and non-foliated siltstone-shale lithostructural units, which have been inferred to share the Great Valley Group as their protolith. However, we note that tracking evidence of deformation affecting the same/similar protoliths across the active core of the fault served to make comparisons of the features and modes of deformation more valid.

Backscatter and secondary electron images of deformed and undeformed microstructures were taken using an FEI Nova 600 FEG field emission scanning electron microscope (SEM) at 10-15 KV accelerating voltage and working distances ranging 3.5-5 mm. The electron backscatter diffraction (EBSD) analysis was conducted at the University of Liverpool using a Zeiss Gemini

450 SEM with a thermionic field emission gun, an accelerating voltage of 20kV, and a beam current of ~5 nA. We used Cathodoluminescence (CL) imaging and luminescence contrast in calcite vein networks in the samples to qualitatively differentiate the fluid source REDOX properties and relative order of the calcite vein generations. The CL results were constrained and correlated with the calcite vein EDS results as well as with the EBSD analysis of the hydrothermal phases associated with the same calcite vein networks (e.g., secondary pyrite, anhydrite, quartz). The CL images were acquired using a CITL-Mk5 cold CL stage system with exposure time between 0.5 and 10s to maximize dynamic range in the acquired images.

The atomic weight% of major and trace element composition of calcite veins in 16 samples were acquired using a Bruker Quantax Energy Dispersive Spectrometry (EDS) analyzer in an Apreo-C low vacuum field emission SEM microscope at accelerating voltage of 30kV. The measurements were made on one or more spots from each calcite vein generation, as could be determined based on CL color contrast in a vein network microstructure. Each measurement included the major and trace elements in calcium carbonate (Ca, O, C, Mg, Mn, Fe). This EDS data collection plan accounts for the sample-to-sample difference in the total number of measurement spots shown in Table 2. Additional elements S, Si, Al, K, and Na were included in each measurement to account for our preliminary observations of other phases in the sample calcite vein networks (e.g., pyrite, anhydrite, quartz, and siliciclastic inclusions). Mineral composition maps were created by interpreting elemental maps we acquired using the EDS detector analyzer. The elemental mapping targeted microstructures that showed interaction of various hydrothermal phases with blocky calcite vein networks. The EDS measurements were preferably focused on collecting data from the blocky and syntaxial calcite veins and as much as possible avoiding the antitaxial calcite vein fabric related to pressure solution cleavage in the samples. This preference was likely to provide calcite vein composition data relating to coseismic advective fluids rather than to fluids involved in aseismic diffusive mass transfer processes consistent with creep rates (Gratier et al. 2003, 2011).

3. Results

3.1 Deformation microstructures in the SAF damage zone

The typical deformation microstructures shown in Fig. 2 were selected from samples SW and NE of the SDZ (SDZ-side) and samples SW and NE of the CDZ (CDZ-side). We note that gouge zones on either side of the 95m coring gap in the SAFOD phase 3 lateral borehole G (Fig. 1) are interspersed with bands of less deformed but highly fractured protolith rocks, which are not included in Fig. 2. Deformation of the SDZ-side damage zone grades from moderately deformed, foliated block-in-matrix gouge at 3187.3m MD (Fig. 2a) to intensely foliated siltstone-shale cataclasites and ultracataclasites at 3193.7m MD ~2.8m southwest of the SDZ (Fig. 2c). The latter units are also known as 'black gouge' or 'black fault rock' in other SAFOD sample studies (e.g., Holdsworth et al. 2011; Bradbury et al. 2015; Coffey et al. 2022). The observed increases in deformation intensity may also be coincident with the presence of minor faults (thick black arrows in Fig. 1) as well as proximity to the SDZ. At core-sample scale, the foliation is mainly defined by variable intensity pressure solution cleavage and shape preferred orientation (SPO) of survivor quartzofeldspathic clasts in a matrix of siltstone-shale ultracataclasites. This general description is typical of the intervals labeled '*foliated siltstone-shale with block-in-matrix fabric* and *foliated siltstone-shale cataclasite with veins'* in Fig. 1, consistent with microstructural descriptions in previous studies (e.g., Holdsworth et al. 2011; Gratier et al. 2011; Hadizadeh et al. 2012; Bradbury et al. 2015). Microscopy reveals microstructures characteristic of deformation by cataclasis as well as pressure solution (Figs. 2a-c). The evidence of pressure solution varies from impingement dissolution of block contacts (Fig. 2a) in the block-in-matrix gouge to the development of a pervasive fabric of antitaxial calcite veins (here referred to as calcite fabric) at high angles to the solution cleavage and clast SPO in indurated quartzofeldspathic cataclasite (Fig. 2b). Microstructures of deformation by pressure solution in the same interval of the SAFOD cores are described in more detail by Gratier et al. (2011), and Richard et al. (2014). A microstructural example of alternating pressure solution and cataclastic deformation mechanisms is shown in Fig. 2c, where ultracataclasites are developed across a sheared quartzofeldspathic clast (dark streaks in small inset box). The BS-SEM image of the ultracataclasite shows that it includes reworked fragments of the calcite fabric (areas circled by dashed lines in Fig. 2c). In the same sample, a polycrystalline mass of secondary pyrite (Fig. 2d) is sheared along the foliation and appears unaffected by pressure solution. The sample directly bordering the SDZ on the NE side (G31) is mostly an undeformed fractured siltstone (not shown) while sample G32, ~1m further NE of the SDZ consists of foliated siltstone-shale cataclasites (Fig. 2e).

On the CDZ-side, typical deformation microstructures are selected from a suite of 8 samples presented in Figs. 2 f-h. A readily noted overall observation is the relative absence of intense and pervasive pressure solution cleavage and calcite fabric in this series of samples compared to those described for the SDZ-side damage zone. Evidence of deformation by pressure solution is present as local impingement dissolution in deformed vein-calcite and the quartzofeldspathic clast contacts within cataclasites and ultracataclasites (fig. 2f). The minor faults reported by Holdsworth et al. (2011) are also present in this section of the SAF damage zone close to our samples G51 and G52 (see Fig. 1). In sample G52, micro-folding of thick blocky calcite veins along foliation in ultracataclasite gouge matrix (Fig. 2g) is a remarkable example of intense deformation by cataclastic flow and development of cataclastic foliation in the CDZ-side damage zone. A close-up SEM image in Fig. 2g (large inset box) shows typical ultracataclasite matrix intrusion into tensile cracks in the folded blocky calcite veins. Microstructures in Fig. 2g demonstrate how blocks in a block-in-matrix gouge could be formed solely by deformation of calcite veins as well as by attrition of reworked quartzofeldspathic blocks. The presence of pressure solution in foliated cataclasite is shown in sample G65 at a distance of ~12m MD NE of the CDZ (Fig. 2h). In the same sample, we find a gouge injection microstructure with exceptionally large (>1) aspect ratio. The relative lack of calcite veins despite the presence of the fluidized gouge injection in this sample is notable since only a few thin strands of blocky calcite veins could be found near the tip of the injection in Fig. 2h. We also note that bending of the injection wall is accommodated through micro-scale displacements along bands of siltstone cataclasites. The growth and deformation of blocky calcite veins, unrelated to pressure solution cleavage were found to be associated with hydrothermal neo-mineralization of pyrite, anhydrite, apatite, and quartz throughout the damage zone gouge samples. In Fig. 3a-d we present interpreted elemental maps to typify these associations.

3.2 Cathodoluminescence of calcite veins in the damage zone

The CL imaging was focused on the spatial distribution of vein generations in blocky and syntaxial type calcite veins in both the damage zone and the active core of the fault. The imaged areas were selected based on a careful survey of whole-section plane-polarized (PPL) optical images. This referencing provided CL-PPL image pairs (Figs. 4,5, and 7), which allowed visual identification of microstructural boundaries of e-twinned areas and different types of e-twins on each CL image.

In general, the images from samples SW of the SDZ (Fig. 4a-c) indicate a noticeable increase in deformation intensity with proximity to minor fault zones marked in Fig. 1 and the black gouge (sample G24, 3193.7m MD-Fig. 1). The increasing deformation intensity is well represented by decreased spacing and microfaulting of calcite veins in Fig. 4b, compared to Fig. 4a. Multiple cross-cutting calcite vein generations are offset by shear displacement along microfractures in sample G24 ~2.8m MD from the SDZ (Fig. 4c). The CL images made it possible to depict, with reasonable confidence, some kinematic elements of local brittle deformation such as Riedel shear orientations (compare PPL and CL images in Figs. 4b-c). The sections from sample G31, ~0.3m MD NE of the SDZ (not shown) are almost devoid of calcite veins while sample G32 ~1.2m MD, farther NE of the SDZ (Fig. 2e) is a fine-grained foliated clast-in-matrix siltstone cataclasite. The calcite vein fabric in sample G32 is shown in the CL-PPL pair of Fig. 4d. Close inspection of the CL images in Fig. 4c (inset box) and 4d (white arrow) showed clear examples of mutually-crosscutting calcite veins with dark and light luminescence.

Across the coring gap, the SAF damage zone samples G41 and G42, SW of the CDZ, show some similarities with G31 and G32 samples NE of the SDZ in terms of general types and spatial density of calcite veins, presence of anhydrite clusters, and hydrocarbon stains in the gouge. The calcite veins in sample G41 (~1.5m SW of CDZ) are mostly blocky elongate type with anhydrite inclusions (Fig. 5a PPL image). Twin lamellae types (Fig. 5a PPL image) include densely spaced thin and lensoid types. The thick tabular type twins were mostly found in contact with anhydrite inclusion growths. We found few to no calcite veins in sample G42 (not shown). NE of the CDZ, there is a general increase in overall volume (vein thickness) and spatial density of calcite veins as multi-generation cross-cutting vein microstructures. The thick blocky calcite vein in sample G45 ~0.2m MD NE of the CDZ includes twin lamellae types indicative of twinning at elevated temperatures (Ferrill et al.2004; Lacombe et al. 2021) shown in Fig. 5b PPL image. On the CL image in Fig. 5b, a bright (margins) and dull (center) calcite luminescence zoning is noted and calcite-sealed cracks with brighter luminescence extend from the vein margins into the center of the vein. A bright/dull patchy luminescence is also noted in sample G47, at ~0.9m NE of the CDZ (Fig. 5c). However, unlike the preceding sample, the e-twin lamellae are of uniform type in areas of light and dark luminescence (Fig. 5c-PPL image). Intense ductile deformation of vein-calcite could be observed in sample G52 (Fig. 5d) ~0.2m from the minor fault zone at 3301.5m MD (see Fig. 1). The folded blocky calcites are further crosscut by relatively undeformed bright CL vein generations with open microcavities (arrows in Fig. 5d-CL image). The sample G56 shows antitaxial fibrous veins with pressure solution seams are crosscut by blocky calcite veins (Fig. 5e). Further away from the CDZ, the ductile shear of calcite in a calcite-sealed implosion jigsaw texture is shown in sample G65 at ~12.1m MD from the CDZ (Fig.5f). We note that the relative disposition of the fragments in the jigsaw texture indicate only small apparent shear strains for the area viewed in Fig. 5f.

3.3 Blocky calcite veins and injection microstructures in the SDZ and CDZ

The CL images provide clear evidence of calcite-sealed jigsaw texture (Fig. 6a-b) that may represent implosion microbreccias in the SDZ sample. The calcite e-twin types in this case tend to vary widely from sparse thin type to, thick bent, and lensoid types over mm-scale distances (inset boxes in Fig. 6a-b). While an absence of cross-cutting veins in Fig. 6a-b indicates a single event of blocky calcite growth, luminescence of the calcite is randomly non-uniform throughout the sealing mesh (white arrows in Fig. 6a-b). The CDZ sample consists of anastomosing serpentinite and quartzo-feldspathic clasts stretched along foliation. Blocky calcite growths are found within both these clasts (e.g., Fig. 6c). It is important to note that the clast blocky calcites predate the calcite veins associated with more recent alteration rind of the serpentinite block from which the sample was collected. The youngest calcite veins associated with the CDZ gouge injection microstructures, however, post-date the clast calcites since the injections crosscut the foliation in our sample. The CL image in Fig. 6c shows a thick blocky calcite vein is crosscut by a set of thin dull CL calcite veins that seal extension fractures at high-angle to foliation. The latter veins are further crosscut at a slightly different angle by a bright CL vein with medial open microcavities (white arrow in Fig. 6c). The CDZ sample also hosts a number of fluidized gouge injection microstructures (e.g., Fig. 6d), not found in our two SDZ samples. More detailed observations from clearly identifiable gouge injection microstructures, including the one shown in Fig.6d, are provided in the following.

The fluidized gouge injections in sample G44, without exception, formed at high angles to foliation. Parallel sectioning of the sample's core billet at~5 mm intervals enabled a limited study of change in dimension of 3 different injections. The aspect ratio (width W/length L) for individual injection was determined following the procedure used by Rowe et al. (2012). Table 1 shows 7 different aspect ratios for the 3 injections since only two of the three injections were clearly traceable in the sequence of 3 parallel thin sections. The W/L ratio of the injections in sample G44 ranged from 0.24 to 0.74 with a Mean of 0.39. The data in Table 1 show only slight variations in depth and width of the injections over a ~20x40x25 mm measurement volume. The largest of the 3 injection microstructures (INJ-a in Table 1) shown in Fig. 7a, is characterized by a well-defined gouge-filled conduit with relatively straight walls. The close-up BS-SEM image across the injection (Fig. 7c) shows the blocky nature of the wall-lining calcite, globulated microstructure of the injected clay-rich gouge matrix within the injection conduit, and a symmetric compositional sequence across the injection walls. Fig. 7d exemplifies several other smaller deformed injection microstructures in the CDZ sample for which we could not obtain reliable aspect ratios. The calcite veins within quartzofeldspathic and serpentinite-rich clasts (exemplified in Fig. 6C) as well as GEN 1 veins in the injection conduit should predate the injection events as they are cross-cut by the injection microstructure. Elsewhere in our samples, only a single injection-like microstructure with an exceptionally large aspect ratio of 1.22 was found in sample G65 (Fig. 2h), ~14 m NE of the CDZ.

An interpreted EDS elemental map of the injection conduit (Fig. 8a) indicates that a calcite-sealed microbreccia wall was developed during fluidization of Mg-rich clay gouge. The map also shows that multiple gouge-filled chambers, partially separated by calcite-sealed microbreccia, are present within the injection conduit. On the CL image in Fig. 8b, we could identify 3 generations of calcite growth based on CL color contrast and cross-cutting relationship, here named GEN 1, GEN 2, and GEN3 (youngest). Mean spectral wavelength for GEN1, GEN 2, and

GEN 3 are respectively 660 ± 5 nm, 634.6 ± 1.7 nm, and 624.5 ± 4.6 nm (N=5 per generation). The CL color contrasts between these values are represented by pixel-color tiles 1, 2, and 3 on Fig. 8b. While a relative age order for GEN 1 and GEN 3 could be established by crosscutting relationship seen on the CL image, the relationship between GEN 2 calcite and the other two generations is only based on differences in spectral values given above. Close inspection of the image also shows that GEN 2 and GEN 1 mutually overprint while GEN 3 overprints, or only contacts, GEN 2 in some areas (e.g., near the injection tip). The major and trace element data from calcite generations related to the largest gouge injection microstructure were collected from 83 spots shown in the Fig. 8b CL image mosaic and summarized in Table 2b. The ternary plot of Mg, Mn, and Fe (Fig. 9a) shows considerably higher Mn/Fe ratio in GEN 3 relative to GEN1 and GEN 2 while both GEN2 and GEN3 preserve a higher Mg concentration compared to GEN 1. Mean Mn/Fe ratio for GEN 1, GEN 2, and GEN 3 calcites is respectively 0.578, 1.631, and 3.196 (see Table 2b). In terms of deformation, the EBSD grain reference orientation deviation (GROD) map (Fig. 9c) and the inverse pole figure (IPF) in Fig. 9d show GEN 1 calcite has undergone significant intracrystalline strain. In comparison, the EBSD data for a quartz vein that co-crystallized with GEN 3 calcite (Figs. 9c and 9e) shows little cumulative deformation (blue colors in Fig. 9c) and a limited range of c-axis orientation oblique to the length of the quartz vein (Fig. 9e).

3.4 The trace element and Mg/Ca ratios in calcite veins

The variation in Mn/Fe ratio in the damage zone (Fig. 10a) is clearly asymmetric. The maximum mean Mn/Fe ratio on the CDZ-side damage zone is a factor of 3 times greater than those on the SDZ-side damage zone. The trend of high Mn/Fe ratios NE of the CDZ shows a noticeable drop between ~3305.4 m and ~3301.4 m MD, which appears to coincide with the presence of two of the minor fault zones. The fluctuations in Mn/Fe ratio in samples closer to the CDZ do not seem to correlate to the other two minor fault locations marked on Fig. 10a. at ~3301 m. The variations in mean Mn/Fe ratio on the SDZ side are too small to be meaningfully attributed to the minor faults marked on Fig. 10a, SW of the SDZ interval. The Mn/Fe ratios on the SDZ-side have a low sample-to-sample variation as well as being well below the CDZ-side maximum values. This general lack of variation in Mn/Fe ratios with distance from the SDZ could indicate inactivity and/or a lack of fluid pathways on the SDZ side of the fault. The inset scattergram in Fig. 10b as well as a visual comparison of the mean Mn/Fe and Mg/Ca curves in Fig. 10 reveals that an increase in mean Mn/Fe ratio is roughly matched with a drop in mean Mg/Ca ratio. This is prominently demonstrated in the CDZ interval with the highest mean Mg/Ca ratio. Mean Mn/Fe and Mg/Ca ratios in calcite vein generations related to the fluidized gouge injections in the CDZ interval (Table 2b), are plotted as open circles on Fig. 10 for comparison with these mean values elsewhere in the CDZ sample. The mean Mn/Fe ratio in the youngest (GEN3) and the oldest (GEN1) generations respectively plot well above and below the CDZ sample average. We note that mean Mn/Fe ratio for the GEN 3 injection calcites (3.196 ± 0.41) is more comparable to the average of means for the calcite veins in the 9 samples bordering the CDZ interval (3.465 ± 0.46) than mean Mn/Fe in the CDZ sample (1.29 ± 0.21).

Fig. 10b shows that mean Mg/Ca values in the damage zone, NE of the CDZ, steadily rise, from 0.003 to 0.006, over 11.8m distance toward the CDZ interval. The individual ratio measurements in the CDZ sample fluctuate widely from 0.003 to 0.328 with mean value of 0.044, which plots as a significant peak. The Mg/Ca ratio falls sharply to 0.009 at ~1.5m SW of the CDZ border. Mean values of the Mg/Ca ratio in the injection-related youngest (GEN 3) and oldest (GEN 1) calcites fall well below the range for the calcite veins in the CDZ sample while GEN 2 injection calcites plot within the CDZ sample average. The youngest injection calcites (GEN 3) have the lowest mean Mg/Ca ratio. The damage zone average of Mg/Ca mean values for the SDZ-side and CDZ-side are respectively 0.007 and 0.005. Notably, the average Mg/Ca ratio for the two SDZ samples is 0.005, not exceeding the damage zone's average.

The ternary plots in Fig. 11 show how the normalized proportions of the trace elements Mg-Fe-Mn in the blocky calcites vary in the damage zone over distances up to 16 meters from the two active creep intervals. The plots show a general increase in the relative content of Mg within the trace element trio in the samples closer to the active creep intervals. A notable difference in the trace element composition between the CDZ and SDZ side, regardless of distance from the active creep zones, is that the overall Fe concentration of the vein calcites is 10-15% lower on the CDZ side.

4. Discussion

4.1. Deformation mechanisms

Internal structure of the foliated quartzofeldspathic gouge in the SAF damage zone varies from being dominantly defined by pressure solution cleavage (Fig. 2b) to dominantly being an SPO-defined cataclastic foliation (Fig. 2d). An explanation is that the gouge is showing progressive transition from cataclastic foliation (Chester et al. 1985) to foliation via pressure solution creep in a maturing fault zone (Bos and Spiers 2001). However, evidence of reworked pressure solution microstructures in Fig. 2c indicates possible coupled deformation mechanism.

Rutter and Mainprice (1979) and Gratier (1999) suggested that removal of soluble phases by pressure solution in highly mature fault zones may result in recurring frictional behavior. More specifically, based on a diffusion-distance limited aqueous mass transfer model, Gratier et al. (2011) argued that episodic cataclasis might be required for aseismic creep via pressure solution. Gratier et al. (2011) and Richard et al. (2014) argued that deformation by pressure solution as the dominant mechanism is a viable creep mechanism throughout the entire seismogenic zone.

The current aseismic creep in the SDZ and CDZ intervals is believed to be mainly controlled by bulk ductile flow (highly distributed grain-scale frictional sliding) of low friction ($\mu<0.3$) serpentinite alteration products found mainly as saponite smectite (e.g., Jeppson et al., 2010; Holdsworth et al., 2011; Hadizadeh et al., 2012; Bradbury et al., 2015; Moore, 2014). Several studies suggest that deformation mechanisms operating at depths below the SAFOD may involve Mg-rich phyllosilicates (e.g., chlorite) that could result from metasomatic alteration of serpentinite at greater temperatures (e.g., Carpenter et al., 2012; French et al. 2015; Carpenter et al. 2015; Moore et al. 2016). Experimental friction shows that irrespective of internal microstructures, the phyllosilicate-rich products of aseismic creep in the SAF are strongly velocity strengthening (e.g., Hadizadeh et al. 2013; Coble et al. 2014; French et al. 2014; Carpenter et al. 2015).

4.2 Microstructures of transient fluid overpressure

The microstructures of aseismic creep in the damage zone of the SAF are overprinted by calcite-sealed jigsaw textures, crosscutting generations of blocky calcite veins, and fluidized gouge injections (Figs.4 and 5). Numerous studies suggest that these microstructures indicate coseismic transient fluid overpressure events (e.g., Sibson 1986; Otsuki et al. 2005; Boulier et al. 2004, 2009; Mittempergher et al. 2011; Lin 2011; Rowe et al. 2005, 2012; Janssen et al. 2010, 2015; Smeraglia et al. 2017; Scuderi et al. 2017; Spruzeniece et al. 2021; Gu et al. 2021). The implosion microbreccias sealed by blocky calcite growths were found in the damage zone samples ~4m SW of the CDZ (e.g., Fig. 4b) and as far as ~12m NE of the CDZ (e.g., Fig. 5f). The highest densities of multi-generation blocky calcite vein networks in the damage zone (e.g., Fig. 4 b-c, Fig. 5d) were observed in samples within ~4m SW of the SDZ boundary and 2.2m NE of the CDZ boundary. The results show that the blocky calcite vein generations have been deformed by subsequent creep on the fault (Fig. 4b and Fig. 5d, 5f). The cross-cutting relationship in CL image of Fig. 5d shows new blocky calcite veins overprint earlier-generation veins deformed by folding at high-angles to foliation within the creeping gouge matrix. However, we must note that the type, spatial distribution, and deformation of calcite veins for the damage zone in the coring gap between the two SAFOD active creep intervals are unknown (Fig. 1).

The CL color spectrum in calcite is mainly the result of changes in trace concentration of Mn and Fe respectively as luminescence enhancer and luminescence quencher in $CaCO_3$ crystal structure (Grover and Read, 1983; Machel, 1985; McManus and Wallace, 1992). In geologic environments, high Mn/Fe ratios correspond to oxygen-rich meteoric pore fluids (1-3 km depths) that generates the non-biogenic bright red-orange calcite luminescence typically of spectral 588 nm; the oxygen-deprived pore fluids at the deeper levels tend to generate dull red-brown calcite luminescence typically of spectral 679 nm (Machel et al. 1999; Machel, 2000; Budd et al. 2000; Cazenave et al. 2003; Verhaert et al., 2004; Lisitsyn et al. 2012). The Mn/Fe ratio and CL colors of calcite veins, therefore, could be used as proxies for the REDOX state and relative depth of pore fluids involved in the formation of calcite veins. Based on these findings, the following luminescence observations from calcite veins in our samples pose questions regarding the provenance of fluid sources involved: 1. Mutual crosscutting of veins with different luminescence contrast (e.g., Figs. 4c-d). 2. Luminescence zoning within a single blocky vein generation (e.g., Figs. 5b-c). And 3. Non-uniform/patchy luminescence veins (e.g., Figs, 6a-b). We suggest that these luminescence interrelationships represent fluid-source mixing during fluid overpressure events. In such cases, the fluid mixing simultaneously involves hypogene as well as down-circulating supergene fluid sources in varying proportions. The involvement of hypogene fluids is also supported by the observations that the growth and deformation of the blocky calcite veins in the SAF damage zone is contemporaneous with growths of secondary pyrite, anhydrite, and quartz (Fig. 2d, Fig. 3).

The microstructural correlation of blocky calcite veins with hydrothermal mineral phases, exemplified in Fig. 3, is useful for estimating a P-T bracket for the fluid overpressure events. EBSD study of a large secondary pyrite mass in sample G24 (black gouge) showed that the pyrite has been deformed via mechanisms ranging from cataclasis to SGR (sub-grain rotation) respectively corresponding to temperatures of 120°C (SAFOD depth) to ~400°C (Hadizadeh and Boyle 2018). This P-T range together with blocky calcite trace-element ratios indicate that the fluid overpressure events had occurred episodically as the SAF gouge was uplifted and exhumed to the current SAFOD depth. The blocky, and syntaxial calcite veins also show a range of e-twin types (Fig. 5a-b and Fig. 6 a-b) that indicate deformation at a range of temperatures up to ~250°C (Ferrill et al. 2004). A study by Lacombe et al. (2021) showed that unlike calcite e-twin piezometry (Rybacki et al. 2011), which might be highly variable depending on local stress field, calcite e-twin thermometry estimates are comparatively reliable.

Fluidized gouge injection microstructures were previously reported in samples bordering the SDZ (Mittempergher et al. 2011). The gouge injections in this study (Figs. 2h, Fig. 6d, and Fig.7) provide evidence of fluid overpressure events in the CDZ sample as well as within the CDZ-side damage zone of the fault. Rowe et al. (2012) argued that the width-to-length ratio of an injection is a direct measure of the shear strain required to accommodate the injection. The CDZ injections show width to length ratio value of 0.25 for the largest injection, and mean value of 0.39 for all reliably measured injections (Table 1). Rowe et al. (2012) attributed such proportionally large aspect ratios to coseismic fluid overpressure events. The oldest (GEN 1) and the youngest (GEN 3) calcites related to the CDZ injection microstructures are in a relative-time order based on both crosscutting relationship and luminescence contrast. However, as mentioned in section 3.3, GEN 1 calcite may predate the injection event. The CL image in Fig. 8b shows that the injection of fluidized gouge and growth of GEN 3 calcites occurred after extension fracture along the GEN 1 calcite vein. Similarly, quartz-calcite veins parallel to and related to the GEN 3 injection structure crosscut GEN 1 calcite (Fig. 9b-c). Therefore, CL colors of the calcite in this case could be reliably used to relate changes in calcite Mn/Fe ratio with changes in P-T conditions.

4.3 Changes in Mn/Fe and Mg/Ca ratios in calcite veins across the fault

Assuming increased Mn/Fe ratio in calcite veins is a proxy for uplift, exhumation, and increased meteoric water activity (see 4.2), the notable southwesterly drop in Mn/Fe ratio (Fig. 10a) indicates that the creeping intervals act as cross-fault permeability barriers. This conclusion is consistent with laboratory measurements of permeability and electrical resistivity in the SAFOD samples by Morrow et al. (2014 and 2015). Morrow et al. (2014) showed that the permeability of foliated SAFOD gouge range from ~10^{-20} m^2 to 10^{-19} m^2 in the damage zone and is ~10^{-21} m^2 in the fault core intervals. Our results also suggest that the incursion of shallow meteoric water into the SAF, at least close to the SAFOD site, is asymmetric and is mostly confined to the NE side of the fault zone. A similar conclusion regarding the permeability of the active creeping intervals of the SAF was reached by clumped-isotope thermometry of the calcite veins in the SDZ and CDZ samples, carried out by Luetkemeyer et al. (2016). The latter study showed that the $\delta^{18}O$ values of paleofluids, detected in the calcite veins, approach equilibrium with modern pore waters only farther away from the CDZ and SDZ. This finding is particularly consistent with our results for the CDZ side of the fault as well as with results of a study by Schleicher et al. (2010).

A comparison of the mean Mn/Fe and Mg/Ca ratios in individual gouge-injection calcite vein generations in the CDZ (open circle symbols, Fig. 10) with those of the blocky calcites elsewhere in the samples provide some insight into the relative age and source of the fluids involved. While the GEN 2 mean values in the CDZ interval tend to agree with the overall trend represented by the dotted line curve in Fig. 10a-b, the ratios for GEN 1 and GEN 3 calcites plot below and above the trend within the CDZ sample. In particular, we interpret the progressive increase in Mn/Fe ratio of the injection calcites, from 0.578 to 3.196 (Table 2b), as intermittent seismic events over a period of uplift and exhumation with GEN 3 calcites representing the latest coseismic event. The EBSD analysis (Fig. 9b-e) shows that the oldest (GEN 1) calcite grains adjacent to the gouge injection microstructure (Fig. 8) preserve high intracrystalline distributed lattice distortions up to 25° (see GROD values in Fig. 9c) and well-developed e-twins (Figs. 9b-c) consistent with significant intracrystalline strain. Conversely, the GEN3 calcite grains in the injection microstructure have low GROD values and typically contain no e-twins, consistent with having experienced little or no strain after formation of the injection structure. The GEN3 injection structures are associated with quartz veining. One such vein cuts and displaces the GEN3 calcite vein (see dotted area in Fig. 9b-c). The larger quartz grains (pale blue in Fig. 9b) show dark blue colours in the GROD map (Fig. 9c) consistent with having experienced limited or no post vein formation strain, as with the associated GEN3 calcite in the main injection structure. The inset scatterplot in Fig. 10b shows a negative correlation between Mg/Ca and Mn/Fe ratios in the studied vein calcites. This relationship is clearly not applicable to GEN 3 injection calcites. The discrepancy could be resolved to a significant degree if the injection pore fluid had originated outside the CDZ interval. Given the compositional similarity of GEN 3 calcites with the calcites in the bordering damage zone (Fig. 10a), we suggest that the latest gouge fluidization event in the CDZ was triggered by a coseismic incursion of meteoric water from the damage zone on the NE side of the CDZ. On the other hand, the fluid source for GEN 1 and GEN2 calcites appear to be internal to the low-permeability CDZ interval. It must be noted again that for lack of available core material we cannot assess the extent of meteoric water activity in the ~95m measured depth distance that separates CDZ and SDZ.

The SDZ and most of the damage zone calcite veins in the studied samples have a Mean Mg/Ca ratio of 0.0055 (SD 0.0022), which is close to those reported by Bradbury et al. (2015). The CDZ-side damage zone Mg/Ca mean values fall further to 0.003 (SD .0008) for the samples >2m away NE of the CDZ. In notable contrast, the Mean Mg/Ca ratio in the CDZ interval, while varying widely, is about an order of magnitude greater than Mean Mg/Ca ratio of the fault zone (Fig. 10b). The magnesian composition of calcite veins in the CDZ could be attributed to this interval's higher rate of serpentinite alteration due higher creep rate, which was initially discovered as borehole casing deformation (Zoback 2011) and later studied by Moore (2014). The low Mg/Ca values elsewhere across the fault indicate lack of dissolved-Mg transfer due to permeability barrier nature of the creeping intervals. We take this to imply change in pore fluid chemistry during exhumation to SAFOD depths in a manner consistent with the model proposed by Luetkemeyer et al. (2016-Fig. 6). The latter model does not preclude preservation and activity of trapped Fe-rich pore fluid enclaves in the low-permeability barrier zones and is consistent with the notable differences in calcite-vein trace element proportions across the SAF damage zone (Fig. 11). Another possible explanation for low Mg/Ca values in the SDZ is that the studied calcite veins shown in Fig. 6a-b formed within the less altered serpentinite blocks, where the vein fluids crystallized under a restricted dissolved-Mg transfer environment. Thus, it is probable that the SDZ mean Mg/Ca could be higher than the surrounding damage zone if data from calcite veins in the altered rind of the serpentinite block (if found) were included.

4.4 Implications for the seismicity of the creeping section

The potential for seismicity as well as occasional hazardous earthquake events (M>6) along known creeping fault zones, some slipping on low friction gouge, is not rare (Harris 2017). Several models have been proposed for processes that could lead to seismic instability in an otherwise aseismic regime. Veveakis et al. (2010) and Alevizos et al. (2014) hypothesized that serpentinite dehydration reactions in mature creeping fault zones might trigger a critical bifurcating process whereby thermal fluid pressurization could result in preservation of a steady state and/or an earthquake event. Other models based on geophysical data analysis, experimental work, and historic earthquake records suggest that intermittent slip-rate acceleration could occur within sections or the entire length of a creeping fault segment due to seismic ruptures in adjacent locked sections (Noda and Lapusta 2013; Jolivet et al. 2014; French et al. 2014, 2015). The aseismic creep rates in central California, measured along strike at the surface and geophysically ascertained to depths of ~30km, range from 22-35mm/year (Titus et al. 2006; Toke et al. 2011; Maurer and Johnson 2014; Jolivet et al 2014). Considering this range of slip-rates, Maurer and Johnson (2014) estimated the degree of frictional locking and its corresponding moment accumulation rate for long-term slip rates of 27-34mm/year. Their results suggest that locked patches may develop at between 10-20km depths and potentially rupture with M_w 6.5 with return time of 150 years. However, a significant factor regarding accelerating slip rates in aseismically deforming mature fault zones is the velocity strengthening nature of phyllosilicate-rich gouges. Noda and Lapusta (2013) suggested that the rate-strengthening frictional property of the clay gouge in the SAF core could be overcome by shear heating and thermal fluid pressurization if the creeping fault is loaded by a large distant seismic event. They maintained that aseismically creeping patches surrounded by low permeability rocks are more susceptible to reduced frictional resistance, as demonstrated in Taiwan 1999 Chi-Chi earthquake (Tanikawa and Shimamoto 2009).

The described models are partially consistent with our findings as they account for the possible coseismic fluid overpressure microstructures in the SDZ and CDZ while considering these intervals as permeability barriers. Furthermore, the presence of blocky calcite growths, and fluidized gouge injections in the CDZ and SDZ indicate that the coseismic events were not limited to the SAF damage zone. If the Creeping intervals are permeability barriers as our results indicate, changes in slip rate could involve hypogene fluid influx from below as well as occasional SAFOD depth-level fluid influx due to far away rupture propagations. Experimental work of French et al. (2014) on CDZ gouge samples at sub-seismic slip-rates showed evidence of dynamic weakening by shear-heating pressurization of pore fluid in the wet gouge and possible dehydration in the dry gouge. The study concluded that rupture propagation from a microseismic patch within the CDZ is unlikely, but sustained propagation from a large earthquake may be possible. In a biomarker thermal maturity analysis, Coffey et al. (2022) found that the intensely sheared intervals of the SAFOD black gouge (3192-3196 m MD) bordering the SW side of the SDZ, yield Mean maximum coseismic temperature of 840°C and minimum K/Ar age of ~3.2 Ma. The K/Ar ages also showed that black gouge is the youngest (9.5-3.3 Ma) while the CDZ-side gouges are considerably older (43-33.8 Ma). The latter age determination is consistent with the presence of blocky calcite veins (Fig. 6c) in our CDZ sample that predate the more recent alteration of the serpentinite block from which the sample is collected. This finding widens the age span for the development of blocky calcite vein textures (mesh and jigsaw patterns) in the CDZ interval. Regardless of the absolute and/or relative age of the coseismic fluid overpressure vein-forming events in our study, their widespread presence shows that the creeping SAF has intermittently hosted seismic events. Although Coffey et al. (2022) did not identify seismic events within the SDZ, the multiple coseismic slips in black gouge associated with very localized frictional heat could indicate thermal fluid pressurization proximal to the SDZ where we find a meshwork of blocky calcite veins seal the sheared serpentinite clasts (Fig. 6a-b). Furthermore, the presence of significant secondary pyrite in our black gouge sample points to the involvement of hypogene fluids. It is important to note that, as shown here, the events involving hypogene fluid pressurization in permeability barriers are going to be episodic with irregular return times. This could in turn expose aseismically creeping fault segments to significant earthquakes with indeterminate return times. Further studies may be necessary to investigate whether the entrained serpentinite-rich bodies in the SAF creeping segment have been locked intermittently over longer geological time.

5. Conclusions

Our results indicate that the damage zone and the actively creeping intervals of the SAF at SAFOD have been subject to intermittent coseismic fluid overpressure events. The recurring events are clearly indicated by multiple generations of blocky calcite growth, implosion microbreccias, and fluidized gouge injections. The CL of the calcite veins indicate the activity of both hypogene and supergene fluid sources with older veins tending to be hypogene-sourced and the youngest supergene-related. Analysis of trace-element composition of the vein calcites and their deformation alongside associated hydrothermal mineral phases show progressive uplift and exhumation followed by an asymmetric incursion of meteoric (supergene) water into the SAF damage zone. The same analysis also suggests that the actively creeping intervals have acted, at least lately, as permeability barriers. The differing creep rates in the two actively creeping intervals, SDZ and CDZ, is reflected in different intake of Mg in the calcite veins in the intervals. Our results are in overall agreement with recent studies of the SAF in central California that indicate large seismic events have occurred intermittently with aseismic creep in recent geological time or suggest future potential for such events.

Acknowledgments

We thank Diane Moore of the US Geological Survey and an anonymous reviewer for valuable constructive reviews of the manuscript. We would like to acknowledge assistance by Elliot Holmes in generating the whole sections optical images, Forrest Stevens, and Donald J. Biddle with generating 3D point cloud sample billet images. This research was partially supported by the U.S. National Science Foundation grant NSF-EAR-1800933 to J. Hadizadeh and A. E. Gaughan.

REFERENCE

Alevizos, S., Poulet, T., Veveakis, E., 2014. Thermo-poro-mechanics of chemically active creeping faults. 1: Theory and steady state considerations. J. Geophys. Res. 119(6), 4558-4582.

Bos, B. and Spiers, C. J., 2002. Frictional-viscous flow of phyllosilicate-bearing fault rock: Microphysical model and implications for crustal strength profiles. J. Geophys. Res. 107 (B2), ECV-1.

Bos, B., and Spiers, C. J., 2001. Experimental investigation into the microstructural and mechanical evolution of phyllosilicate-bearing fault rock under conditions favoring pressure solution. J. Struct. Geol. 23, 1187-1202.

Boullier, A-M., Yeh, E-C., Boutareaud, S., Song, S-R., Tsai, C-H., 2009. Microscale anatomy of the 1999 Chi-Chi earthquake fault Zone. Geochem. Geophys. Geosystem10 (3), 1525-2027.

Boullier, A-M., Fujimotob, K., Ohtanib, T., Roman-Rossa, G., Lewinc, E., Itob, H., Pezardd, P., Ildefonse, B., 2004. Textural evidence for recent co-seismic circulation of fluids in the Nojima fault zone, Awaji island, Japan. Tectonophys. 378, 161-181.

Boutareaud, S., Calugaru, D-G., Han, R., Fabbri, O., Mizoguchi, K., Tsutsumi, A., Shimamoto, T., 2008. Clay-clast aggregates: A new textural evidence for seismic fault sliding? Geophys. Res. Lett. 35, L05302.

Bradbury, K.K., Davis, C.R., Shervais, J.W., Janecke, S.U., Evans, J.P., 2015. Composition, alteration, and texture of fault-related rocks from SAFOD core and surface outcrop analogs: evidence for deformation processes and fluid-rock interactions. PAGEOPH 172, 1053–1078.

Braithwaite, C. J, 2016. Cathodoluminescence in Quaternary carbonate deposits. Sedimentary Geology 337, 29-35.

Budd, D. A., Hames, U., Ward, B., 2000. Cathodoluminescence in calcite cements: New insights on Nb and Zn Sensitizing, Mn activation, and Fe quenching at low trace-element concentrations. J. Sedimentary Res. 70 (1), 217-226.

Carpenter, B. M., Saffer, D. M., Marone, C., 2015. Frictional properties of the active San Andreas Fault at SAFOD: Implications for fault strength and slip behavior. J. Geophys. Res. 120, 5273–5289.

Carpenter, B.M., Saffer, D. M., Marone, C., 2012. Frictional properties and sliding stability of the San Andreas fault from deep drill core. Geology 40, 759-762.

Carpenter, B.M., Marone, C., Saffer, D.M., 2011. Weakness of the San Andreas Fault revealed by samples from the active fault zone. Nature Geoscience 4(4), 251–254.

Carpenter, B.M., Marone, C., Saffer, D.M., 2009. Frictional behavior of materials in the 3D SAFOD volume. Geophys. Res. Lett. 36, L05302.

Cazenave, S., Chapoulie, R., and Villeneuve, G., 2003. Cathodoluminescence of synthetic and natural calcite: the effects of manganese and iron on orange emission. Min. Petrol. 78, 243-253.

Chester, F. M., Friedman, M., Logan, J. M., 1985. Foliated cataclasites. Tectonophys. 111, 139-146.

Coble, C. G., French, M. E., Chester, F. M., Chester, J. S., Kitajima H., 2014. In situ frictional properties of San Andreas Fault gouge at SAFOD. Geophys. International J. 199 (2), 956-967.

Coffey, G.L., Savage, H. M., Polissar, P. J., Cox, S. E., Hemming, S. R., Winckler, G., Bradbury, K. K., 2022. History of earthquakes along the creeping section of the San Andreas fault, California, USA. Geology 50, 516–521.

Cowan, D. S., 1999. Do faults preserve a record of seismic slip? A field geologist's opinion. J. Struct. Geol. 21, 995-1001.

Ferrill, D. A., Morris, A. P., Evans, M. A., Burkhardd, M., Groshong Jr., R. H., Onasch, C. M., 2004. Calcite twin morphology: a low-temperature deformation geothermometer. J. Struct. Geol. 26, 1521-1529.

French, M. E., Chester, F. M., Chester, J. S., 2015. Micromechanisms of creep in clay-rich gouge from the central deforming zone of the San Andreas Fault. J. Geophys. Res. 120, 827–849.

French, M. E., Kitajima, H., Chester, J. S., Chester, F. M., Hirose, T., 2014. Displacement and dynamic weakening processes in smectite-rich gouge from the Central Deforming Zone of the San Andreas Fault. J. Geophys. Res. 119, 1777–1802.

Gratier, J.P., Richard, J., Renard, F., Mittempergher, S., Doan, L. M., Di Toro, G., Hadizadeh, J., Boullier, A. M., 2011. Aseismic sliding of active faults by pressure solution creep: evidence from the San Andreas Fault Observatory at Depth. Geology 39, 1131–1134.

Gratier, J.-P., Favreau, P., Renard, F., 2003. Modeling fluid transfer along Californian faults when integrating pressure solution crack sealing and compaction process: J. Geophys. Res.108 (B2).

Gratier, J-P., Renard, F., Labaume, P., 1999. How pressure solution creep and fracturing processes interact in the upper crust to make it behave in both a brittle and viscous manner. J. Struct. Geol. 21 (8-9), 1189-1197.

Grover, Jr., G. and Read, J. E., 1983. Paleoaquifer and deep burial related cements defined by regional cathodoluminescent patterns, Middle Ordovician carbonates, Virginia. AAPG Bull. 67 (8), 1275-1303.

Gu, D., Han, R., Woo, S., 2021. Geological records of coseismic shear localization along the Yangsan fault, Korea. J. Geophys. Res. 126, e2020JB021393.

Hadizadeh, J. and Boyle, A. P., 2018. A study of secondary pyrite deformation and calcite veins in SAFOD damage zone with implications for aseismic creep deformation mechanism at depths>3 km. J. Struct. Geol. 117, 14-26.

Hadizadeh, J., Tullis, T. E., White, J. C., Konkachbaev, A., 2015. Shear localization, velocity weakening behavior, and development of cataclastic foliation in experimental granite gouge. J. Struct. Geol. 71, 86-99.

Hadizadeh, J., Carpenter, B. M., Mitchell, T. M., Di Toro, G., 2013. Microstructures of reconstituted SAFOD gouge deformed in room temperature friction experiments at 14 μm/s to 6 m/s sliding velocities. AGU. Fall meeting Abstracts (vol.2013, pp T33C-2652).

Hadizadeh, J., Mittempergher, S., Gratier, J. P., Renard, F., Di Toro, G., Richard, J., Babaie, H.A., 2012. A microstructural study of fault rocks from the SAFOD: Implications for the deformation mechanisms and strength of the creeping segment of the San Andreas Fault. J. Struct. Geol. 42, 246–260.

Harris, R. A., 2017. Large earthquakes and creeping faults. Rev. Geophys. 55,169-198.

Hickman, S., Zoback, M., Ellsworth, W., 2004. Introduction to special section: Preparing for the San Andreas Fault Observatory at Depth. Geophys. Res. Lett. 31, L12S01.

Holdsworth, R.E., van Diggelen, E. W. E., de Bresser, J.H.P., Walker, R. J., Bowen, L., 2011. Fault rocks from the SAFOD core samples: implications for weakening at shallow depths along the San Andreas Fault, California. J. Struct. Geol. 33, 132–144.

Holmes, E.M., Gaughan, A.E., Biddle, D.J., Stevens, F.R., Hadizadeh, J., 2021. Geospatial Management and Analysis of Microstructural Data from San Andreas Fault Observatory at Depth (SAFOD) Core Samples. ISPRS Int. J. Geo-Inf. 10, 332.

Janssen, C., Naumann, R., Morales, L., Wirth, R., Rhede, D., Dresen, G., 2015. Co-seismic and/or a-seismic microstructures of JFAST 343 core samples from the Japan Trench. Marine Geology 362, 33-42.

Janssen, C., Wirth, R., Wenk, H.-R., Morales, L., Naumann, R., Kienast, M., Song, S.-R., Dresen, G., 2014. Faulting processes in active faults e Evidences from TCDP and SAFOD drill core samples. J. Struct. Geol. 65, 100-116.

Janssen, C., Kanitpanyacharoen, W., Wenk, H.-R., Wirth, R., Morales, L., Rybacki, E., Kienast, M., Dresen, G., 2012. Clay fabrics in SAFOD core samples. J. Struct. Geol. 43, 118-127.

Janssen, C., Wirth, R., Reinicke, A., Rybacki, E., Naumann, R., Wenk, H.-R., Dresen, G., 2011. Nanoscale porosity in SAFOD core samples (San Andreas Fault). Earth Plan. Sci. Lett. 301, 179-189.

Janssen, C., Wirth, R., Rybacki, E., Naumann, R., Kemnitz, H., Wenk, H.-R., Dresen, G., 2010.

Amorphous material in SAFOD core samples (San Andreas Fault): Evidence for crush origin psuedotachylytes? Geophys. Res. Lett. 37, L01303.

Jeppson, T. N., Bradbury, K. K., Evan, J. P., 2010. Geophysical properties within the San Andreas Fault Zone at the San Andreas Fault Observatory at Depth and their relationships to rock properties and fault zone structure. J. Geophys. Res. 115, B12423.

Jolivet, R., Simons, M., Agram, P. S., Duputel, Z., Shen, Z. K., 2015. Aseismic slip and seismogenic coupling along the central San Andreas Fault. Geophys. Res. Lett. 42, 297–306.

Lacombe, O., Parlangeau, C., Beaudoin, N. E., Amrouch, K., 2021.Calcite Twin Formation, Measurement and Use as Stress–Strain Indicators: A Review of Progress over the Last Decade. Geosciences 11, 445.

Lin, A., 2011. Seismic slip recorded by fluidized ultracataclastic veins formed in a coseismic shear zone during the 2008 Mw 7.9 Wenchuan earthquake. Geology 39 (6), 547–550.

Lisitsyn, V. M., Polisadova, E. F., Valiev, D. T., 2012. Pulsed Cathodoluminescence of Calcite Crystals of Various Origins. Inorganic Materials 48 (7), 738–744.

Lockner, D.A., Morrow, C., Moore, D., Hickman, S., 2011. Low strength of deep San Andreas Fault gouge from SAFOD core. Nature 472, 82–85.

Luetkemeyer, B., Kirschner, D. L., Huntington, K. W., Chester, J. S., Chester, F. M., Evans, J. P., 2016. Constraints on paleofluid sources using the clumped-isotope thermometry of carbonate veins from the SAFOD (San Andreas Fault Observatory at Depth) borehole. Tectonophysics 690, 174-189.

Machel, H.G., Application of Cathodoluminescence to carbonate diagenesis. In: Pagel M., Barbin V., Blanc P., Ohnenstetter D. (Eds.), Cathodoluminescence in Geosciences. Springer-Verlag, Berlin, pp. 271–301. 2000.

Machel, H.G., Mason, R. A., Mariano, A. N., Mucci, A., Causes and emission of luminescence in calcite and dolomite. In: Luminescence Microscopy: Qualitative and Quantitative Aspects. Charles E. Barker and Otto C. Kopp eds. 1999.

Machel, H.G., 1985. Cathodoluminescence in calcite and dolomite and its chemical interpretation. Geoscience Canada 12, 139–147.

McManus, A., Wallace, M.W., 1992. Age of Mississippi valley-type sulfides determined using Cathodoluminescence cement stratigraphy, Lennard shelf, canning basin, Western Australia. Econ. Geol. 87, 189–193.

Maurer, J., and Johnson, K., 2014. Fault coupling and potential for earthquakes on the creeping section of the central San Andreas Fault. J. Geophys. Res. 119, 4414–4428.

Mittempergher, S., Di Toro, G. D., Gratier, J-P., Hadizadeh, J., Smith, S., 2011. Evidence of transient increases of fluid pressure in SAFOD Phase III Cores. Geophys. Res. Lett. 38, L03301.

Moore, D. E., Lockner, D. A., Hickman, S., 2016. Hydrothermal frictional strengths of rock and mineral samples relevant to the creeping section of the San Andreas Fault. J. Struct. Geol. 89, 153-167.

Moore, D. E., 2014. Comparative mineral chemistry and textures of SAFOD fault gouge and damage-zone rocks. J. Struct. Geol. 68, 82-96.

Moore, D.E., Rymer, M.J., 2012. Correlation of clayey gouge in a surface exposure of serpentinite in the San Andreas Fault with gouge from the San Andreas Fault Observatory at Depth (SAFOD). J. Struct. Geol. 38, 51–60.

Morrow, C., Lockner, D. A., Hickman, S., 2015. Low resistivity and permeability in actively deforming shear zones on the San Andreas Fault at SAFOD. J. Geophys. Res. 120, 8240–8258.

Morrow, C. A., Lockner, D. A., Moore, D.E., Hickman, S., 2014. Deep permeability of the San Andreas Fault from San Andreas Fault Observatory at Depth (SAFOD) core samples. J. Struct. Geol. 64, 99-114.

Noda, H. and Lapusta, N., 2013. Stable creeping fault segments can become destructive as a result of dynamic weakening. Nature 493, 519-521.

Otsuki, K., Uduki, T., Monzawa, N., and Tanaka, H., 2005. Clayey injection veins and pseudotachylyte from two boreholes penetrating the Chelungpu fault, Taiwan: Their implications for the contrastive seismic slip behaviors during the 1999 Chi-Chi earthquake. Island Arc 14(1), 22–36.

Richard, J., Gratier, J-P., Doan, M-L., Boullier, A-M., Renard, F., 2014. Rock and mineral transformations in a fault zone leading to permanent creep: Interactions between brittle and viscous mechanisms in the San Andreas Fault. J. Geophys. Res. 119, 8132–8153.

Rowe, C. D., Kirkpatrick, J. D., Brodsky, E. E., 2012. Fault rock injections record paleo-earthquakes. Earth Plan. Sci. Lett. 335, 154-166.

Rowe, C.D., Moore, J.C., Meneghini, F., McKiernan, A.W., 2005. Large-scalepseudotachylytes and fluidized cataclasites from an ancient subduction thrust fault. Geology 33 (12), 937-940.

Rutter, E. H. and Mainprice, D. H., 1979. On the possibility of slow fault slip controlled by a diffusive mass transfer. Gerlands Beitr. Geophys. 88(2), 154–162.

Rybacki, E., Janssen, C., Wirth, R., Chen K., Wenk, H.-R., Stromeyer, D., Dresen, G., 2011. Low-temperature deformation in calcite veins of SAFOD core samples (San Andreas Fault)- Microstructural analysis and implications for fault rheology. Tectonophysics 509, 107-119.

Schleicher, A.M., van der Pluijm, B.A., Warr, L.N., 2010. Nanocoatings of clay and creep of the San Andreas fault at Parkfield, California. Geology 38, 667–670.

Schleicher, A. M., Tourscher, S. N., van der Pluijm, B. A., and Warr, L. N., 2009. Constraints on mineralization, fluid-rock interaction, and mass transfer during faulting at 2-3 km depth from the SAFOD drill hole. J. Geophys. Res. 114 (B4).

Scuderi, M. M., Collettini, C., Marone, C., 2017. Frictional stability and earthquake triggering during fluid pressure stimulation of an experimental fault. Earth Plan. Sci. Lett. 477, 84-96.

Sheppard, R.E., Polissar, P.J., and Savage, H.M., 2015. Organic thermal maturity as a proxy for frictional fault heating: Experimental constraints on methylphenanthrene kinetics at earthquake timescales: Geochim. et Cosmochim. Acta 151, 103–116.

Sibson, R.H., 1986. Earthquakes and rock deformation in crustal fault zones. Annual Rev. Earth Plan. Sci. 14, 149–175.

Smeraglia, L., Billi, A., Carminati, E., Cavallo, C., Doglioni, C., 2017. Field- to nano-scale evidence for weakening mechanisms along the fault of the 2016 Amatrice and Norcia earthquakes, Italy. Tectonophysics 712, 156-169.

Smith, S.A. F., Collettini, C., Holdsworth, R. E., 2008. Recognizing the seismic cycle along ancient faults: CO2-induced fluidization of breccias in the footwall of a sealing low-angle normal fault. J. Struct. Geol. 30, 1034-1046.

Spruženiece, L., Späth, M., Urai, J. L., Ukar, E., Selzer, L., Nestler, B., 2021. Wide-blocky veins explained by dependency of crystal growth rate on fracture surface type: Insights from phase-field modeling. Geology 49 (6), 641-646.

Stunitz, H., Keulen, N., Hirose, T., Heilbronner, R. E., 2010. Grain size distribution and microstructures of experimentally sheared granitoid gouge at coseismic slip rates- Criteria to distinguish seismic and aseismic faults? J. Struct. Geol. 32, 59-69.

Suchy, V., Heijlenb, W., Sykorovac, I., Muchezb, Ph., Dobesd, P., Hladikovad, J., Jackovad, I., Safandae, J., Zemana, A., 2000. Geochemical study of calcite veins in the Silurian and Devonian of the Barrandian Basin (Czech Republic): evidence for widespread post-Variscan fluid flow in the central part of the Bohemian Massif. Sed. Geol. 131, 201-219.

Tanikawa, W., and Shimamoto, T., 2009. Frictional and transport properties of the Chelungpu fault from shallow borehole data and their correlation with seismic behavior during the 1999 Chi-Chi earthquake. J. Geophys. Res. 114, B01402.

Titus, S. J., DeMets, C., and Tikoff, B., 2006. Thirty-Five-Year Creep Rates for the Creeping Segment of the San Andreas Fault and the Effects of the 2004 Parkfield Earthquake: Constraints from Alignment Arrays, Continuous Global Positioning System, and Creep meters. Bull. Seism. Soc. Amer. 96 (4B), 250-268.

Toké, N.A., Arrowsmith, J R., Rymer, M.J., Landgraf, A., Haddad, D.E., Busch, M., Coyan, J., Hannah, A., 2011. Late Holocene slip rate of the San Andreas fault and its accommodation by creep and moderate magnitude earthquakes at Parkfield, California. Geology 39 (3), 243-246.

Verhaert, G., Muchez, P., Sintubin, M., Similox-Tohon, D., Vandycke, S., Keppens, E., Hodge, E.J., Richards, D.A., 2004. Origin of palaeofluids in a normal fault setting in the Aegean region. Geofluids 4, 300–314.

Veveakis, E., Alevizos, S., Vardoulakis, I., 2010. Chemical reaction capping of thermal instabilities during shear of frictional faults. J. Mech. Phys. Solids 58, 1175-1194.

Zoback, M.D., Hickman, S.H., Ellsworth, W.E., 2011. Scientific drilling into the San Andreas Fault Zone — An Overview of SAFOD’s First Five Years. Scientific Drilling 11, 14-28.

Figure Captions

Fig. 1. Location of studied samples, shown by crossed circles, as distributed along the SAFOD phase 3 lateral borehole G. Measured Depth, core Run, and core Section for each sample billet is indicated atop two lithostructural bars representing two core segments of the SAFOD phase III drilling. Southwestern Deforming Zone and Central Deforming Zone, respectively labeled SDZ (~3196.5-3198.3 m MD) and CDZ (~3296.5-3299.1 m MD), are active creep intervals detected as deformation of borehole metal casing during drilling (Zoback et al. 2010). Black arrows indicate approximate position of minor faults reported by Holdsworth et al. (2011). An approximately 95m core hiatus separates the two segments of drillhole G. Core metering and lithostructural unit boundaries modified after Holdsworth et al. (2011), Janssen et al. (2014), and Bradbury et al. (2015).

Fig. 2. Typical deformation microstructures in siltstone-shale units of the SAF damage zone. Images are optical PPL unless otherwise stated. Trace of foliation identifiable at section-scale is indicated by dashed line labeled F.

a. Close-up view showing impingement dissolution of a reworked quartzo-feldspathic block in block-in-matrix gouge. Inset box relates the magnified area to a general view of the gouge microstructure. Sample G11, 3187.3m MD.

b. Typical foliation mainly defined by a pressure solution cleavage. An antitaxial calcite vein fabric at high angles to foliation is present in quartzofeldspathic clasts. Note that calcite veins are confined to within clast boundaries. Sample G23, 3193.3m MD.

c. BS-SEM image showing close-up view of ultracataclasite located within dark-colored streaks in the smaller inset box. Dashed line areas encircle fragments of calcite vein fabric relicts from earlier deformation by pressure solution. Cal is calcite, QFc is reworked quartzofeldspathic clast. Sample G24, 3193.7m MD (black gouge ~2.8m SW of SDZ).

d. Sheared mass of secondary pyrite stretched sub-parallel to trace of foliation. Note absence of deformation by pressure solution at contacts between pyrite mass and quartzofeldspathic gouge. Inset box is location of chemical map in Fig. 3b. Sample same as in c.

e. Pressure solution cleavage foliation NE of SDZ. Anastomosing relaxation cracks have opened along foliation. Note calcite fabric in siltstone clast on far-left side. Inset box is location of Fig. 4d. Sample G32, 3198.6m MD.

f. Calcite-sealed blocks of fractured banded siltstone ~1.6m SW of CDZ. White arrow points to impingement dissolution. Sample G41, 3295m MD.

g. Intensely deformed foliated block-in-matrix gouge including multiple generations of blocky calcite veins. Convoluted calcite veins reflect flowage of shale-rich ultracataclasite matrix between quartzofeldspathic cataclasite blocks. Inset SEM-SE image shows typical injection of matrix ultracataclasites into tensile microfractures in calcite veins in this sample. Sample G52, 3301.34m MD.

h. Shallow injection of coarse-grained cataclasites into a reworked block in block-in-matrix gouge (dotted trace). Arrows show pressure solution seams along bands of siltstone cataclasite. White streaks are thin blocky calcite veins. Sample G65, 3311.1m MD.

Fig. 3. Elemental maps interpreted as mineral composition showing typical microstructural association of blocky calcite veins with hydrothermal mineralization in damage zone samples. Dashed line labeled F is trace of foliation recognizable at section-scale.

a. Secondary pyrite and blocky vein-calcite sheared along a thin cataclasite band. The band is traced with white dashed line based on SEM image of mapped area. Sample G13, 3188.6m MD.

b. Secondary pyrite overprinting blocky calcite sheared along foliation (see inset box in Fig. 2d). Note euhedral forms in pyrite (inset SEM-SE image). The area within dashed line (cCal) is a clast with calcite vein fabric related to pressure solution cleavage. Sample G24, 3193.7m MD (~3m SW of SDZ).

c. A vein fragment comprised of prismatic anhydrite crystals (anh) and strongly twinned blocky calcite (cal). Sample G41, 3295m MD (~1.5m SW of CDZ).

d. Growth of pyrite and apatite inclusions in strongly deformed blocky calcite vein. Sample G52, 3301.34m MD.

Fig. 4. Paired CL-PPL images showing microstructures of blocky and syntaxial calcite veins in SDZ-side damage zone of the SAF. Where present at section scale, trace of foliation (F) is shown with a dashed line.

a. Cross-cutting blocky and syntaxial elongate calcite vein generations (thick arrow) in highly fractured, non-foliated siltstone. A thin arrow shows blocky veins sealing a micro-jog. Sample G13, 3188.60m MD.

b. Blocky calcite vein generations deformed by local dextral shear and overprinted by syntaxial crack-seal veins along extension cracks (brighter CL). Block-in-matrix foliated siltstone-shale cataclasite. Sample G22, 3192.51m MD.

C. Blocky calcite veins offset along a set of R-shear microfractures and overprinted by syntaxial crack-seal veins of variable CL. Area within rectangular box shows dark and light CL veins mutually overprint. Thick arrows point to possible pressure solution seams in calcite veins. Intensely foliated siltstone-shale cataclasite (black gouge). Sample G24, 3193.70m MD.

d. Calcite-vein fabric with anhydrite inclusion (Anh) at high angles to foliation in a large siltstone clast (see inset box in Fig. 2e for microstructural context). Thick, bent e-twins are present in the large blocky vein. Arrow points to an example of mutual crosscutting of calcite veins with dark and light luminescence. Sample G32, 3198.6m MD.

Fig. 5. Paired CL-PPL images showing microstructures of blocky and syntaxial calcite veins in CDZ-side damage zone of the SAF. Where present at section scale, trace of foliation (F) is shown with a dashed line.

a. Sample G41 ~1.5m SW of CDZ showing blocky veins with anhydrite inclusions (Anh). Mechanical twins with different lamellae thickness and spacing are present (inset boxes marked on CL and PPL images). The image is typical of 5 sections from two G41 core billets at 3295m and 3295.13m MD in banded siltstone.

b. An open-cavity blocky growth with distinct areas of light and dark luminescence zoning. Note network of thin crack-seal veins with brighter luminescence extending from margins into interior of the vein. Clear examples of crosshatched, tapering, and gently bent e-twin types are shown in inset boxes marked on PPL and CL images. Note tight lamellar spacing of the twins throughout. Foliated siltstone-shale. Sample G45, 3299.3m MD.

c. Showing blocky elongate type veins with mostly thin, tabular e-twins. Note patchy luminescence zoning. Foliated siltstone-shale. Sample G47, 3300.0m MD.

d. Strongly deformed blocky veins (see inset box in Fig. 2g) with a variety of e-twin lamellae structures. On CL image, cross-cutting relationship indicates at least 3 vein generations with latest generation having brighter luminescence. Note open cavities (arrows) in bright-color veins. Foliated siltstone-shale. Sample G52, 3301.34m MD.

e. Blocky veins (mainly on the right side) cut across antitaxial fibrous veins with pressure solution seams (arrows). Tabular and thick twin lamellae types are present in blocky calcite. Foliated siltstone-shale. Sample G56, 3305.4m MD.

f. Showing blocky veins seal a sheared jigsaw texture. Shear along an R' plane (dashed line) and implosion-driven extension (arrows) are consistent with stress field depicted on PPL image. Foliated siltstone-shale. Sample 65, 3311.1m MD.

Fig. 6. Paired CL-PPL images showing microstructures of blocky and syntaxial calcite veins in active creep zones CDZ and SDZ. Trace of foliation recognizable at section scale is shown with a dashed line labeled F.

a-b. CL images of blocky calcite veins seal implosion jigsaw textures in two different areas on the same thin section in SDZ sample. Inset close-up views on PPL images show presence of a variety of e-twin lamellae in blocky calcites including thin, tabulated thick, and thick with tapered bent and lensoid types. Note patchy calcite luminescence (white arrows). The gouge is mostly composed of altered and deformed serpentinite phases. Sample G27, 3196.70m MD.

c. A segment along length of a thick blocky vein in CDZ crosscut by a set of calcite-sealed extension veins with dull luminescence. The latter veins do not extend into surrounding serpentine-rich gouge matrix (Serp) but merge with mesh-like veins (M) on the right. Note string of open cavities along a bright-colored vein that seals a late extension crack (arrow on CL image). Sample G44, 3298.3m MD, collected from within serpentinite block.

d. Showing one of several fluidized gouge injections across quartzo-feldspathic bands (QFc) that run parallel to foliation in CDZ sample. Injection conduit is mostly sealed by blocky calcite growths, ~50µm in average grain size, with gouge fragment inclusions. Note calcite generation with dull luminescence (arrows on CL image). Injection flow lines in clay-rich gouge (CG) could be seen at opening end and along injection walls. Sample G44, 3298.3m MD.

Fig. 7. Fluidized gouge injection microstructures in CDZ sample (G44, 3298.3m MD). Trace of foliation is shown with dashed line F.

a. Gouge injection microstructure with aspect ratio of 0.25 (INJ G44A in Table 1) shows an injection from left to right at high-angles to foliation shown. Image is an optical XPL mosaic. Plain white and yellowish areas of the image are respectively voids filled with resin (labeled arrow). Brown and black areas within the injection conduit are extremely fine-grained Mg-rich clay gouge. QFc is foliation-parallel quartzofeldspathic bands of cataclasites. Serp is serpentinite-derived phyllosilicate phases.

b. BS-SEM mosaic image partially covering the injection area (inset box in a). Clay-rich gouge fills injection conduit lined with blocky calcite growth. Intruding gouge grades from coarse at the opening to extremely fine-grained at the tip of injection microstructure. Note chambered structure of the injection conduit involving cross-conduit calcite growth.

c. BS-SEM image (inset box in b) showing close-up view of extremely fine-grained conglobate clay gouge (CG) in mid-section of the injection. Injection-wall sequence along double-headed arrow consists of calcite-sealed quartzo-feldspathic microbreccia, and old foliation-parallel quartzo-feldspathic cataclasite band (QFC) at the bottom. A chrome-spinel porphyroblast (Cs), deformed by brittle fracture, is shown by black arrow. At the top side, calcite-sealed microbreccia includes large feldspar (Fl), and quartz (Q) clasts.

d. A small reworked injection microstructure across quartzofeldspathic cataclasite band. Areas in black are void spaces. Note foliation-parallel cluster of pyrite framboids (Py) crosscut by this injection microstructure.

Fig. 8. Composition map and CL image of fluidized gouge injection microstructure (G44A, INJ. A, in Table 1) in CDZ sample.

a. Interpreted elemental map showing microstructural relationship between blocky calcite growth and injected serpentinite-rich gouge.

b. CL image revealing spatial interaction of calcite from different generations involved in fluidized gouge injection. Three generations of calcite growth, labeled GEN 1-3, could be identified via a combination of luminescence contrast and crosscutting relationship. Injection wall (white border line) is lined with latest calcite generation, GEN 3, that crosscuts earliest generation, GEN 1, calcite. Isolated pixel color tiles of the 3 calcite generations are shown on the right. White dots on the image are 83 EDS data collection spots. Inset box is location of EBSD images shown in Figs. 9b-c.

Fig. 9. The trace-element concentration and EBSD analysis of blocky calcites involved in fluidized gouge injection microstructure shown in Fig. 8.

a. Ternary plot of Mean trace-element concentrations; individual plots on the right with GEN 3 being the latest calcite vein generation.

b. EBSD-derived phase map (red = calcite, cyan = quartz) of area within Fig. 8b inset box. Two apparently separate GEN 1 twinned calcite grains are highlighted in yellow. White dashed line in b and c separates GEN1 calcite veins from GEN3 calcite that lines injection structure. Dotted white line in b and c is a GEN3-parallel quartz vein that separates the two parts of GEN 1 calcite grain highlighted in yellow. Note the well-developed e-twins in GEN1 calcite grains (parallel black lines) and their absence from GEN3 calcite grains.

c. EBSD-derived grain reference orientation deviation (GROD) map of area in b (blue = 0°, red = 25°). Note that GEN1 calcite domains have high GROD values (up to 25° in the highlighted grain) indicating a high level of lattice distortion within the grains, whereas GEN3 calcite grains, across the dashed line, have low GROD values indicating little or no lattice distortion within the grains. Quartz grains in the quartz vein (dotted line) have low GROD values indicating little or no lattice distortion. Also note the well-developed e-twins in GEN1 calcite grains (parallel white lines) and their absence from GEN3 calcite grains.

d. Lower-hemisphere pole figures for the two highlighted GEN 1 calcite "grains" in image b. Note that the two grains have the same lattice orientations, consistent with being originally part of the same calcite grain.

e. Lower-hemisphere pole figures for grains in quartz vein that separates GEN1 calcite grain in b and c. Note that the twelve quartz grains identified as part of the vein in c have a restricted range of c-axis directions oblique to the vein trace, while m <10-10> and a <11-20> axes define a broad girdle. Colors are in the IPF space.

Fig. 10. Across-the-fault variations in composition of blocky, elongate blocky, and syntaxial calcite veins with mean sampling frequency of ~1.6 m, excluding the coring gap (data from Table 2a). Active creep intervals SDZ and CDZ are indicated by shaded vertical bars. Error bars

are Standard Error of sample population. Short vertical double lines on x-axis are approximate location of minor faults transferred from Fig. 1.

a. Changes in mean value of Mn/Fe ratio. Open-circle symbols with different sizes represent mean Mn/Fe ratio for gouge-injection calcite vein generations in CDZ interval (data from Table 2b). GEN 3 is the latest generation.

b. Changes in mean value of Mg/Ca ratio. The open circle symbols in CDZ interval represent mean Mg/Ca ratio for gouge-injection calcite vein generations (data from Table 2b). Inset scattergram showing a generally negative correlation between Mn/Fe and Mg/Ca ratio (Table 2 ratio columns, excluding G44inj. data).

Fig. 11. Ternary plots showing changes in trace element composition in blocky calcite veins with distance from the active-creep intervals SDZ and CDZ (excluding data from injection-related calcite veins).

Tables

Table 1. Aspect ratio data for gouge injection microstructures a, b, and c as they appeared on parallel petrographic thin sections A, B, and C through the CDZ core sample billet, cut parallel to each other, perpendicular to foliation.

Sample	INJ.	L, mm	W, mm	W/L
G44 A	a	5.651	1.352	0.25
G44 A	b	3.616	1.446	0.40
G44 A	c	2.486	1.243	0.50
G44 B	a	3.653	0.913	0.25
G44 B	b	4.762	3.524	0.74
G44 C	a	4.491	1.078	0.24
G44 C	b	3.685	1.179	0.32

Table 2. Mean atomic wt.% Mg, Fe, Mn, and Mg/Ca and Mn/Fe values (mean of the ratios) from spots on CL images of calcite veins in all samples. Values in second row for each sample is Standard Error. **a.** Mean values for N spots in typical calcite veins in each sample. **b.** Individual and combined mean values for N spots in calcite generations (GEN 1-3) related to sample G44 gouge injection microstructures (see INJ. a, sample G44A, Table 1). GEN 3 is the latest generation.

2a

Sample	Mg	Fe	Mn	Mg/Ca	Mn/Fe	N
G65	**0.053**	**0.081**	**0.352**	**0.003**	**4.837**	**53**
	0.005	0.005	0.011	0.000	0.185	
G61	**0.039**	**0.096**	**0.344**	**0.002**	**5.220**	**27**
	0.003	0.027	0.014	0.000	0.305	
G56	**0.051**	**0.087**	**0.410**	**0.003**	**5.536**	**34**
	0.003	0.010	0.022	0.000	0.394	
G52	**0.082**	**0.049**	**0.093**	**0.004**	**2.676**	**66**
	0.006	0.003	0.003	0.000	0.240	
G51B	**0.067**	**0.030**	**0.055**	**0.005**	**2.500**	**36**
	0.006	0.003	0.002	0.000	0.267	
G47	**0.127**	**0.070**	**0.088**	**0.007**	**1.700**	**19**
	0.016	0.008	0.005	0.001	0.257	
G46	**0.118**	**0.074**	**0.105**	**0.006**	**2.364**	**27**
	0.013	0.011	0.005	0.001	0.299	
G45	**0.098**	**0.047**	**0.079**	**0.006**	**2.961**	**37**
	0.009	0.005	0.003	0.001	0.431	
G44	**0.718**	**0.152**	**0.144**	**0.044**	**1.290**	**30**
	0.168	0.013	0.010	0.012	0.208	
G41	**0.164**	**0.046**	**0.150**	**0.008**	**3.398**	**29**
	0.014	0.003	0.006	0.001	0.122	
G32	**0.138**	**0.133**	**0.130**	**0.007**	**1.176**	**20**
	0.022	0.013	0.019	0.001	0.177	
G28	**0.138**	**0.044**	**0.021**	**0.007**	**0.646**	**44**
	0.022	0.005	0.001	0.001	0.056	
G27	**0.078**	**0.039**	**0.043**	**0.004**	**1.467**	**41**
	0.022	0.006	0.004	0.001	0.136	
G24	**0.064**	**0.062**	**0.079**	**0.005**	**1.568**	**35**
	0.008	0.006	0.005	0.001	0.156	
G22	**0.152**	**0.170**	**0.141**	**0.008**	**1.095**	**22**
	0.060	0.035	0.006	0.004	0.099	
G13	**0.134**	**0.121**	**0.184**	**0.007**	**1.622**	**24**
	0.012	0.008	0.010	0.001	0.103	

2b

Vein	Mg	Fe	Mn	Mg/Ca	Mn/Fe	N
GEN 1	**0.331**	**0.185**	**0.097**	**0.018**	**0.578**	**32**
	0.048	0.009	0.007	0.003	0.081	
GEN 2	**0.827**	**0.154**	**0.161**	**0.047**	**1.631**	**28**
	0.151	0.022	0.010	0.010	0.227	
GEN 3	**0.245**	**0.060**	**0.120**	**0.013**	**3.196**	**23**
	0.052	0.011	0.007	0.003	0.407	
combined	**0.475**	**0.140**	**0.125**	**0.026**	**1.659**	**83**
	0.062	0.010	0.006	0.004	0.180	

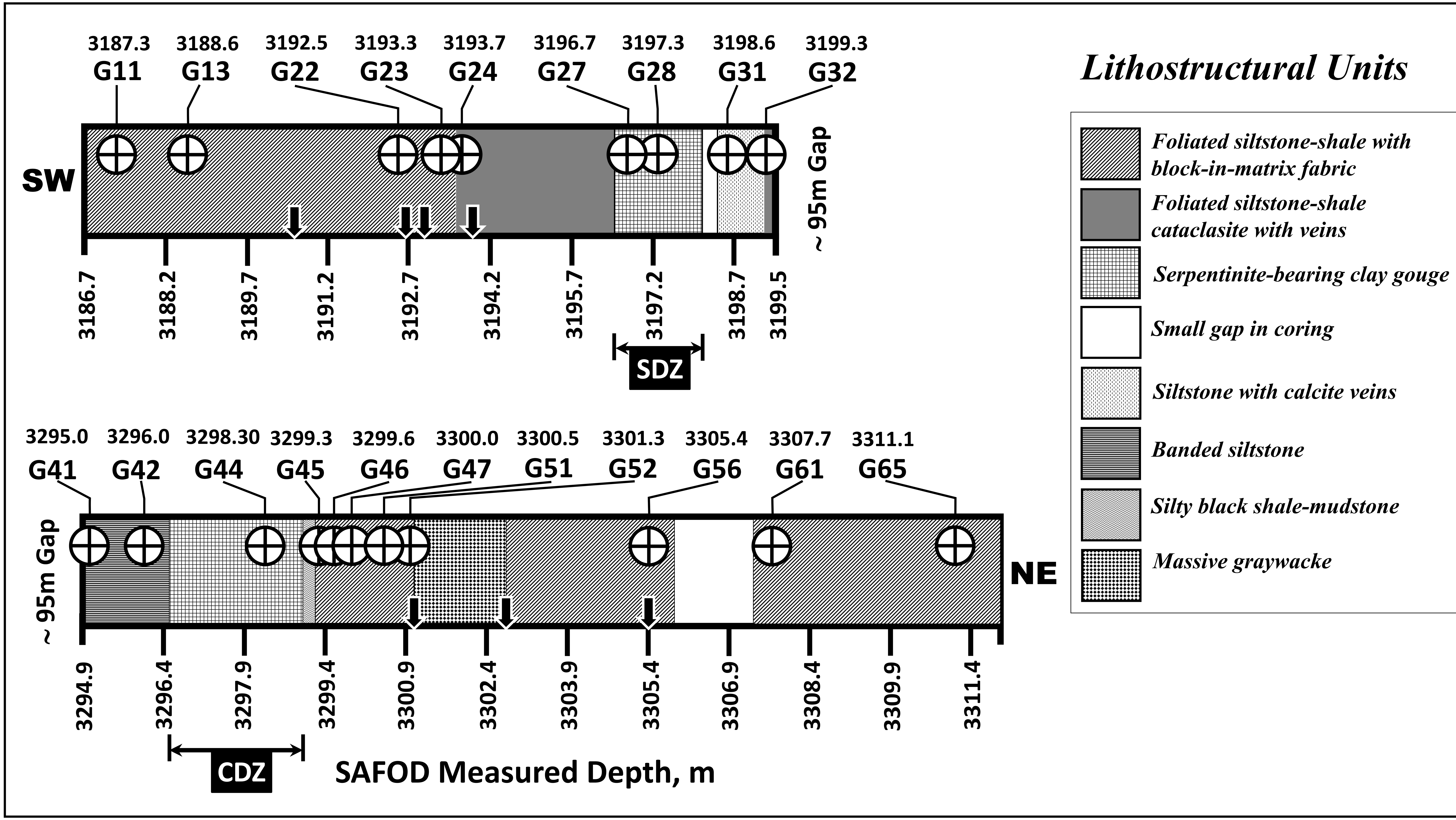

Fig. 1. Location of studied samples, shown by crossed circles, as distributed along the SAFOD phase 3 lateral borehole G. Measured Depth, core Run, and core Section for each sample billet is indicated atop two lithostructural bars representing two core segments of the SAFOD phase III drilling. Southwestern Deforming Zone and Central Deforming Zone, respectively labeled SDZ (~3196.44-3198.05 m MD) and CDZ (~3296.5-3299.1 m MD), are active creep intervals detected as deformation of borehole metal casing during drilling (Zoback et al. 2010). Black arrows indicate approximate position of minor faults reported by Holdsworth et al. (2011). An approximately 95m core hiatus separates the two segments of drillhole G. Core metering and lithostructural unit boundaries modified after Holdsworth et al. (2011), Janssen et al. (2014), and Bradbury et al. (2015).

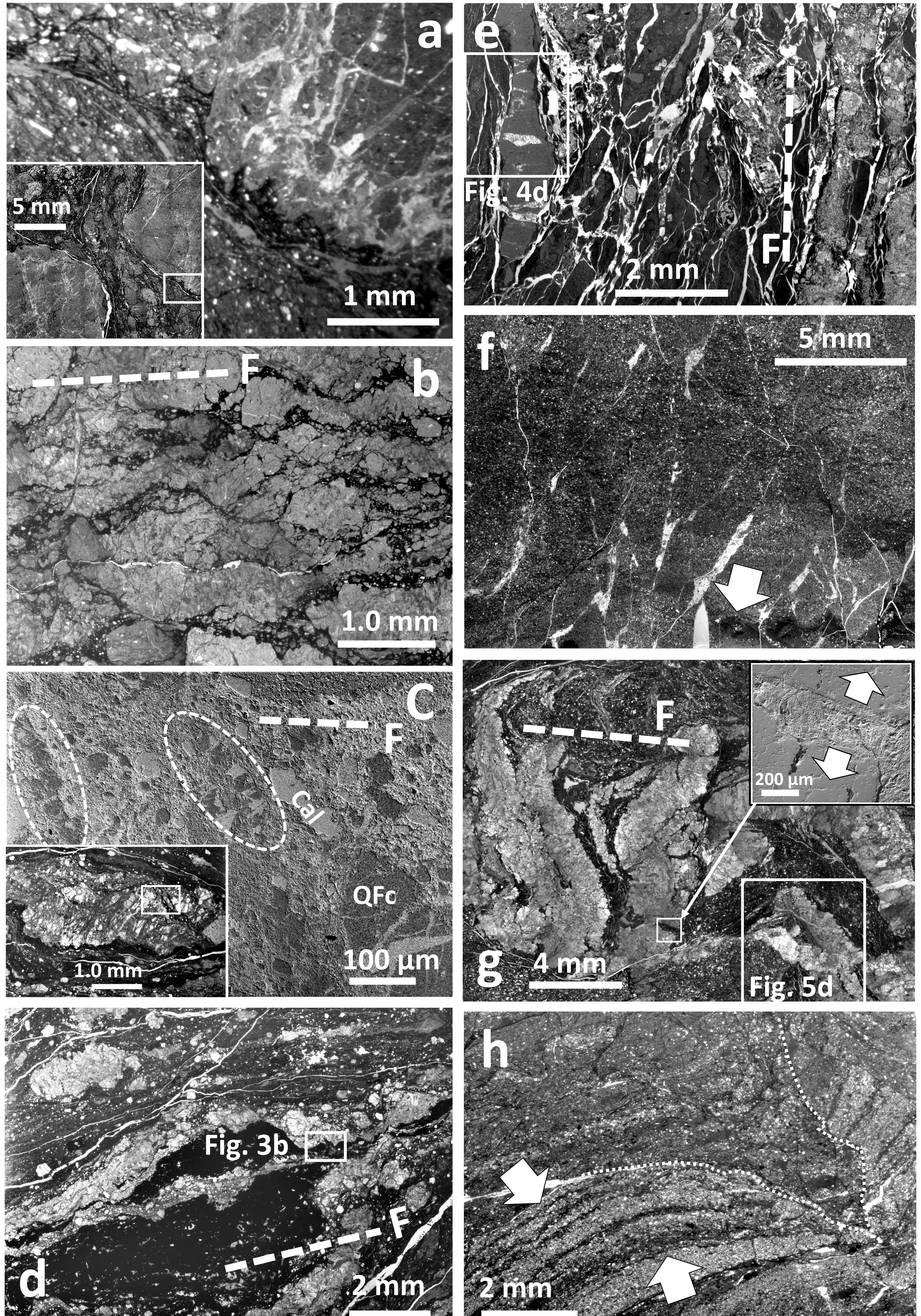

Fig. 2. Typical deformation microstructures in siltstone-shale units of the SAF damage zone. Images are optical PPL unless otherwise stated. Trace of foliation identifiable at section-scale is indicated by dashed line labeled F.

a. Close-up view showing impingement dissolution of a reworked quartzo-feldspathic block in block-in-matrix gouge. Inset box relates the magnified area to a general view of the gouge microstructure. Sample G11, 3187.3m MD.

b. Typical foliation mainly defined by a pressure solution cleavage. An antitaxial calcite vein fabric at high angles to foliation is present in quartzofeldspathic clasts. Note that calcite veins are confined to within clast boundaries. Sample G23, 3193.3m MD.

c. BS-SEM image showing close-up view of ultracataclasite located within dark-colored streaks in the smaller inset box. Dashed line areas encircle fragments of calcite vein fabric relicts from earlier deformation by pressure solution. Cal is calcite, QFc is reworked quartzofeldspathic clast. Sample G24, 3193.7m MD (black gouge ~2.8m SW of SDZ).

d. Sheared mass of secondary pyrite stretched sub-parallel to trace of foliation. Note absence of deformation by pressure solution at contacts between pyrite mass and quartzofeldspathic gouge. Inset box is location of chemical map in Fig. 3b. Sample same as in c.

e. Pressure solution cleavage foliation NE of SDZ. Anastomosing relaxation cracks have opened along foliation. Note calcite fabric in siltstone clast on far-left side. Inset box is location of Fig. 4d. Sample G32, 3198.6m MD.

f. Calcite-sealed blocks of fractured banded siltstone ~1.6m SW of CDZ. White arrow points to impingement dissolution. Sample G41, 3295m MD .

g. Intensely deformed foliated block-in-matrix gouge including multiple generations of blocky calcite veins. Convoluted calcite veins reflect flowage of shale-rich ultracataclasite matrix between quartzofeldspathic cataclasite blocks. Inset SEM-SE image shows typical injection of matrix ultracataclasites into tensile microfractures in calcite veins in this sample. Sample G52, 3301.34m MD.

h. Shallow injection of coarse-grained cataclasites into a reworked block-in-matrix gouge (dotted trace). Arrows show pressure solution seams along bands of siltstone cataclasite. White streaks are thin blocky calcite veins. Sample G65, 3311.1m MD.

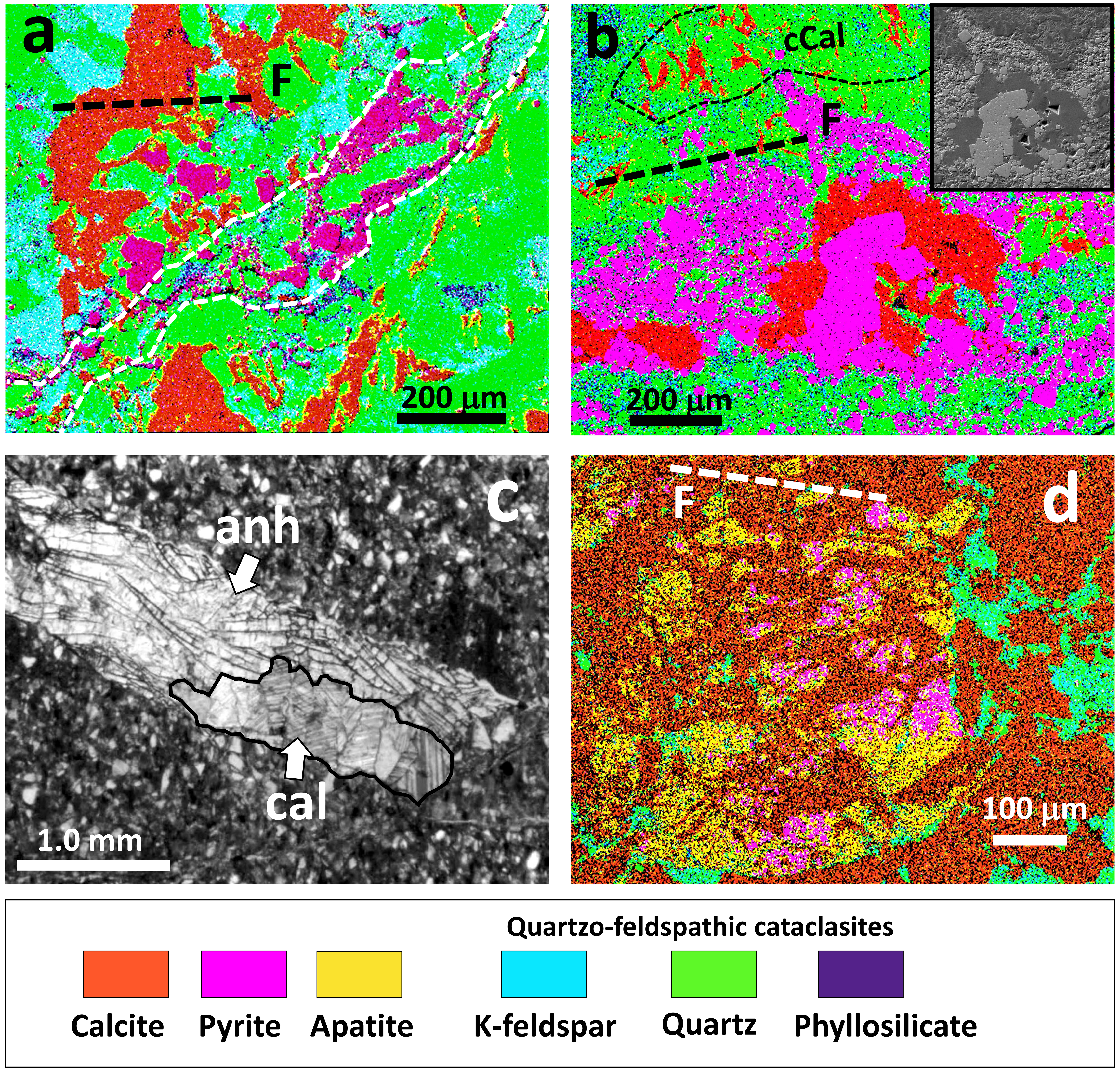

Fig. 3. Elemental maps interpreted as mineral composition showing typical microstructural association of blocky calcite veins with hydrothermal mineralization in damage zone samples. Dashed line labeled F is trace of foliation recognizable at section-scale.

a. Secondary pyrite and blocky vein-calcite sheared along a thin cataclasite band. The band is traced with white dashed line based on SEM image of mapped area. Sample G13, 3188.6m MD.

b. Secondary pyrite overprinting blocky calcite sheared along foliation (see inset box in Fig. 2d). Note euhedral forms in pyrite (inset SEM-SE image). The area within dashed line (cCal) is a clast with calcite vein fabric related to pressure solution cleavage. Sample G24, 3193.7m MD (~3m SW of SDZ).

c. A vein fragment comprised of prismatic anhydrite crystals (anh) and strongly twinned blocky calcite (cal). Sample G41, 3295m MD (~1.5m SW of CDZ).

d. Growth of pyrite and apatite inclusions in strongly deformed blocky calcite vein. Sample G52, 3301.34m MD.

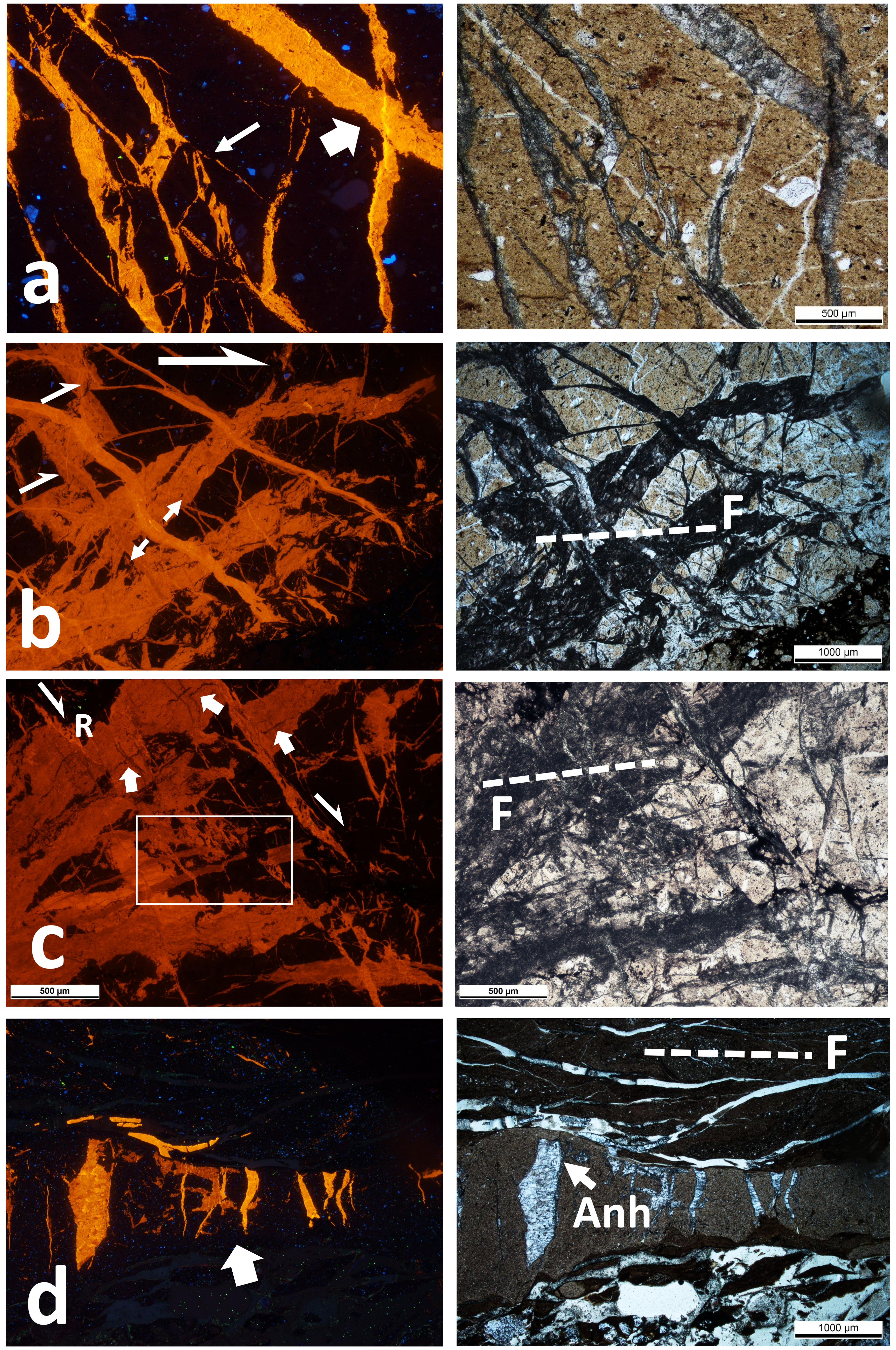

Fig. 4. Paired CL-PPL images showing microstructures of blocky and syntaxial calcite veins in SDZ-side damage zone of the SAF. Where present at section scale, trace of foliation (F) is shown with a dashed line.

a. Cross-cutting blocky and syntaxial elongate calcite vein generations (thick arrow) in highly fractured, non-foliated siltstone. A thin arrow shows blocky veins sealing a micro-jog. Sample G13**,** 3188.60m MD.

b. Blocky calcite vein generations deformed by local dextral shear and overprinted by syntaxial crack-seal veins along extension cracks (brighter CL). Block-in-matrix foliated siltstone-shale cataclasite. Sample G22, 3192.51m MD.

C. Blocky calcite veins offset along a set of R-shear microfractures and overprinted by syntaxial crack-seal veins of variable CL. Area within rectangular box shows dark and light CL veins mutually overprint. Thick arrows point to possible pressure solution seams in calcite veins. Intensely foliated siltstone-shale cataclasite (black gouge). Sample G24**,** 3193.70m MD.

d. Calcite-vein fabric with anhydrite inclusion (Anh) at high angles to foliation in a large siltstone clast (see inset box in Fig. 2e for microstructural context). Thick, bent e-twins are present in the large blocky vein. Arrow points to an example of mutual crosscutting of calcite veins with dark and light luminescence. Sample G32, 3198.6m MD.

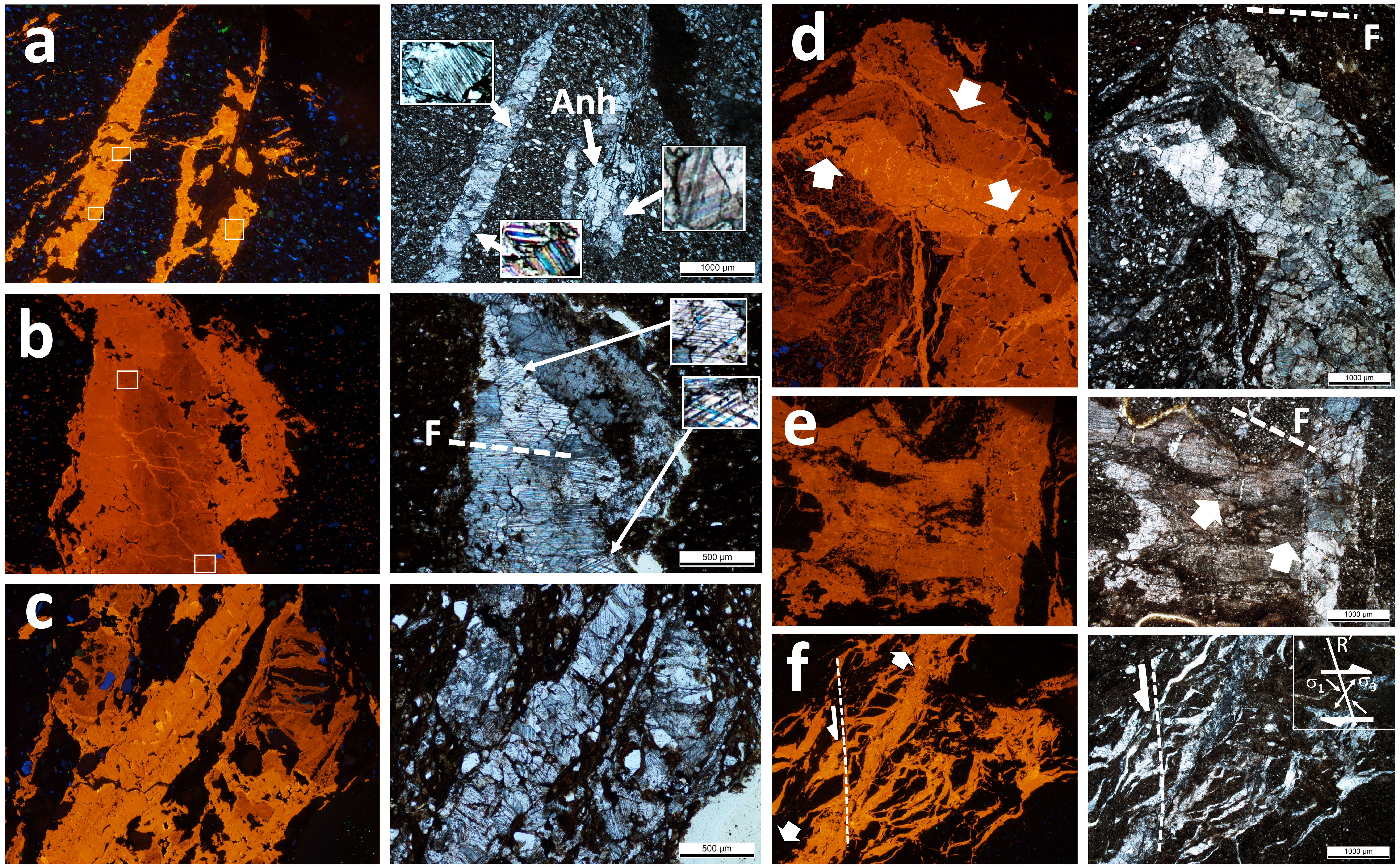

Fig. 5. Paired CL-PPL images showing microstructures of blocky and syntaxial calcite veins in CDZ-side damage zone of the SAF. Where present at section scale, trace of foliation (F) is shown with a dashed line.

a. Sample G41 ~1.5m SW of CDZ showing blocky veins with anhydrite inclusions (Anh). Mechanical twins with different lamellae thickness and spacing are present (inset boxes marked on CL and PPL images). The image is typical of 5 sections from two G41 core billets at 3295m and 3295.13m MD in banded siltstone.

b. An open-cavity blocky growth with distinct areas of light and dark luminescence zoning. Note network of thin crack-seal veins with brighter luminescence extending from margins into interior of the vein. Clear examples of crosshatched, tapering, and gently bent e-twin types are shown in inset boxes marked on PPL and CL images. Note tight lamellar spacing of the twins throughout. Foliated siltstone-shale. Sample G45, 3299.3m MD.

c. Showing blocky elongate type veins with mostly thin, tabular e-twins. Note patchy luminescence zoning. Foliated siltstone-shale. Sample G47, 3300.0m MD.

d. Strongly deformed blocky veins (see inset box in Fig. 2g) with a variety of e-twin lamellae structures. On CL image, cross-cutting relationship indicates at least 3 vein generations with latest generation having brighter luminescence. Note open cavities (arrows) in bright-color veins. Foliated siltstone-shale. Sample G52, 3301.34m MD.

e. Blocky veins (mainly on the right side) cut across antitaxial fibrous veins with pressure solution seams (arrows). Tabular and thick twin lamellae types are present in blocky calcite. Foliated siltstone-shale. Sample G56, 3305.4m MD.

f. Showing blocky veins seal a sheared jigsaw texture. Shear along an R' plane (dashed line) and implosion-driven extension (arrows) are consistent with stress field depicted on PPL image. Foliated siltstone-shale. Sample 65, 3311.1m MD.

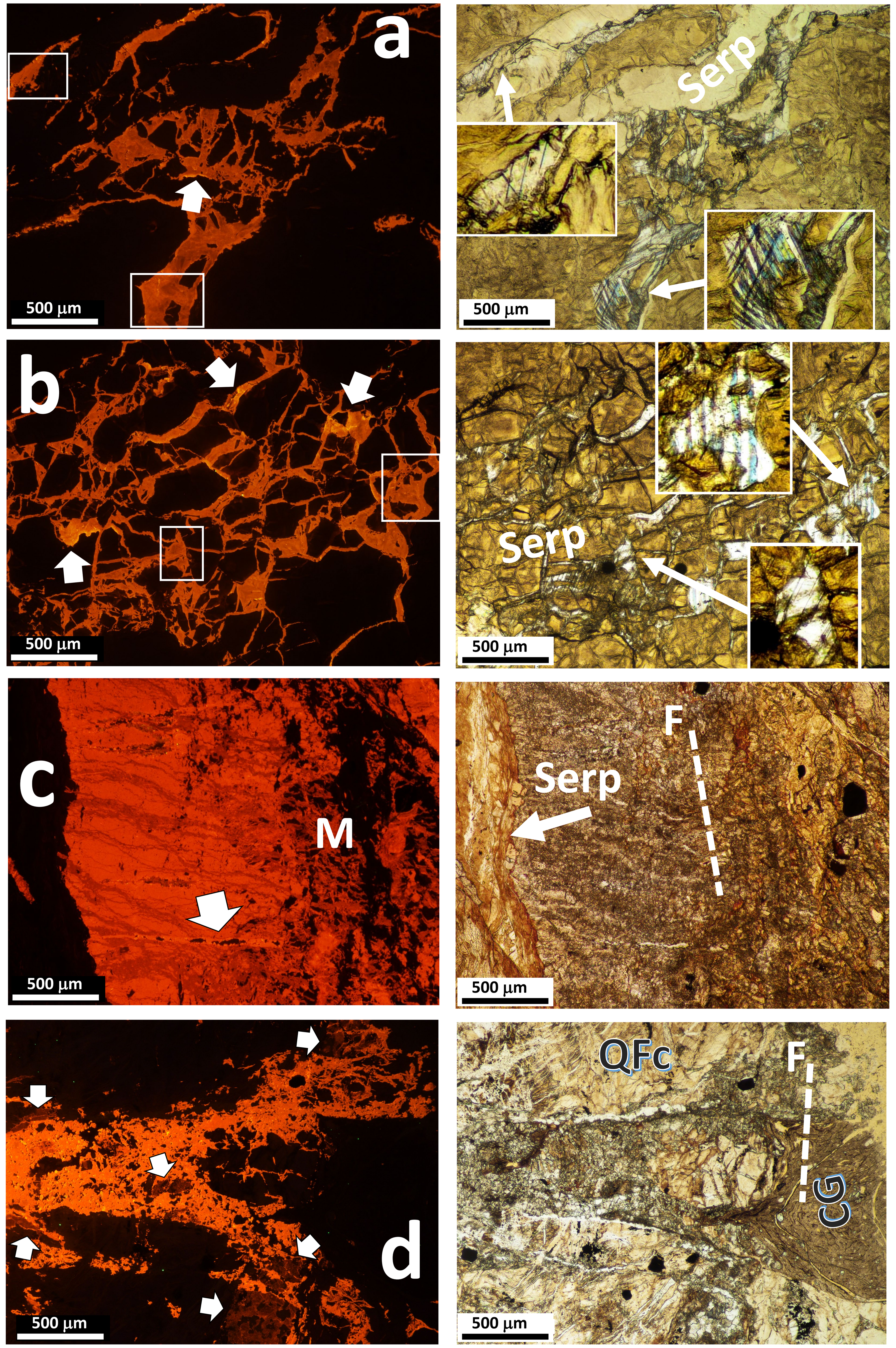

Fig. 6. Paired CL-PPL images showing microstructures of blocky and syntaxial calcite veins in active creep zones CDZ and SDZ. Trace of foliation recognizable at section scale is shown with a dashed line labeled F.
a and b. CL images of blocky calcite veins seal implosion jigsaw textures in two different areas on the same thin section in SDZ sample. Inset close-up views on PPL images show presence of a variety of e-twin lamellae in blocky calcites including thin, tabulated thick, and thick with tapered bent and lensoid types. Note patchy calcite luminescence (white arrows). The gouge is mostly composed of altered and deformed serpentinite phases. Sample G27, 3196.70m MD.
c. A segment along length of a thick blocky vein in CDZ crosscut by a set of calcite-sealed extension veins with dull luminescence. The latter veins do not extend into surrounding serpentine-rich gouge matrix (Serp) but merge with mesh-like veins (M) on the right. Note string of open cavities along a bright-colored vein that seals a late extension crack (arrow on CL image). Sample G44, 3298.3m MD collected from within serpentinite block.
d. Showing one of several fluidized gouge injections across quartzo-feldspathic bands (QFc) that run parallel to foliation in CDZ sample. Injection conduit is mostly sealed by blocky calcite growths, ~50µm in average grain size, with gouge fragment inclusions. Note calcite generation with dull luminescence (arrows on CL image). Injection flow lines in clay-rich gouge (CG) could be seen at opening end and along injection walls. Sample G44, 3298.3m MD.

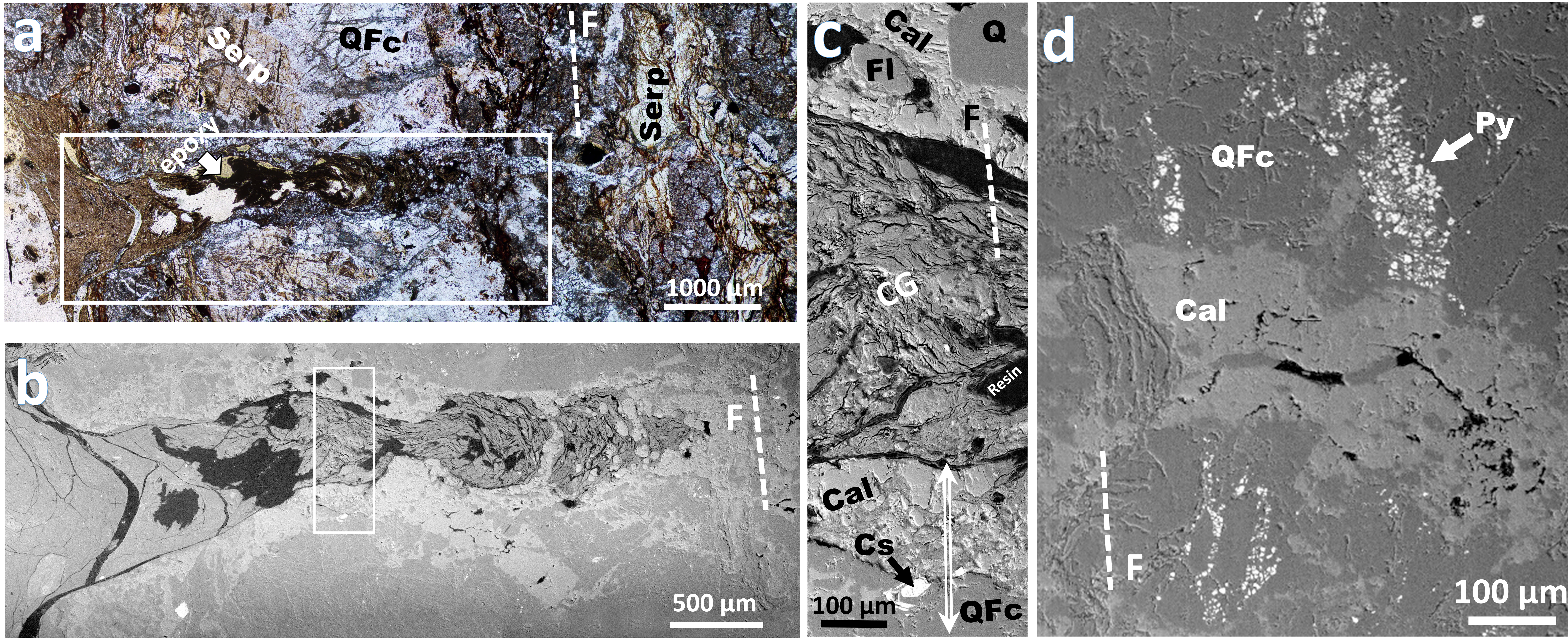

Fig. 7. Fluidized gouge injection microstructures in CDZ sample (G44, 3298.3m MD). Trace of foliation is shown with dashed line F.

a. Gouge injection microstructure with aspect ratio of 0.25 (INJ G44A in Table 1) shows an injection from left to right at high-angles to foliation shown. Image is an optical XPL mosaic. Plain white and yellowish areas of the image are respectively voids and voids filled with resin (labeled arrow). Brown and black areas within the injection conduit are extremely fine-grained Mg-rich clay gouge. QFc is foliation-parallel quartzofeldspathic bands of cataclasites. Serp is serpentinite-derived phyllosilicate phases.

b. BS-SEM mosaic image partially covering the injection area (inset box in a). Clay-rich gouge fills injection conduit lined with blocky calcite growth. Intruding gouge grades from coarse at the opening to extremely fine-grained at the tip of injection microstructure. Note chambered structure of the injection conduit involving cross-conduit calcite growth.

c. BS-SEM image (inset box in b) showing close-up view of extremely fine-grained conglobate clay gouge (CG) in mid section of the injection. Injection-wall sequence along double-headed arrow consists of calcite-sealed quartzo-feldspathic microbreccia, and old foliation-parallel quartzo-feldspathic cataclasite band (QFC) at the bottom. A chrome-spinel porphyroblast (Cs), deformed by brittle fracture, is shown by black arrow. At the top side, calcite-sealed microbreccia includes large feldspar (Fl), and quartz (Q) clasts.

d. A small reworked injection microstructure across quartzofeldspathic cataclasite band. Areas in black are void spaces. Note foliation-parallel cluster of pyrite framboids (Py) crosscut by this injection microstructure.

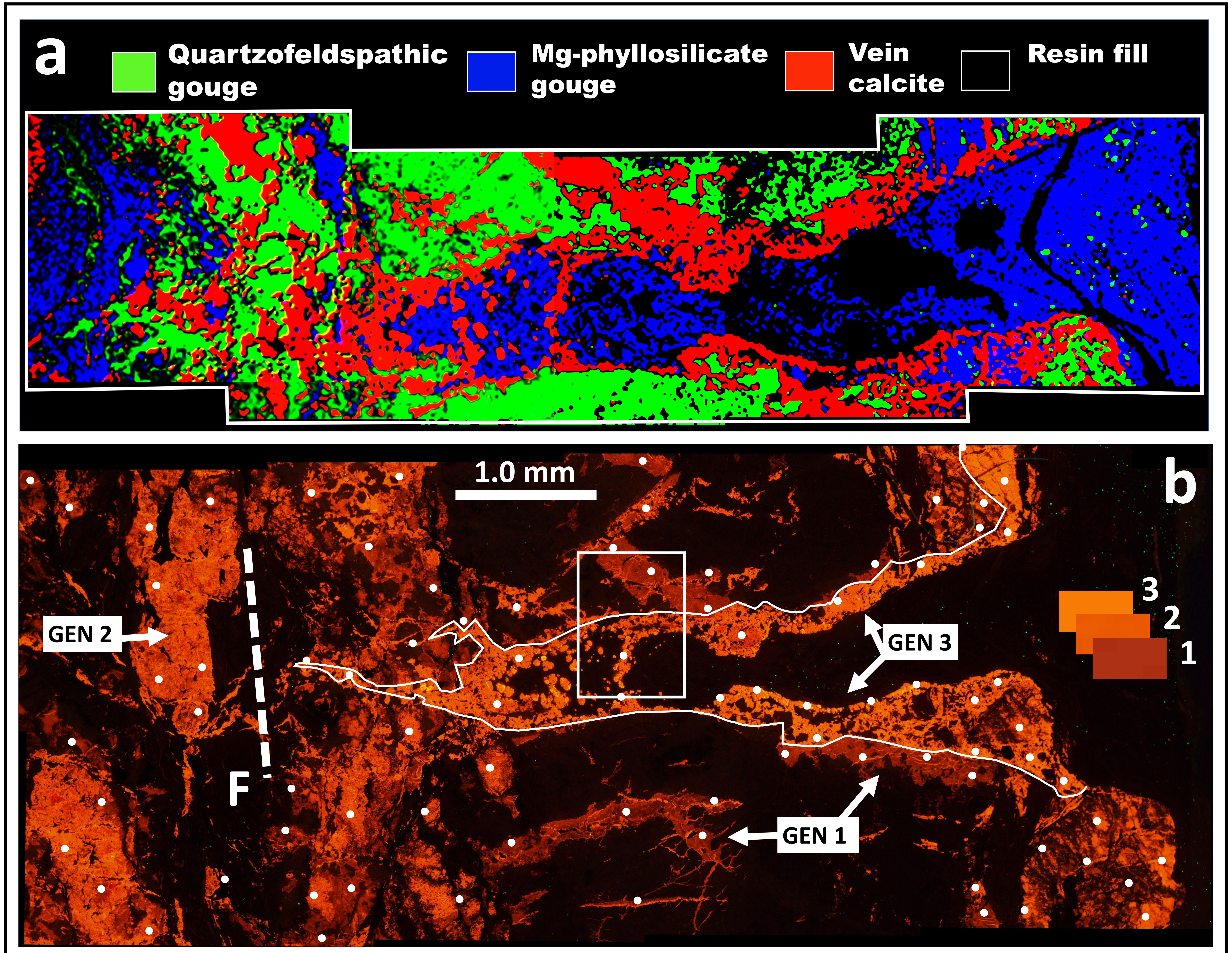

Fig. 8. Composition map and CL image of fluidized gouge injection microstructure (G44A, INJ. A, in Table 1) in CDZ sample.
a. Interpreted elemental map showing microstructural relationship between blocky calcite growth and injected serpentinite-rich gouge.
b. CL image revealing spatial interaction of calcite from different generations involved in fluidized gouge injection. Three generations of calcite growth, labeled GEN 1-3, could be identified via a combination of luminescence contrast and crosscutting relationship. Injection wall (white border line) is lined with latest calcite generation, GEN 3, that crosscuts earliest generation, GEN 1, calcite. Isolated pixel color tiles of the 3 calcite generations are shown on the right. White dots on the image are 83 EDS data collection spots. Inset box is location of EBSD images shown in Figs. 9b-c.

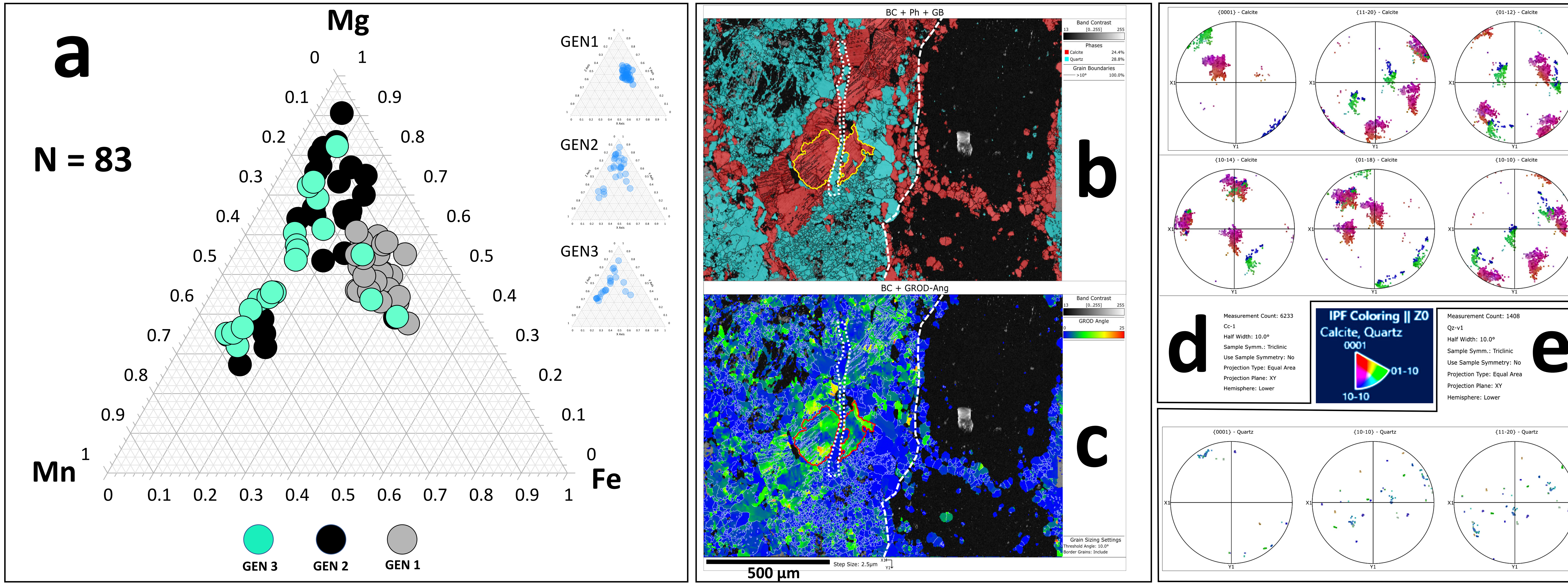

Fig. 9. The trace-element concentration and EBSD analysis of blocky calcites involved in fluidized gouge injection microstructure shown in Fig. 8.
a. Ternary plot of Mean trace-element concentrations; individual plots on the right with GEN 3 being the latest calcite vein generation.
b. EBSD-derived phase map (red = calcite, cyan = quartz) of area within Fig. 8b inset box. Two apparently separate GEN 1 twinned calcite grains are highlighted in yellow. White dashed line in b and c separates GEN1 calcite veins from GEN3 calcite that lines injection structure. Dotted white line in b and c is a GEN3-parallel quartz vein that separates the two parts of GEN 1 calcite grain highlighted in yellow. Note the well-developed e-twins in GEN1 calcite grains (parallel black lines) and their absence from GEN3 calcite grains.
c. EBSD-derived grain reference orientation deviation (GROD) map of area in b (blue = 0°, red = 25°). Note that GEN1 calcite domains have high GROD values (up to 25° in the highlighted grain) indicating a high level of lattice distortion within the grains, whereas GEN3 calcite grains, across the dashed line, have low GROD values indicating little or no lattice distortion within the grains. Quartz grains in the quartz vein (dotted line) have low GROD values indicating little or no lattice distortion. Also note the well-developed e-twins in GEN1 calcite grains (parallel white lines) and their absence from GEN3 calcite grains.
d. Lower-hemisphere pole figures for the two highlighted GEN 1 calcite "grains" in image b. Note that the two grains have the same lattice orientations, consistent with being originally part of the same calcite grain.
e. Lower-hemisphere pole figures for grains in quartz vein that separates GEN1 calcite grain in b and c. Note that the twelve quartz grains identified as part of the vein in c have a restricted range of c-axis directions oblique to the vein trace, while m <10-10> and a <11-20> axes define a broad girdle. Colors are in the IPF space.

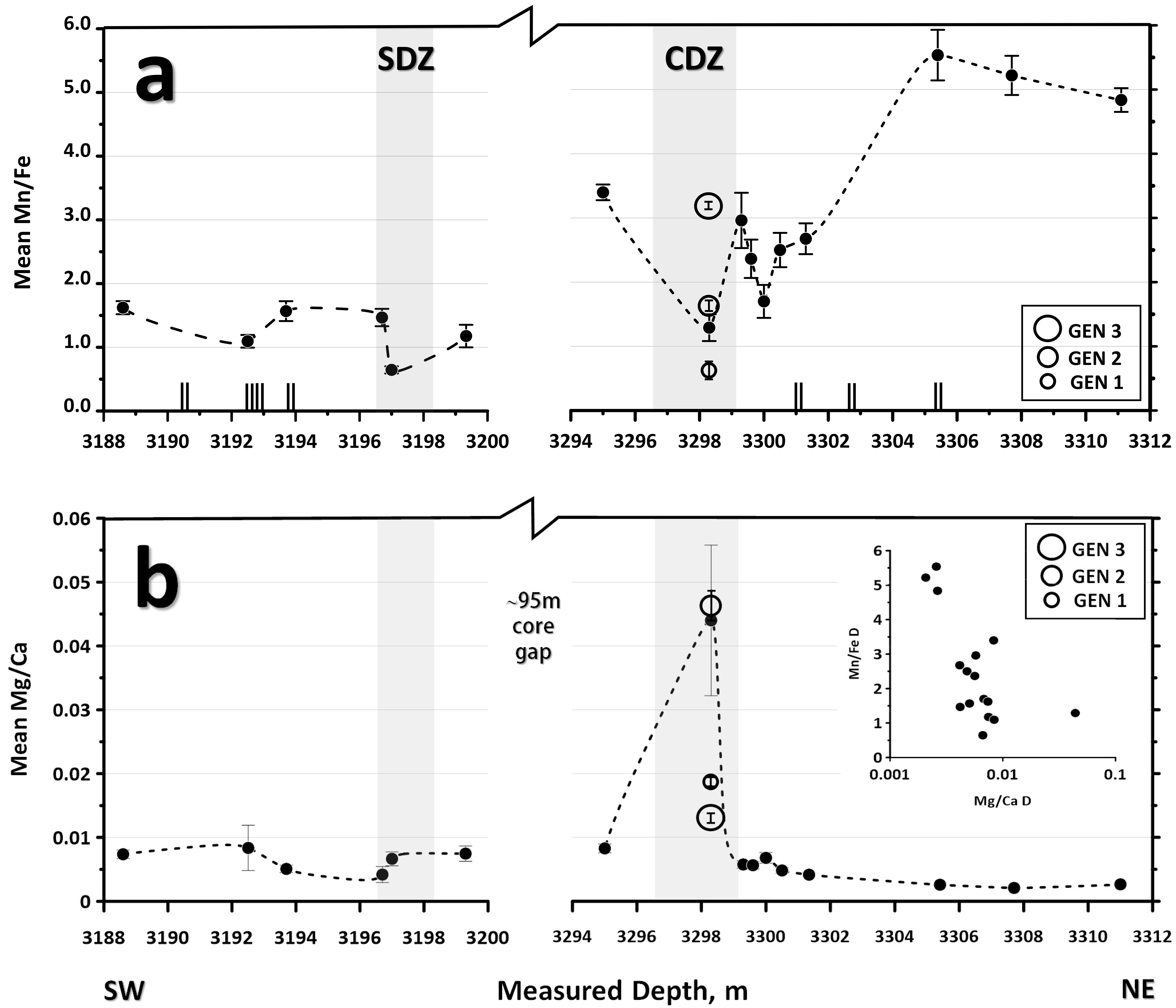

Fig. 10. Across-the-fault variations in composition of blocky, elongate blocky, and syntaxial calcite veins. Mean sampling frequency ~1.6 m, excluding the coring gap. Active creep intervals SDZ and CDZ are indicated by shaded vertical bars. Error bars are Standard Error of sample population. Short double lines on x-axis are location of minor faults transferred from Fig. 1.

a. Changes in mean value of Mn/Fe ratio (data from Table 2a). Open-circle symbols with different sizes represent mean Mn/Fe ratio for gouge-injection calcite vein generations in CDZ interval (data from Table 2b). GEN 3 is the latest generation.

b. Changes in mean value of Mg/Ca ratio (data from Table 2a). The open circle symbols in CDZ interval represent mean Mg/Ca ratio for gouge-injection calcite vein generations (data from Table 2b). Inset scattergram showing a generally negative correlation between Mn/Fe and Mg/Ca ratio (Table 2 ratio columns, excluding G44inj. data).

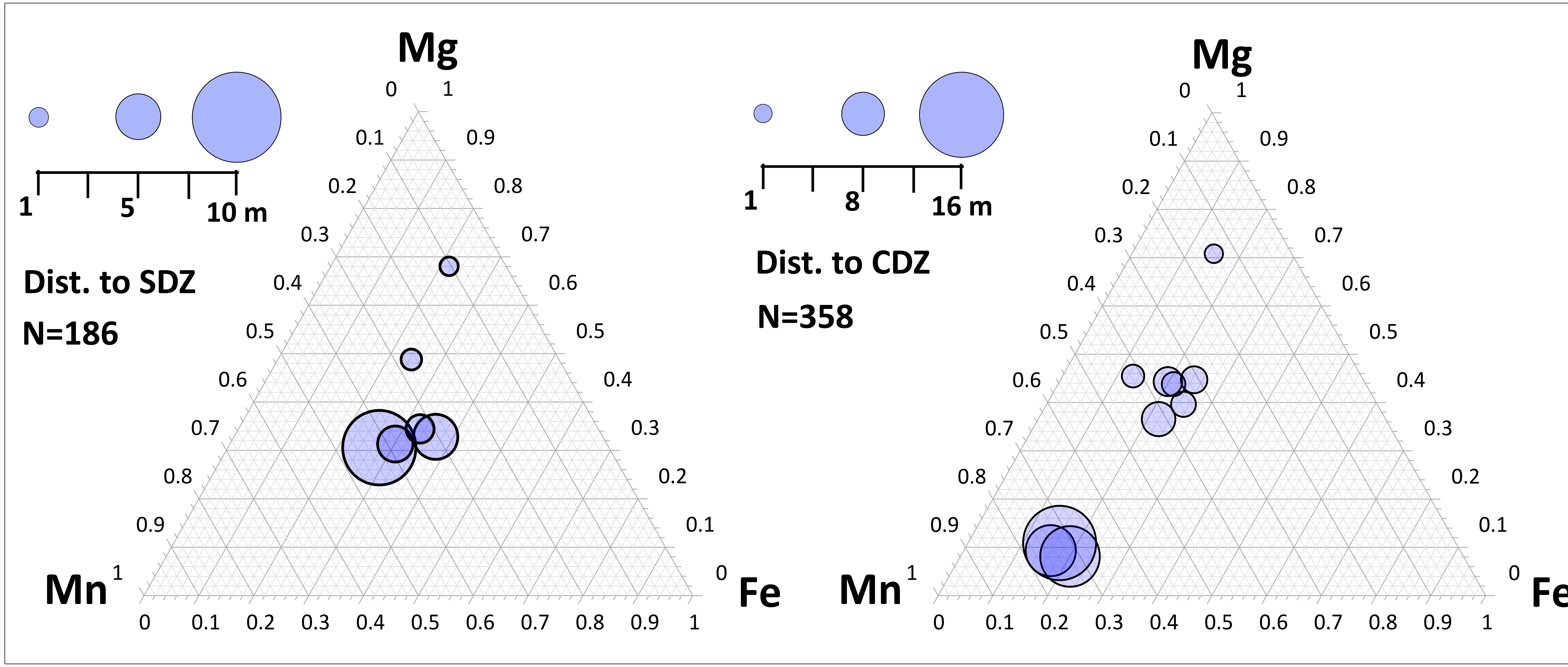

Fig. 11
Ternary plots showing changes in trace element composition of blocky calcite veins with distance from the active-creep intervals SDZ and CDZ (excluding data from injection-related calcite veins).

Table 1.
Aspect ratio data for gouge injection microstructures a, b, and c as they appeared on parallel thin sections A, B, and C through the CDZ core sample billet, cut parallel to each other, perpendicular to foliation.

Sample	INJ.	L, mm	W, mm	W/L
G44 A	a	5.651	1.352	0.25
G44 A	b	3.616	1.446	0.40
G44 A	C	2.486	1.243	0.50
G44 B	a	3.653	0.913	0.25
G44 B	b	4.762	3.524	0.74
G44 C	a	4.491	1.078	0.24
G44 C	b	3.685	1.179	0.32

Table 2.
Mean atomic wt.% Mg, Fe, Mn, and Mg/Ca and Mn/Fe values (mean of the ratios) from spots on CL images of calcite veins in all samples. Values in second row for each sample is Standard Error.

a. Mean values for N spots in typical calcite veins in each sample.

b. Individual and combined mean values for N spots in calcite generations (GEN 1-3) related to sample G44 gouge injection microstructures (see INJ. a, sample G44A, Table 1). GEN 3 is the latest generation.

2b

Vein	Mg	Fe	Mn	Mg/Ca	Mn/Fe	N
GEN 1	**0.331**	**0.185**	**0.097**	**0.018**	**0.578**	**32**
	0.048	0.009	0.007	0.003	0.081	
GEN 2	**0.827**	**0.154**	**0.161**	**0.047**	**1.631**	**28**
	0.151	0.022	0.010	0.010	0.227	
GEN 3	**0.245**	**0.060**	**0.120**	**0.013**	**3.196**	**23**
	0.052	0.011	0.007	0.003	0.407	
combined	**0.475**	**0.140**	**0.125**	**0.026**	**1.659**	**83**
	0.062	0.010	0.006	0.004	0.180	

2a

Sample	Mg	Fe	Mn	Mg/Ca	Mn/Fe	N
G65	**0.053**	**0.081**	**0.352**	**0.003**	**4.837**	**53**
	0.005	0.005	0.011	0.000	0.185	
G61	**0.039**	**0.096**	**0.344**	**0.002**	**5.220**	**27**
	0.003	0.027	0.014	0.000	0.305	
G56	**0.051**	**0.087**	**0.410**	**0.003**	**5.536**	**34**
	0.003	0.010	0.022	0.000	0.394	
G52	**0.082**	**0.049**	**0.093**	**0.004**	**2.676**	**66**
	0.006	0.003	0.003	0.000	0.240	
G51B	**0.067**	**0.030**	**0.055**	**0.005**	**2.500**	**36**
	0.006	0.003	0.002	0.000	0.267	
G47	**0.127**	**0.070**	**0.088**	**0.007**	**1.700**	**19**
	0.016	0.008	0.005	0.001	0.257	
G46	**0.118**	**0.074**	**0.105**	**0.006**	**2.364**	**27**
	0.013	0.011	0.005	0.001	0.299	
G45	**0.098**	**0.047**	**0.079**	**0.006**	**2.961**	**37**
	0.009	0.005	0.003	0.001	0.431	
G44	**0.718**	**0.152**	**0.144**	**0.044**	**1.290**	**30**
	0.168	0.013	0.010	0.012	0.208	
G41	**0.164**	**0.046**	**0.150**	**0.008**	**3.398**	**29**
	0.014	0.003	0.006	0.001	0.122	
G32	**0.138**	**0.133**	**0.130**	**0.007**	**1.176**	**20**
	0.022	0.013	0.019	0.001	0.177	
G28	**0.138**	**0.044**	**0.021**	**0.007**	**0.646**	**44**
	0.022	0.005	0.001	0.001	0.056	
G27	**0.078**	**0.039**	**0.043**	**0.004**	**1.467**	**41**
	0.022	0.006	0.004	0.001	0.136	
G24	**0.064**	**0.062**	**0.079**	**0.005**	**1.568**	**35**
	0.008	0.006	0.005	0.001	0.156	
G22	**0.152**	**0.170**	**0.141**	**0.008**	**1.095**	**22**
	0.060	0.035	0.006	0.004	0.099	
G13	**0.134**	**0.121**	**0.184**	**0.007**	**1.622**	**24**
	0.012	0.008	0.010	0.001	0.103	

TABLE 1

Sample	INJ	L, mm	W, mm	W/L
G44 A	a	5.651	1.352	0.25
G44 A	b	3.616	1.446	0.40
G44 A	c	2.486	1.243	0.50
G44 B	a	3.653	0.913	0.25
G44 B	b	4.762	3.524	0.74
G44 C	a	4.491	1.078	0.24
G44 C	b	3.685	1.179	0.32

Editable Tables

TABLE 2

2a

Sample	Mg	Fe	Mn	Mg/Ca	Mn/Fe	N
G65	0.053	0.081	0.352	0.003	4.837	53
	0.005	0.005	0.011	0.000	0.185	
G61	0.039	0.096	0.344	0.002	5.220	27
	0.003	0.027	0.014	0.000	0.305	
G56	0.051	0.087	0.410	0.003	5.536	34
	0.003	0.010	0.022	0.000	0.394	
G52	0.082	0.049	0.093	0.004	2.676	66
	0.006	0.003	0.003	0.000	0.240	
G51B	0.067	0.030	0.055	0.005	2.500	36
	0.006	0.003	0.002	0.000	0.267	
G47	0.127	0.070	0.088	0.007	1.700	19
	0.016	0.008	0.005	0.001	0.257	
G46	0.118	0.074	0.105	0.006	2.364	27
	0.013	0.011	0.005	0.001	0.299	
G45	0.098	0.047	0.079	0.006	2.961	37
	0.009	0.005	0.003	0.001	0.431	
G44	0.718	0.152	0.144	0.044	1.290	30
	0.168	0.013	0.010	0.012	0.208	
G41	0.164	0.046	0.150	0.008	3.398	29
	0.014	0.003	0.006	0.001	0.122	
G32	0.138	0.133	0.130	0.007	1.176	20
	0.022	0.013	0.019	0.001	0.177	
G28	0.138	0.044	0.021	0.007	0.646	44
	0.022	0.005	0.001	0.001	0.056	
G27	0.078	0.039	0.043	0.004	1.467	41
	0.022	0.006	0.004	0.001	0.136	
G24	0.064	0.062	0.079	0.005	1.568	35
	0.008	0.006	0.005	0.001	0.156	
G22	0.152	0.170	0.141	0.008	1.095	22
	0.060	0.035	0.006	0.004	0.099	
G13	0.134	0.121	0.184	0.007	1.622	24
	0.012	0.008	0.010	0.001	0.103	

2b

Vein	Mg	Fe	Mn	Mg/Ca	Mn/Fe	N
GEN 1	0.185	0.331	0.097	0.018	0.578	32
	0.009	0.048	0.007	0.003	0.081	
GEN 2	0.154	0.827	0.161	0.047	1.631	28
	0.022	0.151	0.010	0.010	0.227	
GEN3	0.060	0.245	0.120	0.013	3.196	23
	0.011	0.052	0.007	0.003	0.407	
Combined	0.475	0.140	0.125	0.026	1.659	83
	0.062	0.010	0.006	0.004	0.180	